UNIVERSITY of CALIFORNIA
Santa Barbara

Detection and Characterization of Exoplanet and Binary Star Systems Through Direct Imaging and Spectroscopy

A dissertation submitted in partial satisfaction of the
requirements for the degree of

Doctor of Philosophy

in

Physics

by

Isabel Alexandra Lipartito

Committee in charge:

Professor Benjamin Mazin, Chair

Professor Timothy D. Brandt

Professor Omer Blaes

March 2021

The dissertation of Isabel Alexandra Lipartito is approved:

Professor Timothy D. Brandt

Professor Omer Blaes

Professor Benjamin Mazin, Chair

March 2021

Detection and Characterization of Exoplanet and Binary Star Systems Through Direct Imaging and Spectroscopy

by

Isabel Alexandra Lipartito

To all the women before me who made this possible.

Acknowledgements

Technical Acknowledgements and Attributions:

The development of the MKID Exoplanet Camera was a massive project on behalf of all members of the Mazin Lab and many researchers at other institutions.

The readout hardware was designed by Ben Mazin and Paschal Strader with our collaborators at Fermilab. The readout firmware was developed by Sean McHugh, Paschal Strader, and Neelay Fruitwala. The FPGA chips and ADCs were generously donated by Xilinx and Analog Devices, respectively. The MKID arrays were fabricated by Bruce Bumble at JPL, and Paul Szypryt and Gregoire Coiffard at UCSB. MEC arrays and their precursors were tested by Seth Meeker, Clinton Bockstiegel, Nicholas Zobrist, Noah Swimmer, and Sarah Steiger.

MEC's integration at the Subaru Telescope was made possible with support from Subaru staff including Oliver Guyon, Julien Lozi, Nemanja Jovanovic (now at Caltech), and others. Night on-sky observations were only possible with support from the SCExAO team: Olivier Guyon, Julien Lozi, Sebastien Vievard, and Ananya Sahoo. Remote observations from UCSB were made in part with Ben Mazin, Neelay Fruitwala, Nicholas Zobrist, Sarah Steiger, Noah Swimmer, Jeb Bailey, Kristina Davis, Rupert Dodkins, and Jenny Smith. The aforementioned members of the Mazin Lab, along with student researcher Clarissa Rizzo, were instrumental in the development and testing of the MKID Pipeline.

The work in Chapter 2 was originally presented in Fruitwala et al. (2020). My contribution was the assembly and testing of the MEC Readout System. This work was funded in part by an NSF ATI grant, and by a US Department of Energy grant.

The work in Chapter 3 was originally presented in Walter et al. (2020). My contribution was the development and testing of several key components of the MKID Pipeline, along with reduction and post-processing of MEC on-sky data. I also characterized the contrast limits of the instrument.

The work in Chapter 4 will be presented in "Orbital Parameters and Binary Properties of 37 FGK stars in the Cores of Open Clusters NGC 2516 and NGC 2422", Lipartito et al (to be submitted to The Astronomical Journal). This is a continuation of the spectroscopic observations of two open clusters made using the Michigan/Magellan Fiber System originally presented in Bailey et al. (2016) and Bailey et al. (2018). Chapter 4 describes my continuation of this work, fitting orbits to the RV binaries identified in the two previous papers.

The work in Chapter 4 made use of data from the European Space Agency (ESA) mission *Gaia* (https://www.cosmos.esa.int/gaia), processed by the *Gaia* Data Process-

ing and Analysis Consortium (DPAC, https://www.cosmos.esa.int/web/gaia/dpac/consortium). Funding for the DPAC has been provided by national institutions, in particular the institutions participating in the *Gaia* Multilateral Agreement. The work in this chapter also used `eleanor`, a light curve extraction tool for TESS Full-Frame Images, as presented in Feinstein et al. (2019).

The work throughout this thesis used Astropy,[1] a community-developed core Python package for Astronomy (Astropy Collaboration et al., 2013, 2018).

Finally, I acknowledge support by the National Science Foundation Graduate Research Fellowship under grant number 1650114.

Personal Acknowledgements:

I foremost want to thank my advisor, Dr. Ben Mazin, for the past six years of guidance and support. Thank you for your leadership and vision during these innovative and challenging projects. I am thankful to have been a part of this endeavor, and to have worked with you in the process. I am also extremely grateful to Dr. Timothy Brandt and Dr. Jeb Bailey, who mentored me throughout the RV Binaries in Open Clusters project and taught me so much about data analysis and scientific communication. I thank the entirety of the Mazin Lab for working with me all these years and fostering a friendly climate that made me excited to come to lab every single morning.

I want to thank my family for supporting me throughout my education and for believing in me at times when I had trouble believing in myself. You have made me the person I am today, and I am forever grateful for that.

Sincere thanks is owed to my close graduate student friends, Sarah Lerner and Dr. Max Lee. Thank you both for listening to me ramble on for years about persistent speckles and misplaced torque wrenches. I could not have gotten through the PhD process without your friendship and support.

Finally, I want to thank my 'coven' of physicists (also known as housemates): Amalu Shimamura, Sabrina Wagner, and Valentina Hallefors. Thank you for cheering me on every step of the way these past few years and for providing a safe, loving home environment.

[1] http://www.astropy.org

Curriculum Vitæ

Isabel Alexandra Lipartito

Education

2021	(Expected) Ph.D., Physics with an Astrophysics Emphasis, University of California, Santa Barbara
2018	M.A., Physics, University of California, Santa Barbara
2015	B.A., Physics and Astronomy, Smith College, Northampton

Honors and Awards

2019	Mananya Tantiwiwat Award for Outstanding Research, UCSB Physics Department
2017-2020	National Science Foundation Graduate Research Fellowship
2015	University of California, Santa Barbara Regents Fellowship

Select Publications

"Orbital Parameters and Binary Properties of 37 FGK stars in the Cores of Open Clusters NGC 2516 and NGC 2422", **I. Lipartito**, J. I. Bailey, T. Brandt, and B.A. Mazin *To be submitted to The Astronomical Journal (AJ) 2021.*

"Optical and Near-IR Microwave Kinetic Inductance Detectors (MKIDs) in the 2020s", B. A. Mazin, J. I. Bailey, J. Bartlett, C. Bockstiegel... **I. Lipartito** et al. *Astro2020 APC Whitepaper* (2019)

"DARKNESS: A Microwave Kinetic Inductance Detector Integral Field Spectrograph for High-Contrast Astronomy", S. R. Meeker, B. A. Mazin, A. B. Walter, P. Strader... **I. Lipartito** et al. *PASP* Vol. 130, No. 988 (2018)

"The Solar Chromosphere Observed at 1 Hz and 0."2 Resolution", **I. Lipartito**, P. G. Judge, K. Reardon, and G. Cauzzi. *ApJ* 785, 109 (2014)

Abstract

Detection and Characterization of Exoplanet and Binary Star Systems Through Direct Imaging and Spectroscopy

by

Isabel Alexandra Lipartito

High contrast imaging and high-resolution spectroscopy are powerful techniques to characterize multi-component astronomical systems, examples of which range from stars with planetary companions to similar-mass stellar binaries. The first part of this thesis concerns the instrumentation and science behind detecting substellar companions. We present the development of single photon-counting detectors known as Microwave Kinetic Inductance Detectors (MKIDs) for exoplanet direct imaging. Optical/Near-IR MKIDs are low noise detectors which can resolve both the energy and arrival time of individual photons, returning microsecond-accurate time-tagged photon lists. These lists allow for image processing techniques that take advantage of photon spectral and arrival time information to model and subtract the stellar background, leaving behind signal from the faint planetary companion.

We discuss the commissioning and characterization of the MKID Exoplanet Camera (MEC), a 20,440 pixel MKID infrared camera that interfaces with the The Subaru Coronagraphic Extreme Adaptive Optics (SCExAO) planet finding instrument on the Subaru

Telescope at Mauna Kea. MEC is the first permanently deployed near-infrared MKID instrument and is designed to operate both as an IFU, and as a focal plane wavefront sensor in a multi-kHz feedback loop with SCExAO. We present the development and construction of a second generation digital readout system for MEC. Our readout system is capable of identifying, analyzing, and recording photon detection events in real time with a time resolution of order a few microseconds.

The second part of this thesis addresses the characterization of the orbital properties and stellar components of multiple star systems through high-resolution spectroscopy. We analyze stellar binaries observed with the Michigan/Magellan Fiber System (M2FS), a fiber-fed double spectrograph that was used to complete a several year-long survey of the core half-degree of open clusters NGC 2516 and NGC 2422. This survey targeted all stars identified as solar-analog photometric members. We present orbits for 24 binaries in the field of NGC 2516 (300 Myr) and 13 binaries in the field of NGC 2422 (130 Myr). Six of these systems are double-lined spectroscopic binaries (SB2s). We fit these RV variable systems with `orvara`, a MCMC-based fitting program that models Keplerian orbits. We use precise stellar parallaxes and proper motions from *Gaia* EDR3 to determine cluster membership. We impose a barycentric radial velocity prior on all cluster members; this significantly improves our orbital constraints.

Two of our systems have periods between 5 and 15 days, the critical window in which tides efficiently damp orbital eccentricity. These binaries should be included in future analyses of circularization across similarly-aged clusters. We also find a relatively flat

distribution of binary mass ratios, consistent with previous work. We identify a field star whose secondary has a mass in the brown dwarf range, as well as two cluster members whose RVs suggest the presence of an additional companion. Our orbital fits will help constrain the binary fraction and binary properties across stellar age and across stellar environment

This thesis explores the detection and characterization of stellar companions at opposite ends of the companion mass range: planetary and stellar. We present technological advances ranging across the fields of instrumentation, image processing (both real-time and post-processing), and stellar system characterization.

Contents

Chapter 1

Introduction to High-Contrast Imaging

Until recently, exoplanet detection was indirect, mostly through either the transit method or radial velocity (RV) method. The transit method scans stellar lightcurves for periodic dimming indicative of a planetary transit. The RV method searches for periodic shifts in stellar spectral lines caused by a companion wobbling the star's orbit. Both of these methods are sensitive to massive, close-in planets. They also require a specific system alignment: in order to observe a transit, the exoplanet needs to pass between the star and earth. In order to observe spectral line shifts, the orbital plane of the planet needs to line up to some degree with the line-of-sight of the observer. The transit method yields the exoplanet's radius and the RV method yields $M \sin i$, the planet's minimum mass.

High-contrast imaging (HCI), sensitive to large distant planets orbiting around nearby

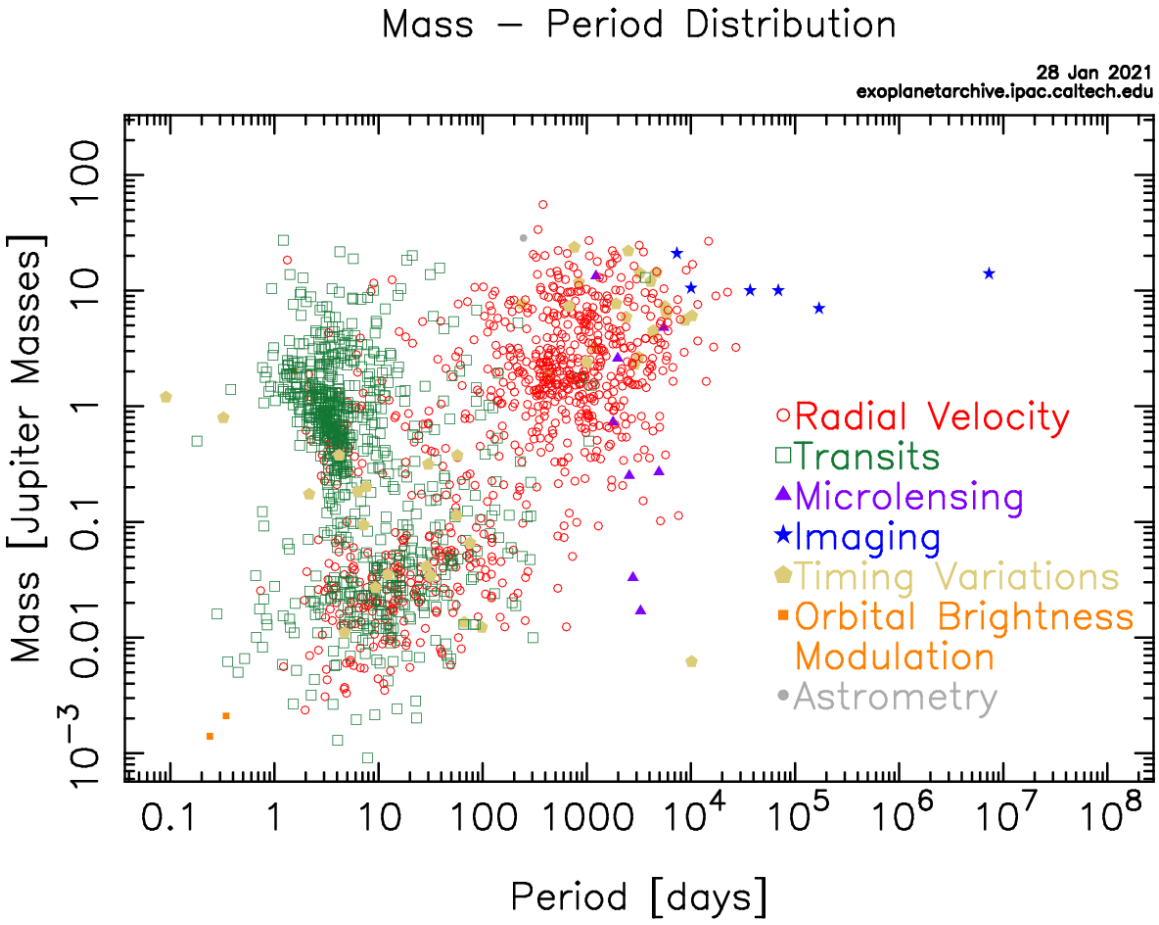

Figure 1.1 Period-mass plot for all $\sim$ 4300 confirmed exoplanets circa January 2021 from https://exoplanetarchive.ipac.caltech.edu. The majority of planets have been found through the radial velocity and transit methods which are sensitive to high-mass planets orbiting close to their host stars. The few planets that have been directly imaged are Jovian in size and far from their host star.

stars, is simultaneously a direct method of exoplanet detection and exoplanet characterization. Direct imaging reveals the planet-star separation. Observing the planet in different wavelengths of light (photometry) yields a rough spectrum, which can be compared to planetary formation models to determine the planet's size and age (e.g. Currie et al., 2011, for the benchmark directly-imaged system HR8799). Provided the instrument is equipped with a spectrograph, a full spectrum can be made to determine the planet's

atmospheric composition (e.g. Konopacky et al., 2013; Barman et al., 2015, again for HR8799). Notable achievements in addition to the direct imaging of four massive planets around star HR8799 (Marois et al., 2008) include the discovery of a giant planet in a young star's disk (Lagrange et al., 2010), and the further discovery and characterization of Jovian planets (Kuzuhara et al., 2013; Macintosh et al., 2015a). For a complete review of the direct imaging of giant planets over the past few decades, see Bowler (2016).

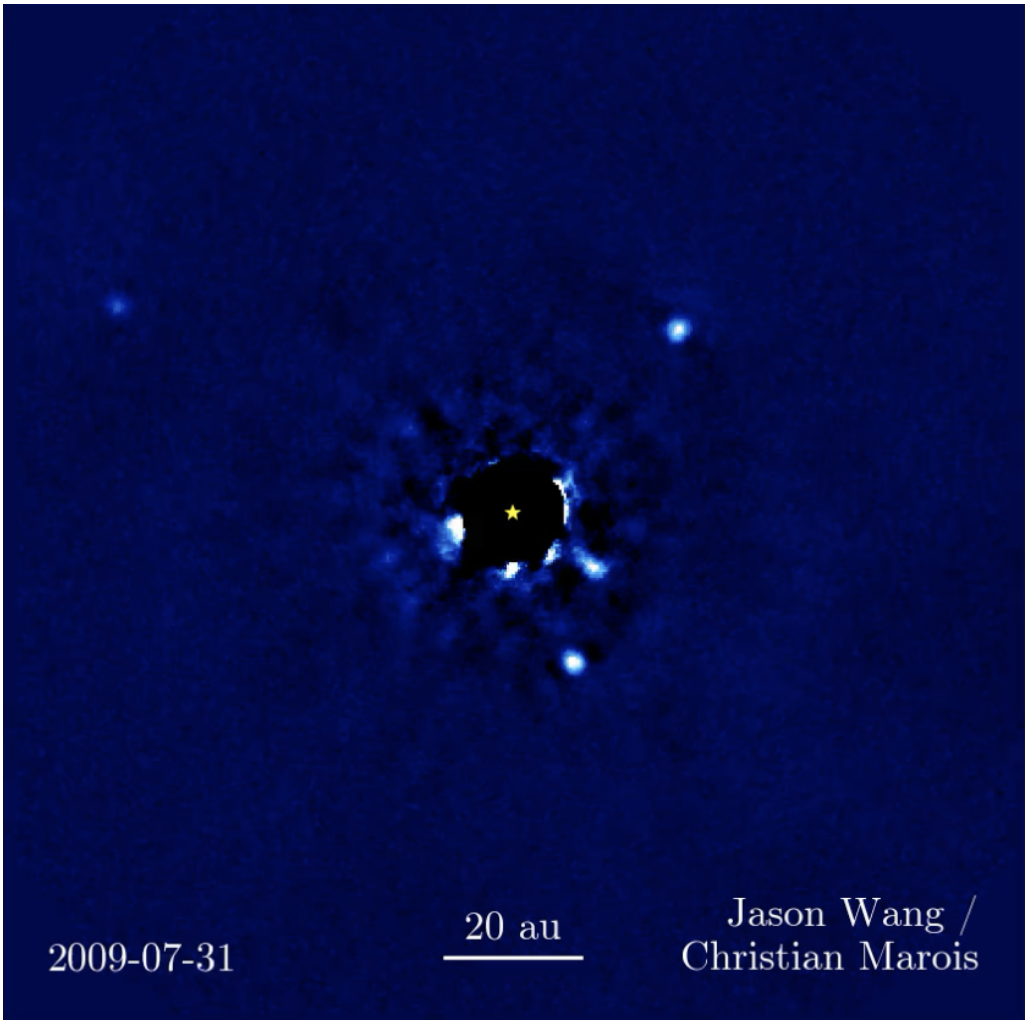

Figure 1.2 HR8799 and its four companions. Image is a still from a movie made by Jason Wang (Caltech) and Christian Marois (NRC Herzberg) compiled from seven years of observations taken with the Keck Telescope.

1.1 HCI Instrumentation and Challenges

The discovery and characterization of exoplanets via direct imaging is particularly challenging due to the extreme contrasts ($<10^{-4}$ for ground based targets) and small angular separations ($\lesssim 1''$) between the planetary companion and its host star. Sophisticated ground-based high-contrast instruments have been, or are being, built including: the Gemini Planet Imager (GPI, Macintosh et al., 2008, 2014), SPHERE at VLT (Carbillet et al., 2011; Beuzit et al., 2019), SCExAO at Subaru (Jovanovic et al., 2015), P1640 (Crepp et al., 2011; Lewis & Oppenheimer, 2017) and the Stellar Double Coronagraph (SDC, Mawet et al., 2014a) at Palomar, the Keck Planet Imager and Characterizer (KPIC) at Keck (Mawet et al., 2016; Jovanovic et al., 2019), and MagAO-X at the Magellan Clay Telescope (Males et al., 2018).

In addition to the planet-star contrast, there's the additional challenge of removing bright quasistatic speckles in our images which can be indistinguishable from substellar companions in their average intensity. In the absence of atmospheric effects, an incoming wavefront can be approximated as a perfect plane at the entrance pupil of the telescope. The telescope aperture performs a Fourier transform on this plane multiplied by the pupil shape. It forms an Airy point-spread function (PSF) in the image plane. However, any small-amplitude sinusoidal ripples in phase imposed on this plane (resulting from atmospheric distortions), will modify this perfect PSF by creating Fourier components in the image plane that appear to be fainter copies of the primary Airy PSF. These will be displaced from the primary PSF by an angle related to inverse of the sinusoidal wave's

frequency across the pupil of the telescope.

An arbitrarily complicated wavefront will generate thousands of these symmetric sets of faint spots, known as speckles, each pair with a different intensity. Their positions are a function of the wavefront perturbations and the wavelength of light observed (speckles are chromatic). They will move around with even a minor change in the incoming wavefront. The result is a highly variable background of correlated noise. Because speckles are correlated, traditional methods to increase signal-to-noise (i.e. increasing exposure times) will not work as the speckles will not average into a smooth background, rather the PSF noise will converge to a quasi-static noise pattern.

High-contrast instruments are equipped with adaptive optics (AO) systems designed to correct the incoming wavefront. An AO system consists of a wavefront sensor and a deformable mirror operating in a control loop to continuously improve the incoming wavefront and to account for the constantly changing atmosphere. Atmospheric speckles still appear in images corrected with AO due to residual wavefront errors resulting from time lag in the AO correction, speed of the AO control loop, non-common path errors, telescope vibrations, and chromaticity between the wavefront and science cameras (Guyon, 2005; Lozi et al., 2018). These speckles evolve on timescales of seconds to minutes (quasistatic speckles). The result is a residual speckle noise background (the *speckle barrier*) that limits the planet-star detection contrast ratio to $\sim 10^{-6}$. In the following sections we discuss techniques to overcome the speckle barrier.

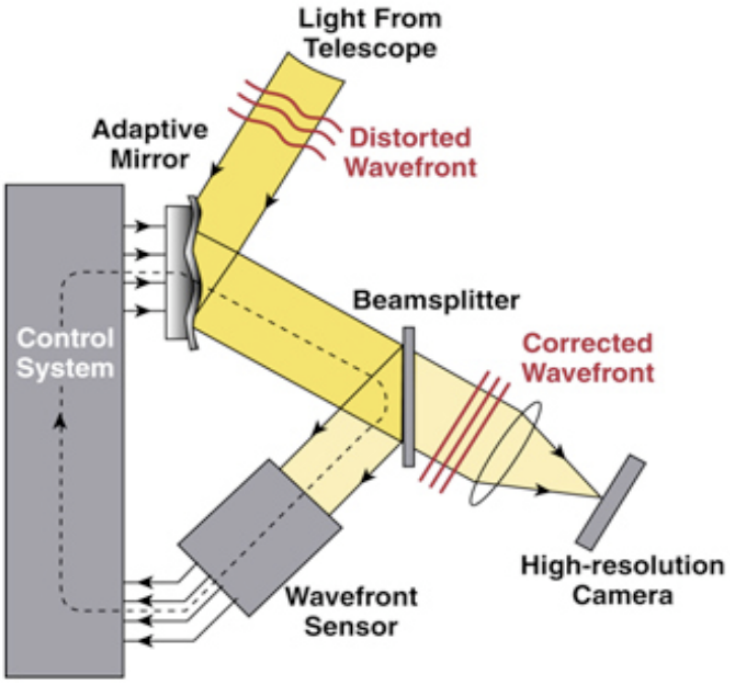

Figure 1.3 The basic feedback loop of an AO system. An aberrated wavefront enters the telescope, bounces off a deformable mirror, and is then split by a beamsplitter. Some of the light is sent to a wavefront sensor that measures the phase distortion of the wavefront and subsequently sends that information to the deformable mirror, commanding it to take a shape such that the wavefront aberrations will cancel out. Cartoon schematic from ucolick.org, courtesy of Lawrence Livermore National Laboratory and NSF Center for Adaptive Optics.

1.1.1 PSF Subtraction

PSF subtraction reduces the stellar quasistatic noise by factors approaching 100 (Marois et al., 2006a). The following techniques for PSF subtraction differ in how they approach the modeling of the stellar PSF. These three techniques exploit properties of quasistatic speckle behavior to generate a reference PSF to subtract off the quasistatic speckle background, leaving behind the substellar companion.

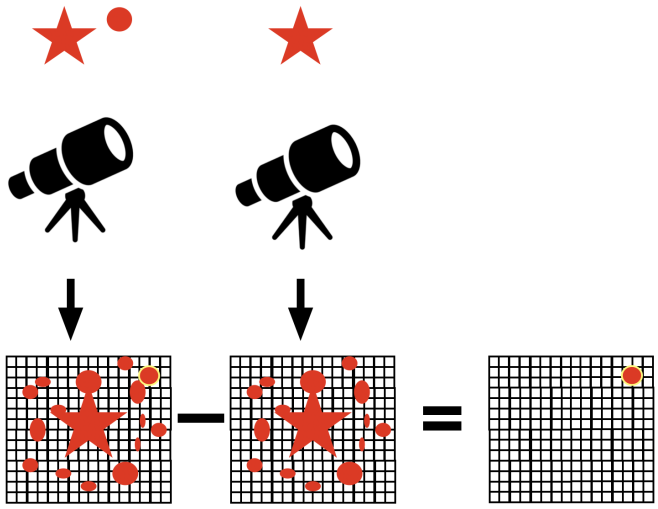

Figure 1.4 Reference Differential Imaging: The model PSF comes from a reference star. Cartoon representation made by I. Lipartito

Reference Differential Imaging (**RDI**, Lafrenière et al., 2009; Soummer et al., 2011; Ruane et al., 2019) uses a reference star PSF as a model. In addition to imaging the high-contrast target, one takes a separate image of a nearby reference star. This reference star's PSF can be directly subtracted from the high-contrast target's stellar PSF, leaving behind just the substellar companion.

Spectral Differential Imaging (**SDI**, Racine et al., 1999; Marois et al., 2000; Sparks & Ford, 2002) is a technique which exploits the chromatic behavior of speckles: unlike stars and planets, speckles move radially outwards with increasing wavelength. SDI is performed on a spectral cube made of N wavelength slices. Each wavelength slice image is scaled to align the quasistatic speckles and combined to create a synthetic PSF which is then subtracted from each scaled image. The images are descaled and combined into a final image which only contains the companion.

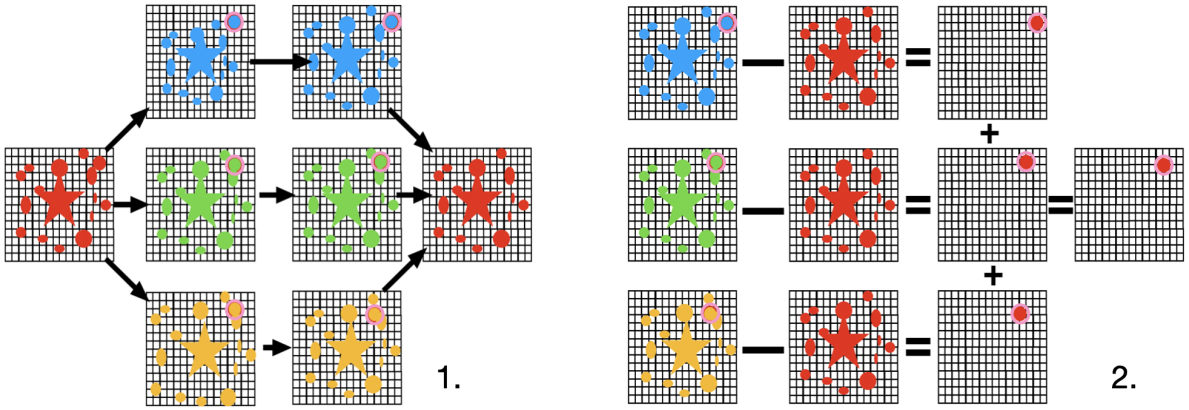

Figure 1.5 Spectral Differential Imaging:
(1) Take a stellar image made using a broadband filter and break it up into a series of images with different wavelengths. Scale each image to have the same stretch so the speckles align and then median-combine them. Now we have a reference PSF without the planet in it.
(2) Subtract the reference PSF from each color image and de-scale. Median-combine them, only the planet should be left over. Cartoon representation made by I. Lipartito

Angular Differential Imaging (**ADI**, Marois et al., 2006b) exploits the rotational invariance of speckles. A series of observations is made using an Alt-Az telescope with its derotator switched off. The Field of View (night sky) will rotate around the stellar PSF due to the rotation of the Earth while speckles will remain 'fixed' in position. ADI is performed on the resulting temporal cube made up of time slices. A synthetic PSF will be made from aligning each image in the temporal cube to a common frame. That reference PSF is then subtracted from each image. Images are derotated and combined into a final image which only contains the companion.

Since the initial development of ADI and SDI, a variety of post-processing algorithms have refined their approaches to push for higher achievable contrasts (e.g. Lafrenière et al., 2007; Soummer et al., 2012; Marois et al., 2014; Gomez Gonzalez, C. A. et al.,

2016). The time variability and chromaticity of quasistatic speckles, however, limit the performance of ADI and SDI which are the best performing current techniques (Gerard et al., 2019). Both of these techniques also suffer at the small angular separations where exoplanets are more likely to be found. The speckle spectral dispersion used by SDI and the arclength traced by the companion's sky rotation used by ADI are both proportional to the planet's separation. Furthermore, the precision of the background estimate for PSF subtraction is limited by low counting statistics at small separations (Mawet et al., 2014b). Even without these issues, the variability induced by speckle fluctuations can dominate over the shot noise expected from the total number of photons.

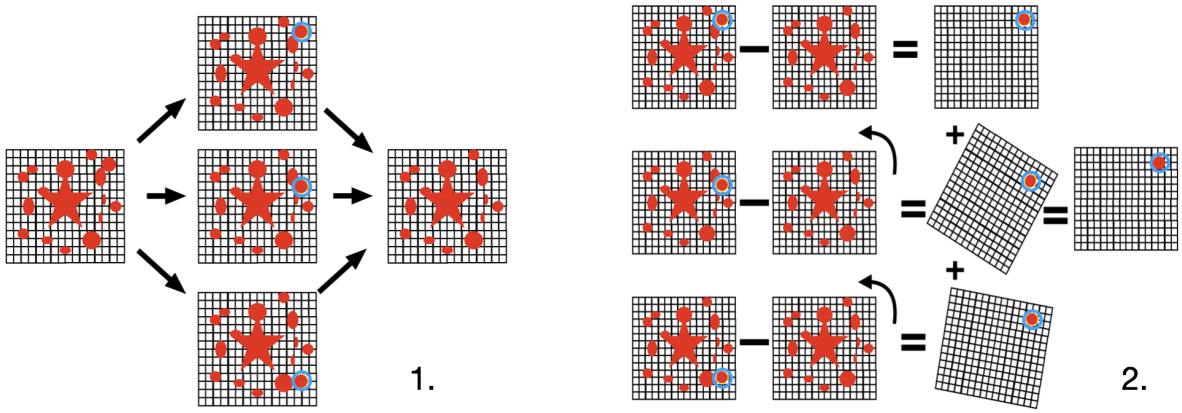

Figure 1.6 Angular Differential Imaging:
(1) Take a series of stellar images made over time, where the planet is rotating around the star and appears in different positions in each image. Median-combine the series of images to obtain a reference PSF without the planet in it.
(2) Subtract the reference PSF from each image in the time series. Derotate and median-combine the images, only the planet should be left over. Cartoon representation made by I. Lipartito

1.1.2 Speckle Nulling

In order to push to higher contrasts (giant planets around M-dwarf stars have a contrast ratio lower than $\sim 10^{-7}$), AO systems need to be supplemented with real-time speckle removal techniques, an example of which is focal plane speckle nulling. This is an iterative technique to sense and null non-common path error speckles in the focal plane using images from the science camera. A quasistatic speckle can be deleted by determining the sinusoidal ripple in the wavefront that caused it and imposing the opposite ripple on the deformable mirror. Bottom et al. (2016a) demonstrated speckle nulling on-sky at low speeds ($<$ 10 Hz, able to remove static and quasistatic speckles) using the Stellar Double Coronagraph (SDC) (Bottom et al., 2016) and the PALM-3000 AO system (P3K) (Dekany et al., 2006; Bouchez et al., 2010), finding factors of 3-6 improvement in contrast. See Jovanovic et al. (2015) (Figure 1.7) for an example of speckle nulling using the SCExAO system at Subaru. Faster control bandwidths (at least 100 Hz) and higher camera frame rates ($\sim$ kHz) are needed in order to remove fast atmospheric speckles.

1.1.3 Speckle Statistical Analysis

A recent development in speckle removal is through speckle arrival timing statistics (Aime & Soummer, 2004; Fitzgerald & Graham, 2006; Soummer et al., 2007; Gladysz & Christou, 2008). The underlying PDF, or probability density function, from which a speckle's intensity is drawn is a Modified Rician (MR). MR distributions are characterized by their static PSF contribution (I_c) and random speckle intensities (I_s). Speckles can be

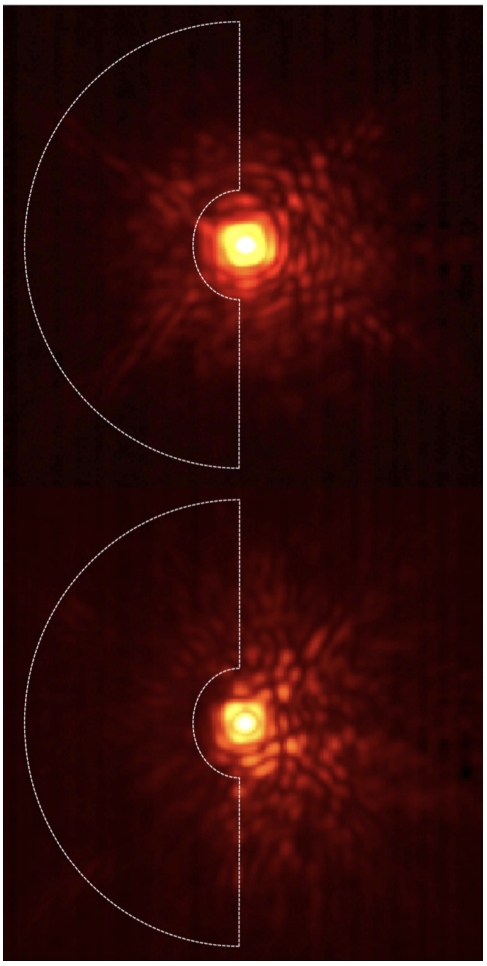

Figure 1.7 From Jovanovic et al. (2015) Top: RX Boo with no speckle nulling applied. Bottom: RX Boo with speckle nulling performed on the region enclosed by the white dashed line using SCExAO.

identified by their skewed MR profiles (lower I_c/I_s ratios) as compared to the Gaussian profile of a potential substellar companion.

The statistics of the wave amplitude in the focal plane of an instrument are described in detail in Aime & Soummer (2004). In short, a wave arriving at the entrance pupil of a telescope consists of a deterministic component representing the perfect plane wave A plus a random term representing the uncorrected part of the wavefront $a(x, y)$, multiplied

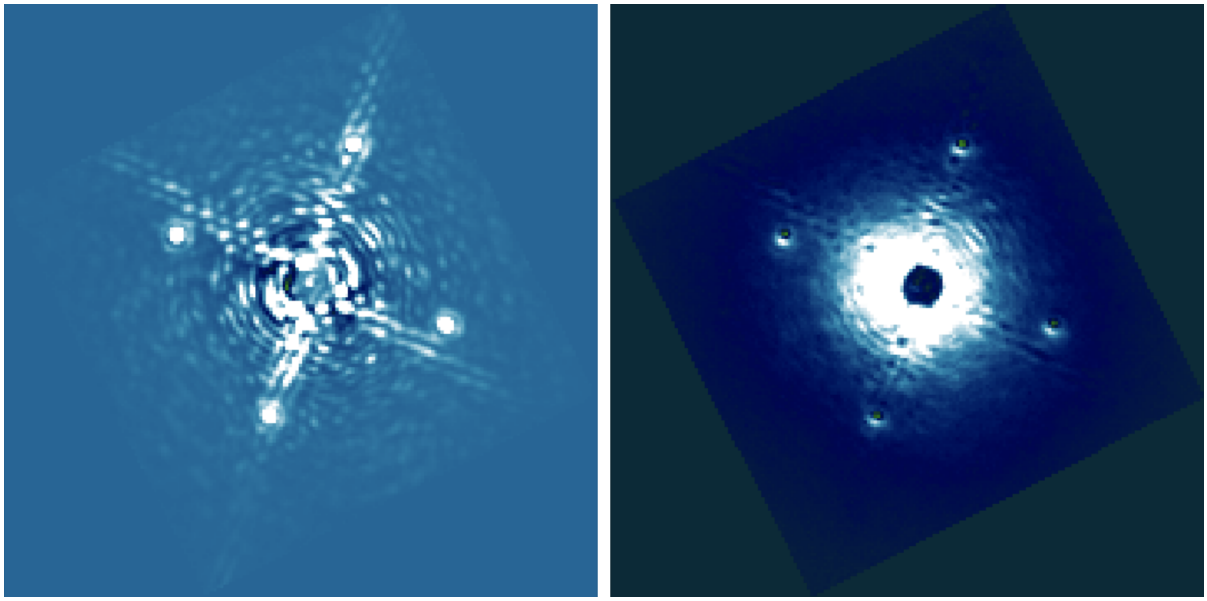

Figure 1.8 Left: Coherent Diffraction Pattern (I_c), Right: Seeing Disk Image (I_s). Images simulated by I. Lipartito from a Coronagraphic High Angular Resolution Imaging Spectrograph (CHARIS) dataset provided by Dr. T. Brandt, private communication

by a telescope aperture transmission function $P(x, y)$. The wavefront amplitude in the pupil plane is therefore:

$$\Psi_I(x, y) = [A + a(x, y)]P(x, y) \tag{1.1}$$

The wavefront amplitude in the focal plane is given by a scaled Fourier Transform (FT) of the pupil plane amplitude:

$$\Psi_{II}(x, y) = A \cdot FT[P(x, y)] + FT[a(x, y)P(x, y)] \tag{1.2}$$

We call $A \cdot FT[P(x, y)]$ the deterministic term $C(x, y)$ (proportional to the perfect wave amplitude of the Airy pattern). We call $FT[a(x, y)P(x, y)]$ the random term $S(x, y)$,

representing the varying speckle pattern. The square of the wavefront amplitude gives us the instantaneous intensity in the focal plane:

$$\Psi_{II}(x,y)^2 = C(x,y)^2 + S(x,y)^2 + 2Re[C^*(x,y)S(x,y)] \tag{1.3}$$

The average intensity in the focal plane is given by:

$$\langle \Psi_{II}(x,y)^2 \rangle = |C(x,y)^2| + \langle |S(x,y)^2| \rangle \tag{1.4}$$

I_c is $|C(x,y)^2|$, the intensity of the coherent part of the wavefront, and I_s is $\langle |S(x,y)^2| \rangle$, the intensity of the speckle part of the wavefront. The variance of the intensity has a contribution from both of these components of the wavefront: $\sigma_c^2 = (2I_sI_c + I_c)$ and $\sigma_s^2 = (I_s^2 + I_s)$:

$$\sigma^2 = (2I_sI_c + I_c) + (I_s^2 + I_s) \tag{1.5}$$

The mean intensity is given by the sum of the mean coherent and speckle components of the wavefront:

$$\mu_I = I_c + I_s \tag{1.6}$$

Finally, the probability density function (PDF) of the intensity takes the form of a

modified Rician (MR) distribution:

$$\rho_{\mathrm{MR}}(I) = \frac{1}{I_c} \exp\left(-\frac{I + I_c}{I_s}\right) I_0\left(\frac{2\sqrt{I}\sqrt{I_c}}{I_s}\right) \tag{1.7}$$

Speckles have a MR-distribution PDF whereas an astronomical source (planet or faint stellar companion) will obey Poisson statistics, giving it a characteristic shape closer to that of a Gaussian curve. Statistical Speckle Distribution (SSD) is the practice of characterizing these distributions to separate a planet from speckles. By looking at the intensity histograms of different astronomical phenomena, we can determine if they come from planets or speckles. Meeker et al. (2018) demonstrated SSD on-sky for star system 32 Peg using the DARKNESS instrument at Palomar (Figure 1.9).

1.2 MKIDs for High-Contrast Imaging

A significant improvement over existing systems can be achieved by using read-noise free time domain information on short enough timescales to sample and control, or remove in post-processing, the fast speckle fluctuations from imperfections in the AO system and non-common path aberrations. The Mazin group develops exoplanet cameras such as the MKID Exoplanet Camera (MEC) for this purpose - to serve as both a photon counting, energy resolving science camera, and as a focal plane wavefront sensor to correct for chromatic wavefront errors not accounted for by the upstream AO system. To achieve this, a high-speed, noise-free detector is required, for example, a Microwave Kinetic

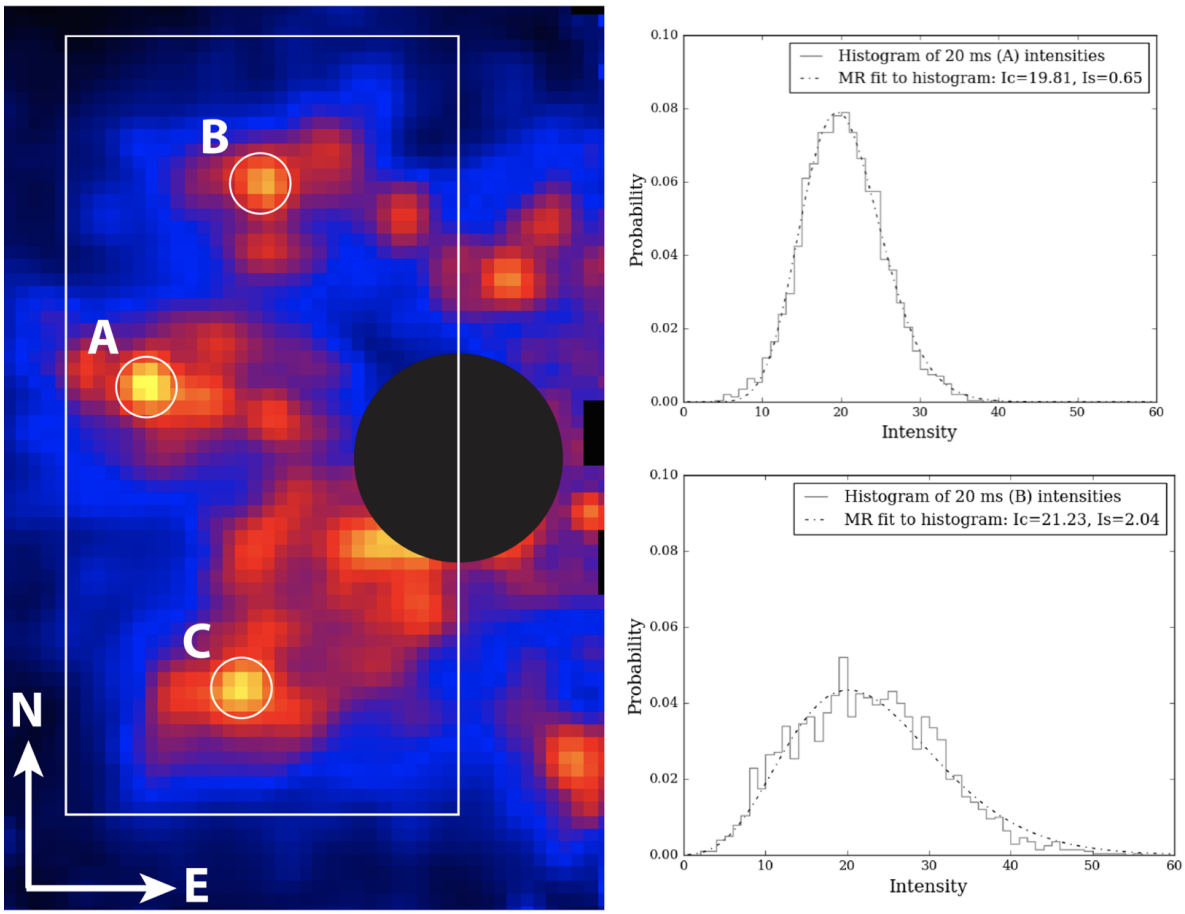

Figure 1.9 From Meeker et al. (2018). Left: Median 1-second J-band image of 32 Peg Ab (at location A) and satellite speckles (locations B, C). Star system 32 Peg imaged by the DARKNESS MKID-based high-contrast instrument in conjunction with the PALM-3000 Adaptive Optics Instrument. The satellite speckles are generated by placing two sine wave shapes on the deformable mirror. Right: Intensity histograms from two-thousand 20 ms exposures for 32 Peg Ab (top panel) and a satellite speckle (bottom panels). Intensity units are photon counts in each aperture per 20 ms frame. The satellite speckle and stellar companion have different intensity histograms.

Inductance Detector Array.

1.2.1 Optical and Infrared (OIR) MKID Arrays

The 'pixels' of the Mazin Lab cameras are Microwave Kinetic Inductance Detectors, or MKIDs, which are low temperature superconducting resonant LC circuits. MKIDs work on the principle that incident photons change the surface impedance of a superconductor through the kinetic inductance effect. The kinetic inductance effect occurs because energy can be stored in the supercurrent (the flow of Cooper Pairs) of a superconductor. Reversing the direction of the supercurrent requires extracting the kinetic energy stored in it, which yields an extra inductance term in addition to the familiar geometric inductance. The magnitude of the change in surface impedance depends on the number of Cooper Pairs broken by incident photons, and is proportional to the amount of energy deposited in the superconductor. This change can be accurately measured by placing a superconducting inductor in a lithographed resonator. A microwave probe signal is tuned to the resonant frequency of the resonator and any photons which are absorbed in the inductor will imprint their signature as changes in the phase and amplitude of this probe signal.

Since the quality factor, Q, of the resonators is high, and their transmission off resonance is nearly perfect, multiplexing can be accomplished by tuning each pixel to a different resonant frequency with lithography during device fabrication. A comb of probe signals is sent into the device and room temperature electronics recover the changes in amplitude and phase. This makes a device capable of measuring the arrival time (to a microsecond) and energy (to 5-10%) of each arriving photon without read noise or dark

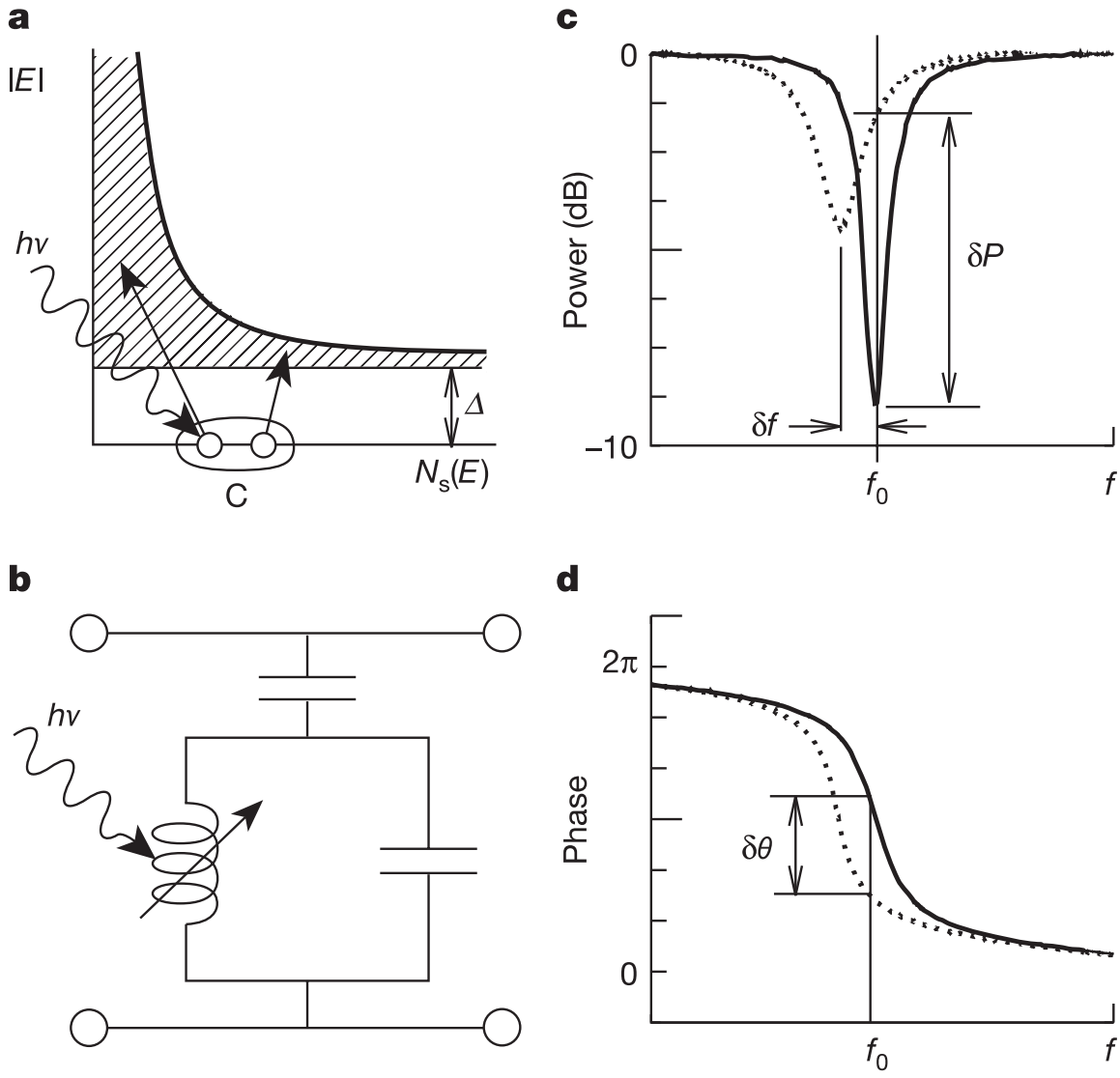

Figure 1.10 The basic operation of an MKID, from Day et al. (2003). (a) Photons with energy $h\nu$ are absorbed in a superconducting film producing a number of excitations called quasiparticles. (b) To sensitively measure these quasiparticles the film is placed in a high frequency planar resonant circuit. The amplitude (c) and phase (d) of a microwave excitation signal sent through the resonator. The change in the surface impedance of the film following a photon absorption event pushes the resonance to lower frequency and changes its amplitude. If the detector (resonator) is excited with a constant on-resonance microwave signal, the energy of the absorbed photon can be determined by measuring the degree of phase and amplitude shift.

current; an optical/near-IR analog of an X-ray microcalorimeter. More details on MKIDs can be found in Mazin et al. (2012, 2013a) and in Figure 1.10.

MKID pixels are 'read out' continuously while exposing, there is no loss of active exposure time to readout. These detectors are well-suited to track atmospheric aberrations which evolve on too rapid a timescale to be removed with PSF subtraction.

1.2.2 MKID Instruments

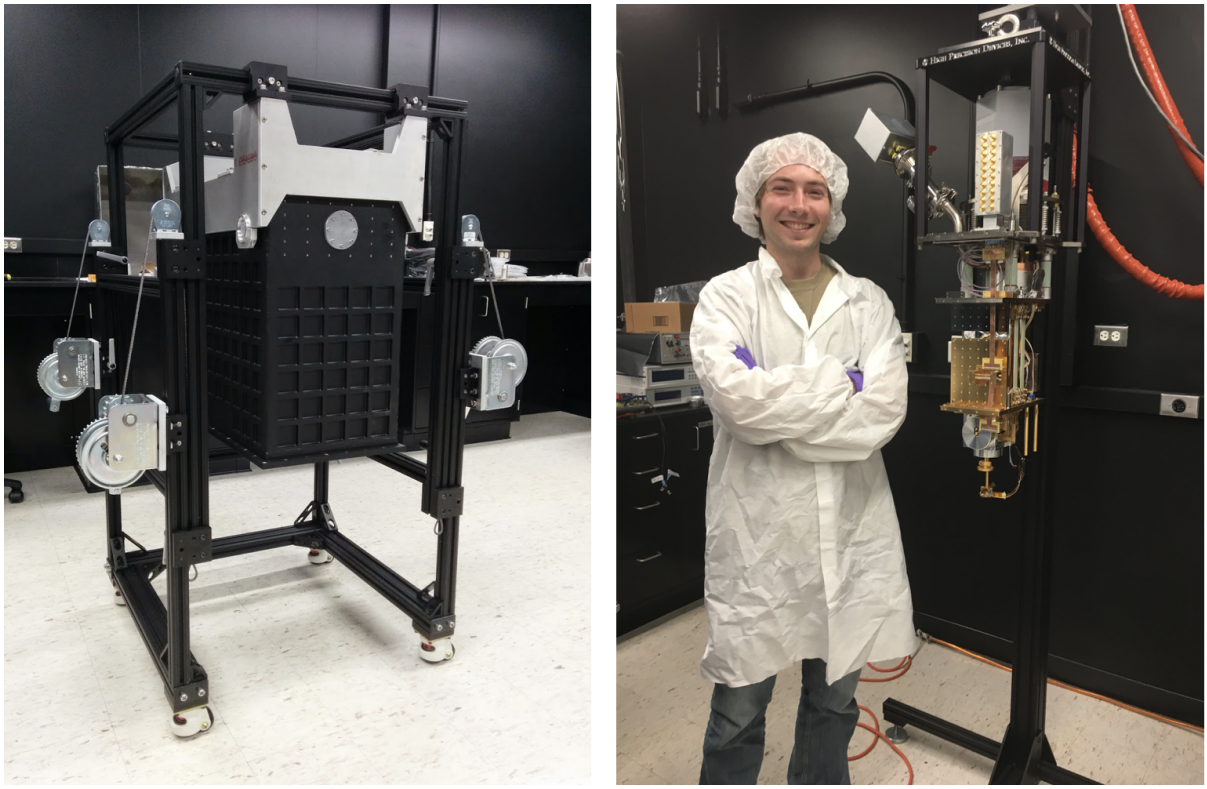

Figure 1.11 Two MKID Cameras: (Left) DARKNESS in its shell. Picture courtesy of Dr. Seth Meeker (Right) MEC outside its shell with Dr. Alex Walter. Picture taken by I. Lipartito

The Mazin group has built and commissioned three MKID-based cameras: ARCONS (the Array Camera for Optical to Near-IR Spectrophotometry), DARKNESS

(the DARK-speckle Near-infrared Energy-resolving Superconducting Spectrophotometer), and MEC (the MKID Exoplanet Camera). Previous studies using ARCONS include a search for optical pulsations in the millisecond pulsar J0337+1715 (Strader et al., 2016), and light-curve analysis of AM CVn stars (Szypryt et al., 2014). DARKNESS was commissioned in July 2016 and has been deployed in conjunction with the Stellar Double Coronograph and PALM-3000 Adaptive Optics system at Palomar Observatory to observe binary star systems, and stars with known substellar or exoplanet companions (i.e. HR8799, Delta And). I brought DARKNESS back and forth to Palomar Observatory and installed it along with its electronics for nights of observations, spending weeks beforehand testing the readout and also integrating DARKNESS with the in-house adaptive optics system, P3K.

Part of developing instrumentation for astronomy means managing both the front end of instrumentation (instrument testing, building electronics, calibration) with the back end (software and pipeline development, characterizing the ability of the instrument, data reduction). In the next two chapters, we present the instrumentation of and science enabled by MKID-based instruments.

In the first chapter, we present The MKID Exoplanet Camera (MEC), which I helped build and commission. MEC is permanently installed at the Subaru Telescope on the summit of Mauna Kea in Hawaii. This instrument has a 0.8–1.4 micron infrared observing band and works in conjunction with the Subaru Coronagraphic Extreme Adaptive Optics instrument (SCExAO). We discuss MEC's cryostat, optics, and integration with

SCExAO. We also present a second generation digital readout system for photon counting microwave kinetic inductance detector (MKID) arrays operating in the optical and near-IR wavelength bands. This readout system, which I assembled and tested, is currently used by MEC.

In the second chapter we discuss the current performance and contrast limits of MEC+SCExAO, as well as the data reduction pipeline for MEC data. I was part of the team developing the MKID Data Reduction Pipeline, writing the flat calibration section and the hot pixel-masking section. I identified which algorithms were computation-heavy and could be optimized. We adapted traditional high-contrast imaging techniques (Angular Differential Imaging, Spectral Differential Imaging) to work with MKID data. In 2016, we started imaging already known planets like Kappa And B and HR 8799 using DARKNESS, and in 2019 we started imaging these planet and debris disks using MEC. I spent hundreds of hours trying to coax a planet or debris disk out of our data for both DARKNESS and MEC observations, but as of 2019, our cameras did not have the contrast levels required to image high-contrast targets. I explain the characterization of the contrast limits of the MKID Exoplanet Camera.

MEC+SCExAO have the capability for imaging starlight reflected off exoplanets, opening up a wider parameter space of imageable planets than that allowed by thermal imaging. We conclude by discussing future plans and science goals for this system.

Chapter 2

MEC: The MKID Exoplanet Camera for Subaru SCExAO

In this chapter we discuss the instrument details of the MKID Exoplanet Camera (MEC), a z through J band (800–1400 nm) integral field spectrograph located behind The Subaru Coronagraphic Extreme Adaptive Optics (SCExAO) instrument at the Subaru Telescope on Maunakea that utilizes Microwave Kinetic Inductance Detectors (MKIDs) as the enabling technology for high-contrast imaging. This work was published in Walter et al. (2020) and Fruitwala et al. (2020).

MEC is the first permanently deployed near-infrared MKID instrument and is designed to operate both as an IFU, and as a focal plane wavefront sensor in a multi-kHz feedback loop with SCExAO. The read-noise free, fast time domain information attainable by MKIDs allows for the direct probing of fast speckle fluctuations that currently

limit the performance of most high-contrast imaging systems on the ground and will help MEC achieve its ultimate goal of reaching contrasts of 10^{-7} at 2 λ/D. MEC was commissioned at Subaru Observatory in 2018. MEC's requirements were based on the delivered optical beam from SCExAO, the available space to mount MEC to SCExAO, the performance of the MKIDs, and the available budget. This resulted in a design with the instrument parameters that are summarized in Table 2.1.

Parameters	Values
Device Materials	PtSi on Sapphire w/ Nb g.p.
Device Format	140x146 pixels (10 feedlines)
Pixel Pitch	150 μm
Plate Scale	10.4 mas/pixel
Field of View	1.4" x 1.5"
Wavelength Band	800-1400 nm (z - J)
Spectral Resolution ($\lambda/\Delta\lambda$)	5-7
Max Count Rate	5000 cts/pix/second
Pixel Dead Time	10 μs
Readout Frame Rate	>2 kHz
Operating Temp.	90 mK
4 K Stage Base Temp.	3.1 K
60 K Stage Base Temp.	57 K
90 mK Hold Time	>17 hours

Table 2.1 MEC Instrument Summary

The MEC MKID array has 10 coplanar waveguide (CPW) transmission lines, or feedlines, that each probe 14 x 146 pixels for a total of 20440 pixels in the array. This makes it the largest superconducting detector in the world. It uses the PtSi MKIDs described in Szypryt et al. (2017), which are optimized for 800-1400 nm light with a spectral resolution of about $\lambda/\Delta\lambda = 6$. The pixels are on a 150 μm pitch, see Figure 2.1. The device currently in MEC has 7/10 feed lines with good transmission and on those there is about an 80% pixel yield.

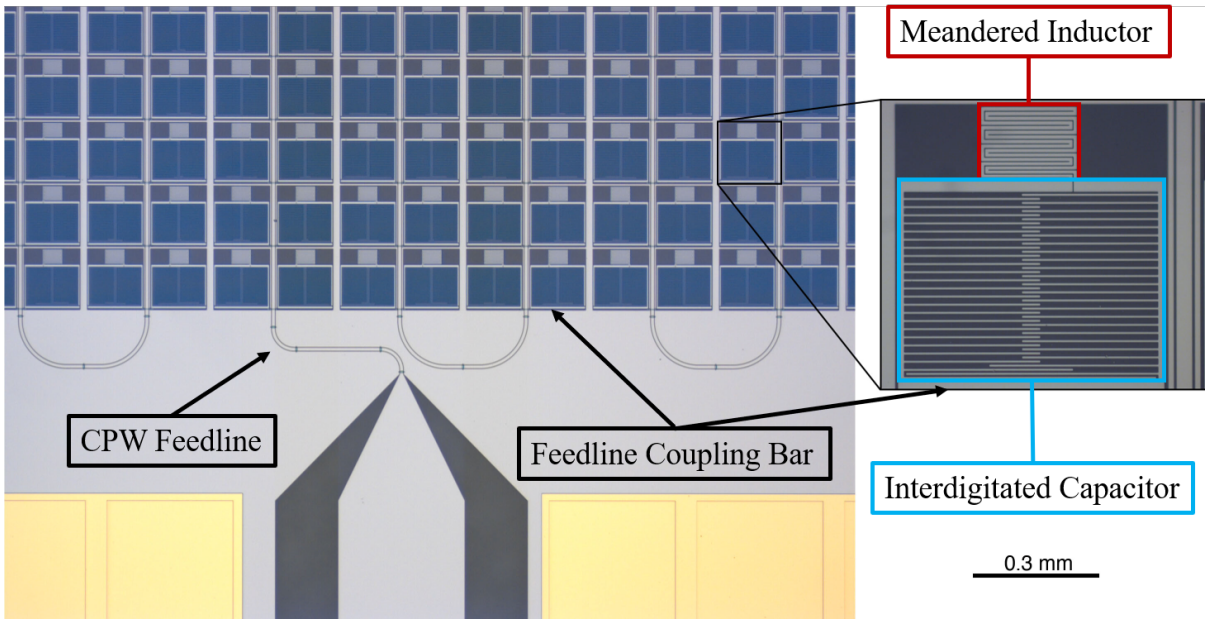

Figure 2.1 Microscope image of a small section of a 20 kpix MKID array similar to the engineering array in the MEC instrument. Left: A coplanar waveguide (CPW) feedline with crossovers connects to a grid of MKID pixels. Gold thermal pads are shown at the bottom. Right: Zoomed-in picture showing the large interdigitated capacitor, meandered inductor, and the feedline coupling bar (bottom right corner).

2.1 Cryostat

MEC's cryostat is a pulse tube cooled Adiabatic Demagnetization Refrigerator (ADR) capable of reaching temperatures below 50 mK. The outer vacuum shell 300 K enclosure measures roughly 22 cm wide x 33 cm deep x 96 cm tall. It contains RF gaskets to reduce radio frequency interference, a 7.5 kW pulse tube, and all the vacuum and wiring connections to accommodate a 20 kpix MKID array. The open MEC cryostat can be seen in Figures 1.11 and 2.2.

The 60 K shell is cooled by the first stage of the pulse tube. It contains heat sinks to cool the wiring to reduce heat load on the 4 K stage. The 4 K stage is cooled by the

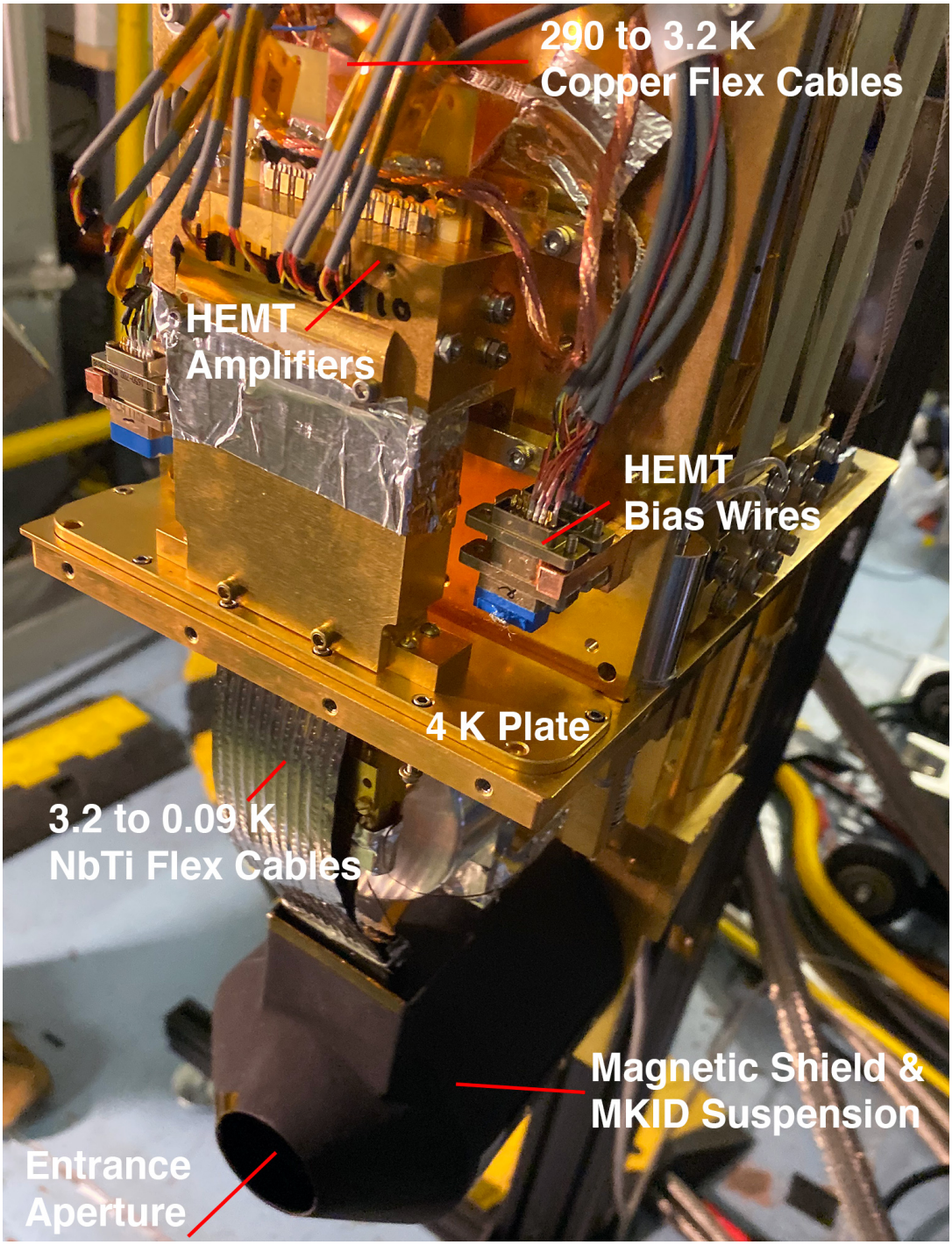

Figure 2.2 Image of the 4 K stage of MEC with the radiation shields removed to show the readout wiring and the black magnetic shield. The pulse tube and heat switch are hidden by the wiring attachment plate.

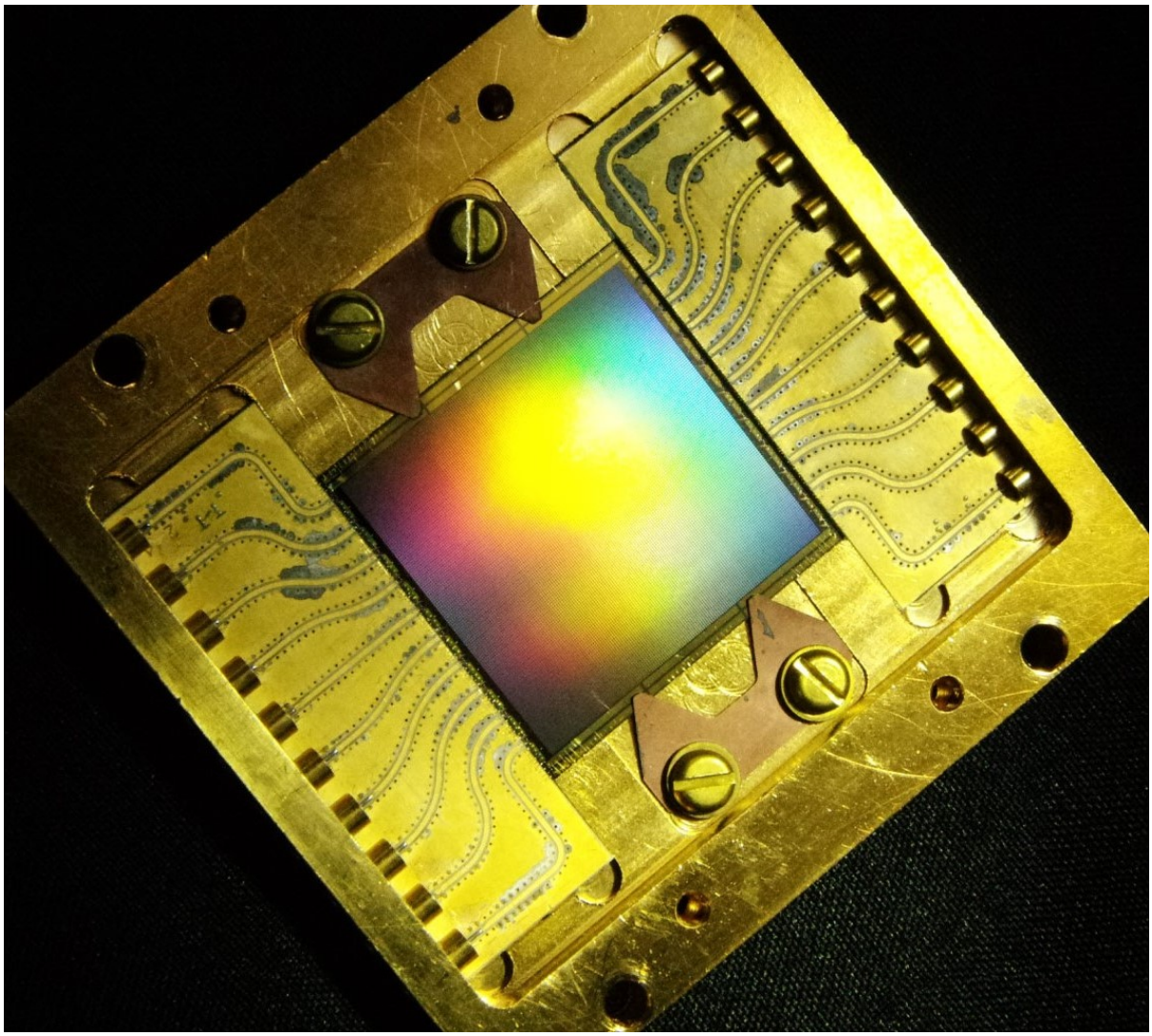

Figure 2.3 Image of a 20440 pixel PtSi MKID device designed for MEC. This is the highest pixel count superconducting detector array at any wavelength. Image credit: Clinton Bockstiegel

second stage of the pulse tube, and has 0.75 W of cooling power at 4 K.

Attached to the 4 K plate (shown in Figure 2.2) are: the ADR unit with the mechanical heat-switch, the ten cryogenic high-electron-mobility transistor (HEMT) amplifiers, and the detector package. The detector package is mounted to the 4 K plate and is

enclosed in a 4 K magnetic shield. This design places the MKID array far from the magnetic shield opening where field leakage will be strongest and also allows us to install a 1 K, 9 cm long black baffle to further reduce off-axis scattered light and 4 K black body radiation. The MKID array is mounted in a microwave package 5 cm x 5 cm x 0.5 cm in size, as shown in Figure 2.3. This box is attached to a gold-plated copper rod that sticks out of the base of the magnetic shield and connects to the ADR unit by a copper strap.

The ADR acts as a single-shot magnetic cooler which brings the MKID array down to 90 mK where the temperature is stabilized with a feedback loop to the ADR magnet power supply. We achieve a 90 mK hold time of >17 hours on the telescope, more than sufficient for the 13-14 hours required for a night of calibration and on-sky observations.

2.2 Optics

2.2.1 Specifications of Incoming Beam

The SCExAO exit beam is located 293±1 mm from the top of the top mounting rail. The beam comes off the bench at about 58 mm from the left edge of the bench. The SCExAO exit beam is collimated. The pupil position is 54±20 mm from the back of the bench. The pupil size is 8.67±0.15 mm. The beam is expected to exhibit <10 nm of chromatic RMS optical wavefront error over the 0.8-1.4 μm bandwidth.

Table 2.2 MEC Optics

#	Optic	Description
1	100 mm FL lens	Thorlabs AC254-100-c
2	9 mm FL lens	Edmunds 45-783
3	2.54 mm gold mirror	Mnt. on CONEX-AG-M100D
4	5.08 mm gold mirror	Fixed mount
5	300 mm FL lens	Thorlabs AC508-300-c
6	2 in ND Filter wheel	See Table 2.3
7	Front Window	Edmund 48-130
8	60 K IR filter	10 mm thick N-BK7
9	4 K IR filter	20 mm thick N-BK7
10	Microlens Array	aμs APO-GT-P150-R0.8

2.2.2 MEC Fore-Optics

The MEC optics box has a two inch hole for the incoming SCExAO beam (Figure 2.4). A set of three lenses creates a telecentric beam designed to reimage the focus onto the MKID array as simulated in Zemax. The beam leaves the optics box with an f-number $f/377.7$, travels through the neutral density (ND) filter wheel (Table 2.3), and enters the cryostat through the front vacuum window. Two IR bandpass filters at the 60 K and 4 K shield block black body radiation and finally a microlens array focuses the beam onto the light sensitive part of the MKID pixels. The MEC optics are listed in Table 2.2.

Table 2.3 MEC Neutral Density Filter Wheel

Slot	Filter	Part #
1	OPEN	
2	0.5 OD	Edmund 62-673
3	1.0 OD	Edmund 62-676
4	2.5 OD	Edmund 62-680
5	CLOSED	

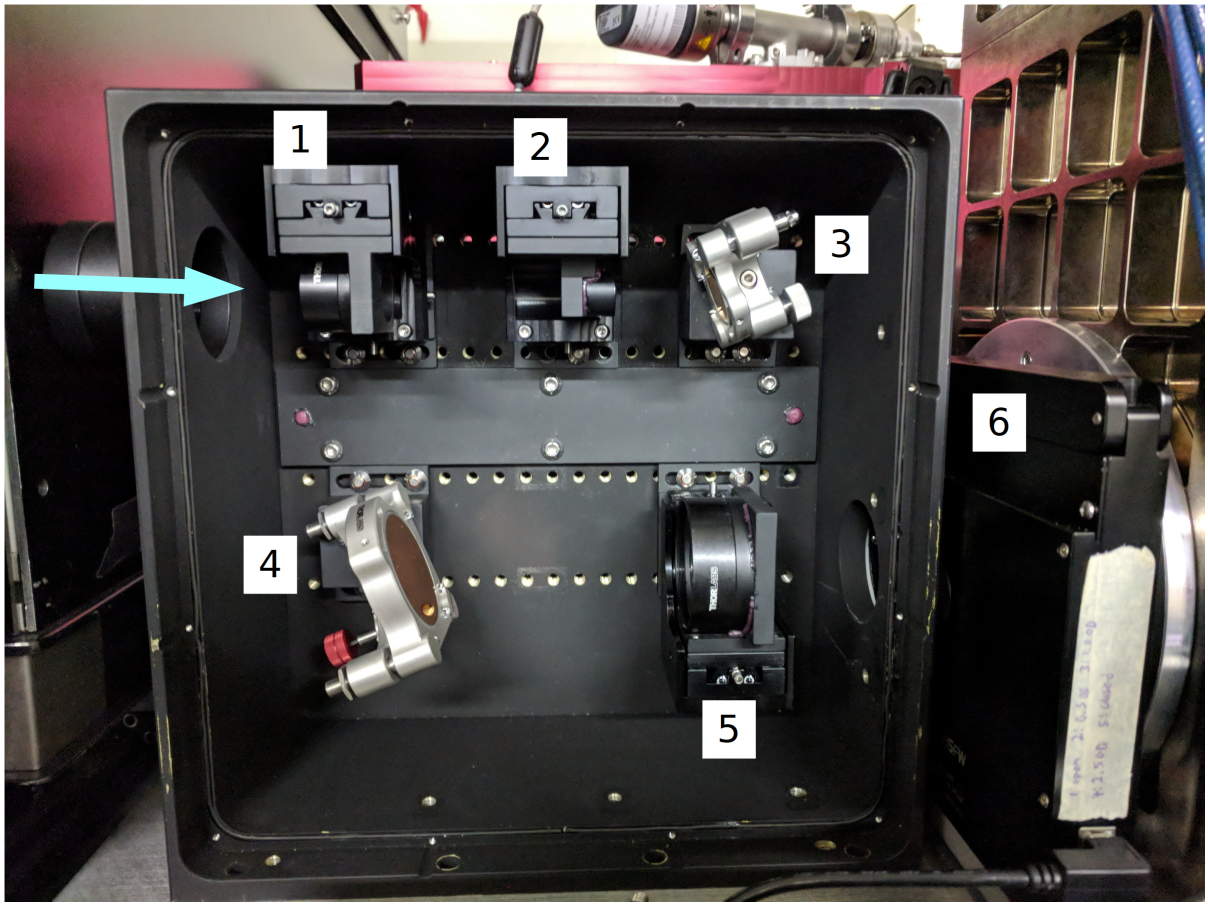

Figure 2.4 The MEC foreoptics box reimages the beam from SCExAO (arrow from left) onto the MKID device. Two gold mirrors (3 and 4) and three lenses (1, 2 and 5) steer and focus the input collimated beam onto the MKID array with an f-number of f/377.7. The specific optics components can be found with their corresponding numbers in Table 2.2.

2.3 Integration with SCExAO

As of March 19, 2018, MEC is mounted on the Nasmyth platform behind SCExAO in the place of the High-Contrast Coronographic Imager for Adaptive Optics (HiCIAO; Hodapp et al., 2008). The electronics rack (discussed in Section 2.4) is stationed next to MEC on the Nasmyth floor. A He compressor is located in the IR compressor room on the observation floor and a linux server is in the server room on the first floor of the control

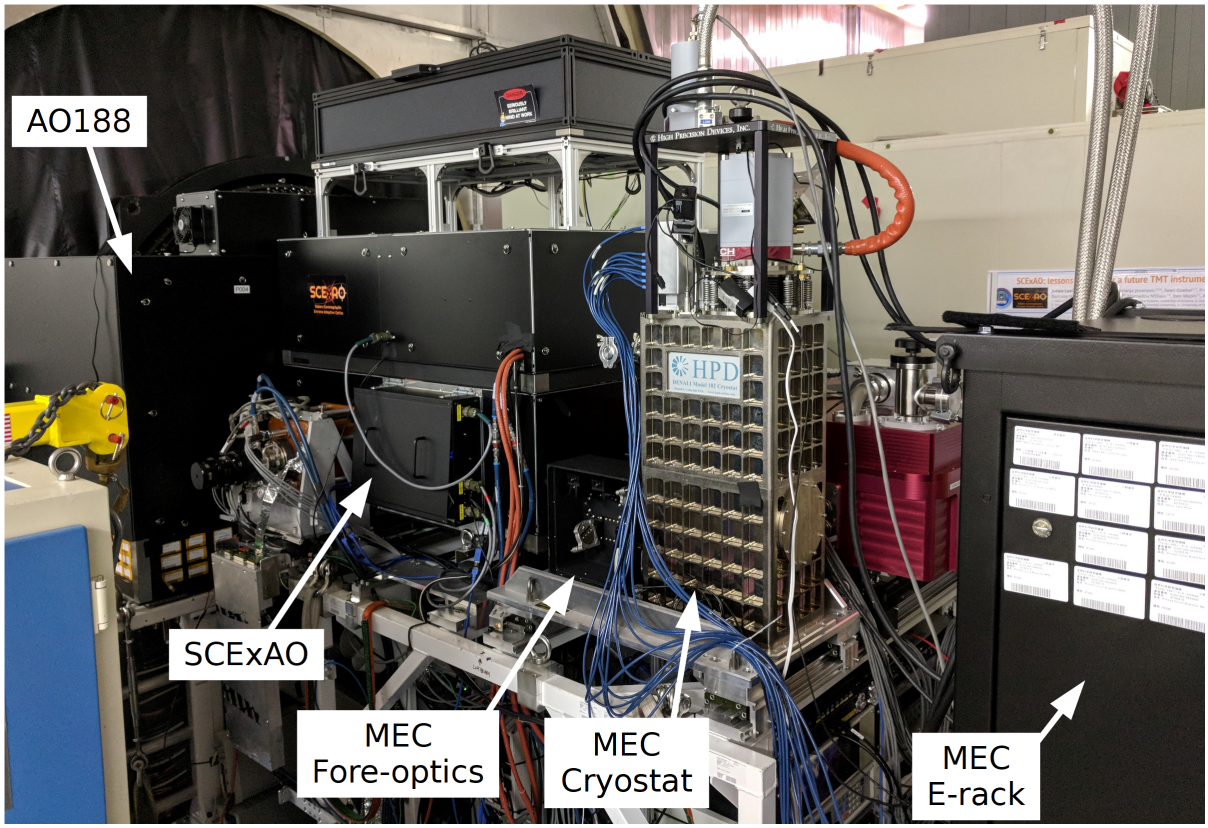

Figure 2.5 MEC is mounted behind the SCExAO bench and AO188 facility adaptive optics systems on the IR Nasmyth port at Subaru Telescope.

building. Figure 2.6 diagrams how MEC is situated on the Nasmyth floor. Figure 2.5 is an image of MEC mounted at the telescope.

2.4 Readout

One of the primary advantages of MKIDs over other superconducting detector technologies is the intrinsic frequency domain multiplexibility; each MKID pixel is a microwave frequency resonator with a resonant frequency that can be easily tuned in fabrication. This allows large numbers of resonators, each tuned to a different frequency, to be placed

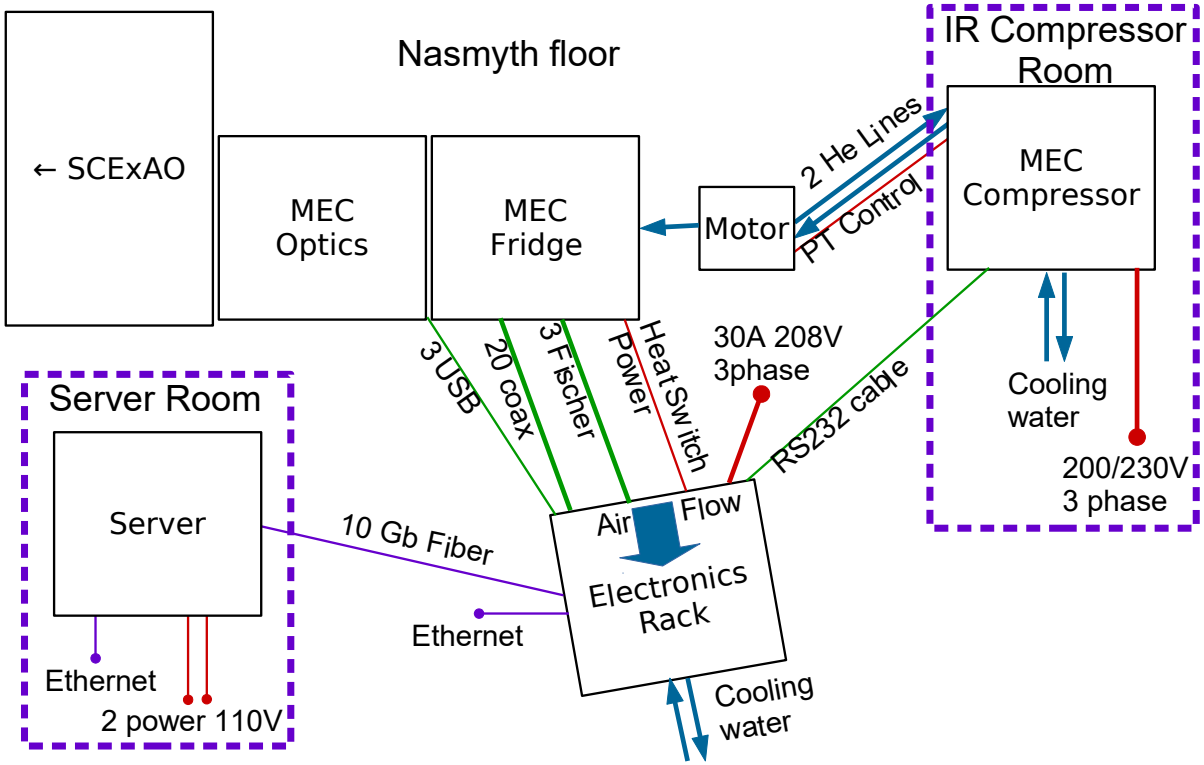

Figure 2.6 A diagram showing the MEC floor plan and interconnects at the Subaru Telescope. Here, red lines denote power connections, blue lines/arrows denote cooling lines, green lines denote electrical cabling and purple lines denote network connections.

in parallel on a single microwave channel. This greatly simplifies the cryogenic wiring and electronics, shifting the complexity to the room temperature readout system (Mazin et al., 2002, 2013b; Meeker et al., 2018; Walter et al., 2018). The readout system is responsible for generating the RF frequency comb to drive the resonators, and for digitizing and processing the resulting MKID array output to determine the arrival time energy of any incident photons.

A first generation readout for optical MKIDs was developed in 2011 for the ARCONS instrument. This system is capable of reading out 256 channels in a 512 MHz band on each readout board (McHugh et al., 2012). Eight boards were used simultaneously to

readout the 2048 pixel ARCONS instrument. In order to feasibly scale up to the kilopixel arrays used by the second generation of optical MKID instruments, we have developed a new readout system capable of reading out up to 1024 channels per unit over 2 GHz of bandwidth. This system largely retains the signal processing algorithm chain found in the first generation readout, albeit with major changes to the hardware and firmware to accommodate the higher bandwidth. As in the first generation readout, our system is capable of identifying, analyzing, and recording photon detection events in real time with a time resolution of order a few microseconds. Here we discuss the this readout system and how it fits in with the MEC+SCExAO system architecture.

2.4.1 System Overview

The full readout system consists of several readout units, each of which can read out up to 1024 resonator channels in a 2 GHz band. Two such units can be placed in parallel to read out a full 4 GHz feedline. Each readout unit has three major components: 1) a CASPER (Collaboration for Astronomy Signal Processing and Electronics Research) ROACH-2 (Reconfigurable Open Architecture Computing Hardware) board with a Xilinx Virtex-6 FPGA for channelization and pulse detection, 2) an Analog to Digital/Digital to Analog Converter (ADC/DAC) board with dual 2 GSPS Analog Devices AD9625 ADCs and AD9136 DACs and Xilinx Virtex-7 FPGA for control, and 3) a Radio Frequency/Intermediate Frequency (RF/IF) board for IQ modulation. The ADC/DAC and RF/IF boards are developed by Fermilab specifically for UCSB MKID arrays.

2.4.2 Electronics Rack

The electronics rack (E-rack) holding the readout system is situated on the Nasmyth platform next to the MEC instrument (Figure 2.7). It requires 3.5 kW max of power supplied to the power distribution unit with a 30 A, 208 V 3-phase power cord. Cooling water/glycol is supplied to the E-rack by Subaru. There should be unobstructed air flow to two readout crates in the electronics rack. The front (facing SCExAO) draws air in, and the back expels air through a heat exchanger into the Nasmyth room.

The MEC readout employs twenty second generation CASPER ROACH-2 boards. Each of these ROACH-2 boards are connected to an ADC/DAC board and a RF/IF board (See Figure 2.9 for one board set, also known as a readout unit). Every ROACH-2 houses a Xilinx Virtex6 Field Programmable Gate Array (FPGA), which processes and channelizes the signal from the ADC using a scaled-up version of the ARCONS firmware. The ADC/DAC board houses a Virtex7 FPGA. An external 10 MHz reference signal is used to synchronize all clocks required by the ADCs, DACs, and FPGAs on both the ROACH-2 and ADC/DAC boards.

The ROACH-2 boards are connected to the ADC/DAC boards by two Z-DOK connectors which are responsible for sending the ADC output and clock signals to the ROACH-2, and for implementing an SPI communications interface between the Virtex-6 and Virtex-7 FPGAs. The RF/IF boards are mounted on the ADC/DAC boards using SMP blind-mate connectors for signals and GPIO pins for programming. Each set of boards reads out 1024 pixels in 2 GHz of bandwidth.

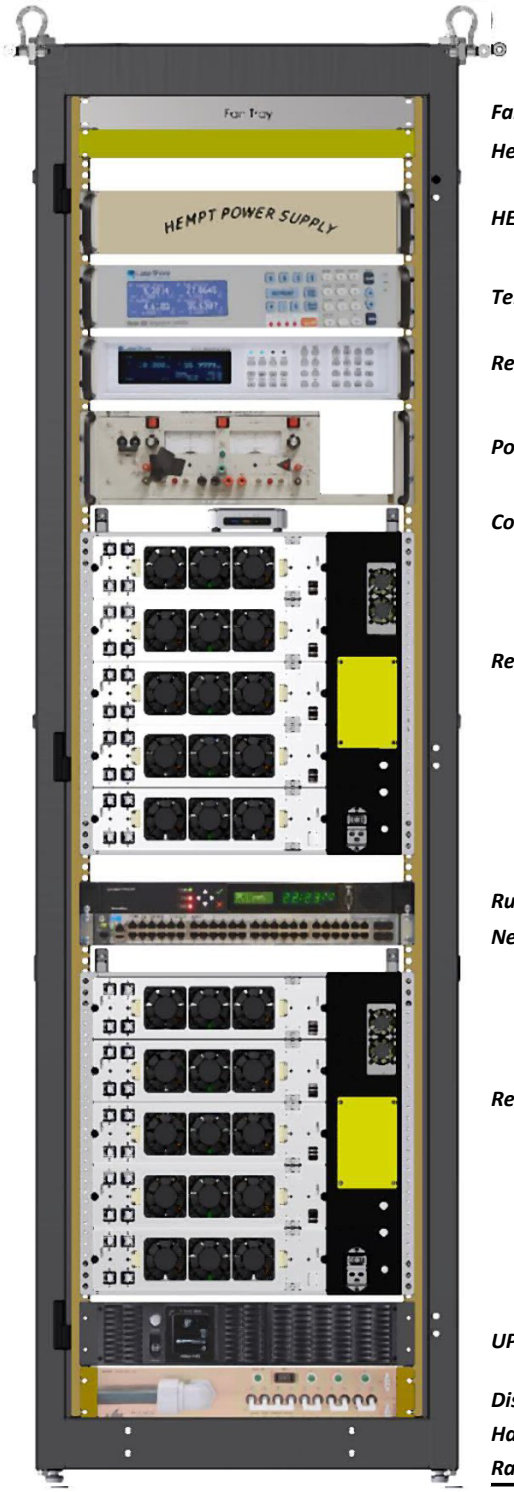

MEC Instrument Rack Components

(3-13-17)

Fan Tray [Kooltronic KT3X502]	21 lb	120 W
Heat Exchanger Assy [723SN00A02]	22 lb	NA
HEMT Power Supply	≈15 lb	0 W
Temp Controller [Lakeshore 350]	17 lb	240 W
Resistance Bridge [Lakeshore 370]	13 lb	55 W
Power Supply [Kepco BOP 20-10ML]	51 lb	200 W
Computer [Intel NUC6i3SYK]	3 lb	65 W
Readout Crate	≈150 lb	1,350 W
Rubidium Clock [Spectracom]	7 lb	50 W
Network Switch [HP2920-48G]	12 lb	70 W
Readout Crate	≈150 lb	1,350 W
UPS [Cyberpower PR3000LCDRTXL2U]	72 lb	NA
Distribution Box [Eaton PC975-LT]	29 lb	NA
Hardware for Craning	39 lb	NA
Rack [Hammond – Custom]	280 lb	NA
Total	**≈881 lb**	**≈3,500 W max**

Figure 2.7 CAD drawing of MEC electronics rack (E-rack) and list of components.

Each ROACH-2 board boots up with an operating system and file system stored in Flash memory and runs a TCP BORPH server (provided by CASPER) to decipher commands. The firmware for the ADC/DAC board is initially loaded by a USB to JTAG interface and is stored on flash memory. The next time the board is booted it loads the firmware from memory automatically.

The ROACH-2 boards are on a private local-area network (LAN) as moderated by the network switch. We run all readout control software on the MEC data server, however, any computer (with the required Python libraries) that is connected to the LAN can perform this task. We use a PPS (pulse per second) signal generator to sync the clocks for each set of readout boards. The PPS signal is synchronized to an external PTP/NTP server to ensure accurate absolute timing as well as synchronization with the data server clock (See Figure 2.8).

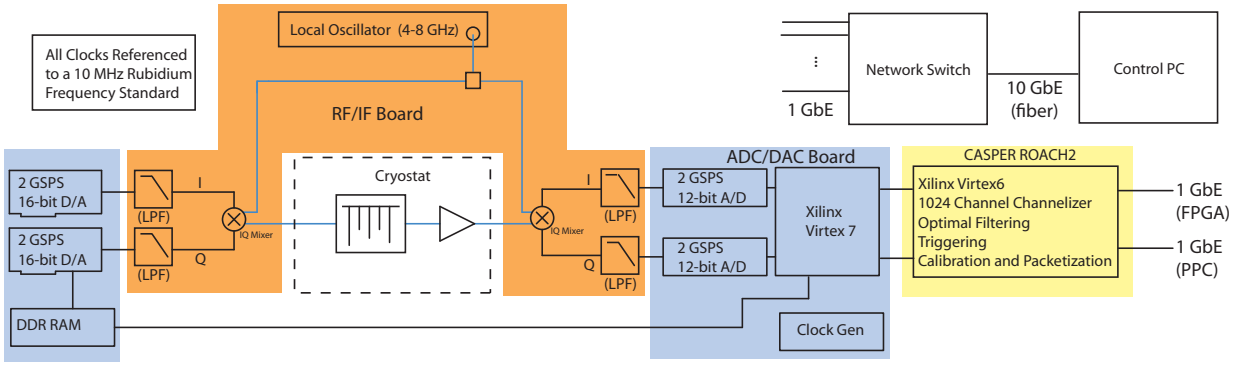

Figure 2.8 System block diagram showing a single 2 GHz, 1024 channel readout unit. Reproduced with permission from Publ. Astron. Soc. Pac 130, 988 (2018). Copyright 2018 The Astronomical Society of the Pacific.

2.4.3 Readout Procedure

The initial setup defines the frequency comb that probes the resonators. This is determined by doing frequency sweeps of every feedline at a grid of powers and then using a machine learning code to both find the resonators and determine their optimal probe powers. Our python software then computes a lookup table (LUT) containing the time-domain sum of the optimum resonator probe tones. The lookup table is stored in DDR3 RAM onboard the ADC/DAC board, and is played to the DAC in a loop while the system runs. The DAC output is passed through the RF/IF board where an IQ mixer upconverts the signal to the right frequency range (4 to 6 GHz or 6 to 8 GHz) using a local oscillator. After traveling through the cryostat, MKID array, and HEMTs, the RF/IF board mixes down the returning signal to baseband where it is digitized by the ADCs. Then the Virtex7 on the ADC/DAC board streams the raw ADC output to the ROACH-2 over the Z-DOK connectors. The ROACH-2 firmware processes ADC data stream, performing the following actions:

1. Separate the comb of frequencies into individual pixel frequencies using an FFT (Fast Fourier Transform) and digital down conversion (DDC).
2. Sample the phase of each resonator's signal every microsecond.
3. Run a pixel-wise unique optimal filter over each pixel's phase signal.
4. Trigger on photon events and store photon packets in buffer.
5. Send buffer to disk every 0.5 millisecond (or faster if full) over 1-Gbit Ethernet via UDP.

Each single photon packet is a 64 bit word with the following breakdown: 10 bit x-coordinate, 10 bit y-coordinate, 9 bit timestamp, 18 bit wavelength, 17 bit baseline phase. A C program on the data server receives the UDP frames containing photon packets sent from the ROACH-2 boards and writes them to disk as observation files. Additionally, it histograms the photons into images for real time display.

2.4.4 Assembling the MEC Readout

The twenty readout units are divided across two readout crates which supply power, 1 PPS, and 10 MHz signals. Each readout crate consists of five cartridges each holding two readout units, one on either side of the cartridge blade. Each cartridge has three cooling fans for its readout units. I assembled all ten of these cartridges in preparation for MEC's 2018 shipment to Subaru Observatory. This project consisted of mounting the readout units to the blades of the cartridge with standoffs, and connecting the readout units to the ethernet, 10 MHz signal, 1 PPS, and power supply with wires and coaxial cables. Several of the cables were a custom design that I made in-house.

I wired around 20 separate connections, some of which stretched across the entire cartridge as seen in Fig. 2.9. These connections must remain in place considering that the cartridges need to be able to be taken in and out of the slots in the readout crate during the testing process. The openings of the readout crates are flush with the upper rim of the cartridge baseplates (the ones holding the cooling fans in Fig. 2.9). I had to find a balance between making the wiring robust, and preserving easy access to the

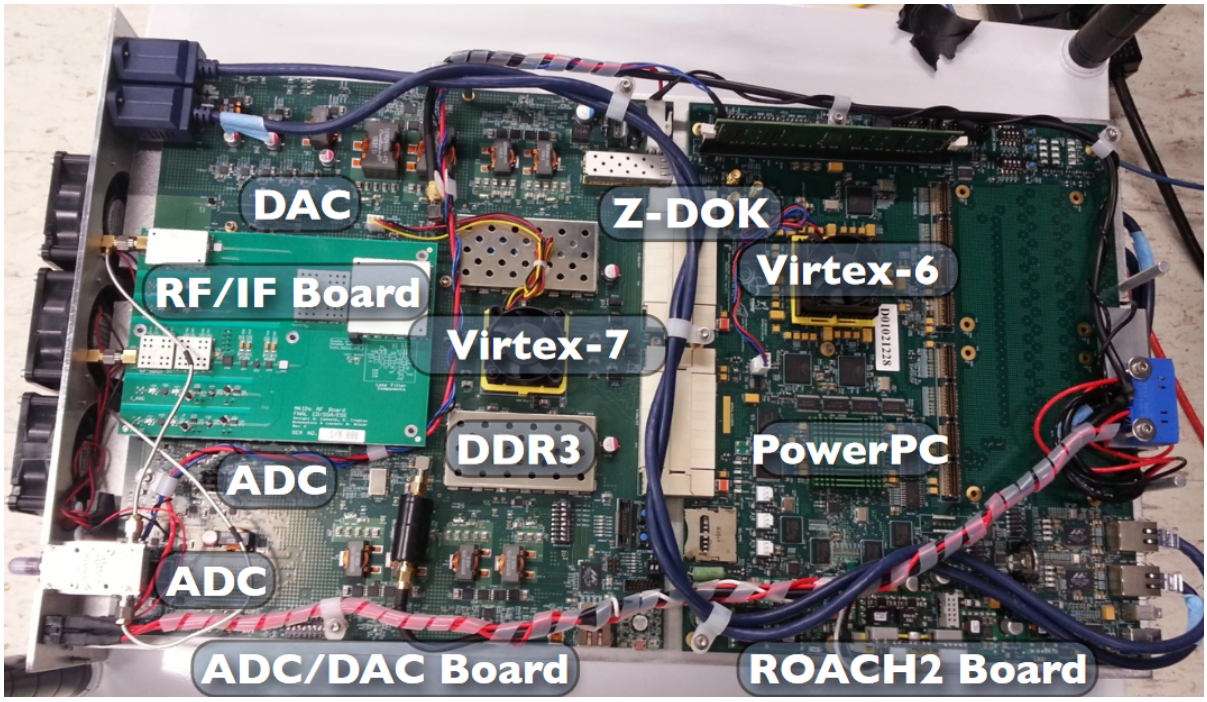

Figure 2.9 Cartridge containing an assembled readout unit. The ROACH-2 board is connected to the ADC/DAC board by two Z-DOK connectors. The RF/IF board is mounted on the ADC/DAC board using SMP blind-mate connectors for signals and GPIO pins for programming. Another readout unit is mounted to the underside of this cartridge. Figure and Caption reproduced with permission from Paschal Strader, "Digital Readout for Microwave Kinetic Inductance Detectors and Applications in High Time Resolution Astronomy", Ph.D. dissertation (University of California at Santa Barbara, 2016).

boards. Thicker wires are more durable and provide more surface area for soldering contacts, but these are bulkier and more likely to snag on some of the delicate electronics on the individual readout boards. I used thin 24 AWG wires as much as possible, and I installed additional standoffs on the readout boards to lock down the bulky ethernet cables and thicker wires snaking across the readout units.

One of the the 10 MHz connections required a custom wiring: one end needed to be a female coaxial cable and the other end needed to splinter into two male pin connectors.

To make this connection, I split a standard male-female coaxial cable in half, saving the female end. I stripped the wire coating to reveal the inner conductor surrounded by a concentric conducting shield. I braided the concentric wire into a single wire strand and used heat shrink rubber to electrically isolate the inner conductor from the braid that used to be the concentric wire. I then soldered these two wire strands into two separate male pin connections to connect the 10 MHz to the power supply.

The next part of the project involved preparing the readout electronics to work with MEC. Each cartridge needed to successfully power on and demonstrate that it could carry out the entire readout process described in Section 2.4.3. I booted up each ROACH-2 board, updating each one with its own IP address, and loaded the firmware onto the ADC/DAC boards. One of the Z-Dok pins allows the ADC/DAC firmware to communicates with the ROACH-2 firmware with SPI (Serial Peripheral Interface). The ADC/DAC firmware employs a Xilinx MicroBlaze soft microprocessor core to run a C program which accepts and executes commands from the ROACH-2. Both of these needed to work in order for the boards to communicate with one another. Throughout the testing process, I would find electronic failures including but not limited to: a blown MOSFET on a ROACH-2, an unbootable ROACH-2, and a ROACH-2 and ADC/DAC pair that wouldn't communicate. When I found one of these failures, I would remove the cartridge in question (hence the engineering constraint for a smooth cartridge removal despite the many wired connections) and replace the offending electronic. I sent ROACH-2s and ADC/DACs back to the CASPER or Fermilab groups for repairs during this time. By

the time MEC was ready to ship, we had a full set of working readout cartridges and a few emergency replacements to go along. Figure 2.10 denotes some additional engineering challenges I faced in the process of getting MEC ready for shipment.

Figure 2.10 Snapshots of some of the notable engineering challenges I faced in getting MEC ready to ship (all pictures taken by I. Lipartito). Top left: a quick picture I took holding my camera up to the microscope as I removed faulty R2 resistors (upon orders from Fermilab) from our RF/IF boards and replaced them with copper wire connections. Top right: MEC E-rack during the cartridge testing process. I used masking tape stickers to make notes of the status of each cartridge and remember which have faulty electronics. Bottom left: A valve got mangled while MEC was being crated for shipping in Spring 2018. Bottom right: I had UCSB Machine Shop repair that valve within a few days. I am leak checking it in this image before shipping it off to join the rest of MEC.

Chapter 3

MEC: On-Sky Performance and Data Processing

In this chapter we discuss the format of data returned by the MKID Exoplanet Camera, along with our data reduction pipeline to process this data. We also discuss MEC's capabilities and current contrast limits, presenting a few systems directly imaged by MEC. We conclude with the performance of the combined MEC and SCExAO system for high contrast imaging of exoplanets and disks, and document the significant new technology developed for MEC. The work was published in Walter et al. (2020) and presented in part by I. Lipartito at the Extreme Solar Systems Conference in 2019 (Reykjavik, Iceland).

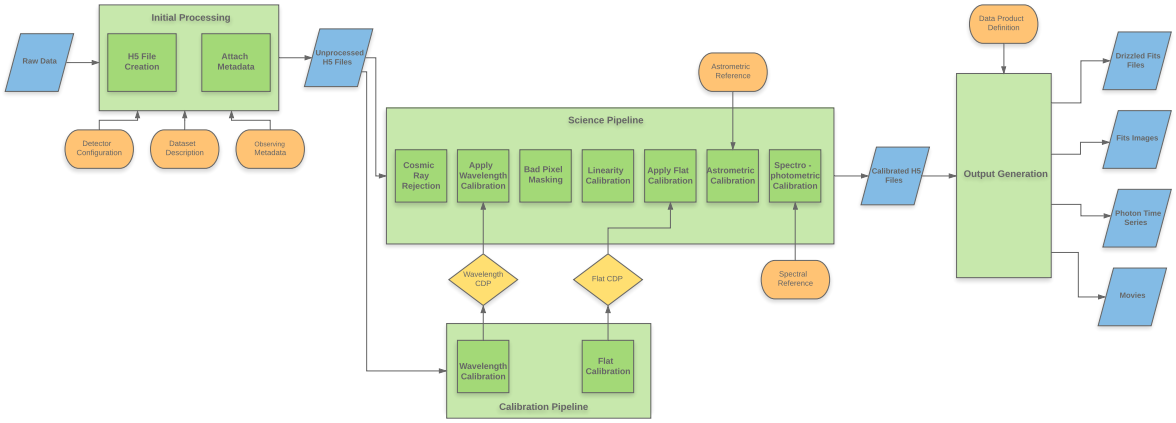

Figure 3.1 Block Diagram of The MKID Pipeline. Calibration steps are shown in green, references and configurations are shown in orange, data products are shown in blue, and calibration data products (CDP) are shown in yellow.

3.1 Data Processing/Calibration

Data calibration is an essential part of observational astrophysics. CCDs (charge-coupled devices) and CMOS (complementary metal oxide semiconductors) are the most common types of cameras used in astronomy and there are well-established methods for calibrating their data products. Like MKIDs, CCD/CMOS detectors suffer from misbehaving pixels and require calibrations to normalize pixel response and register it to some astronomical standard. Due to the unique nature of MKID data, however, we need to develop our own methods of calibrating our data. Our basic astronomical data reduction involves wavelength calibration, flat-fielding, hot pixel masking, and image registration and combination. These methods need to be straightforward to implement and robust to edge cases and outliers.

3.1.1 MKID Data Products

The Mazin Lab develops a data reduction pipeline for each instrument. Our data is taken continuously throughout the night, we only pause data collection when the telescope is moving to a new target. We get one *binary* file for each second of data which contain the photon's arrival timestamp (to the precision of one microsecond), its x and y spatial position, and a number known as the *phase*, the response of the camera to the photon (this will translate to energy). There are four dimensions in which we have information: two spatial dimensions, one time dimension, and one energy dimension. Wrapped in all this information are the speckles, ambient light, and, most importantly, the astrophysical targets.

We can arrange the data into three dimensional cubes or two dimensional arrays depending on the scientific case:

1. Collapsing the data along the time dimension makes a spectral cube, a common output of traditional Integral Field Spectrographs (IFS). MKID cameras are special in that they are simultaneously low-resolution spectrographs and imagers. We can do Spectral Differential Imaging (SDI) on spectral cubes.

2. Collapsing the data along both the temporal and spectral dimension, making an image in a specified band of light. We can do Reference Differential Imaging (RDI) and photometry on these images.

3. Collapsing the data along the spectral dimension makes a temporal cube. We can

look at the timestreams of light in the pixels of this cube and analyze whether they correspond to a Gaussian or Modified Rician probability distribution (Stochastic Speckle Discrimination, SSD). We can also do Angular Differential Imaging (ADI) on the temporal cube.

3.1.2 MKID Pipeline

To analyze MEC data we use The MKID Pipeline available on Github: https://github.com/MazinLab/MKIDPipeline. The MKID Pipeline begins by transforming the raw binary data into calibrated photon lists in a fast access database. This process is outlined in Figure 3.1. Many of the steps were implemented for the ARCONS pipeline (van Eyken et al., 2015) and were copied or slightly modified for MEC.

1. **Processing Binary Data into a HDF5 Database**

   The raw binary observation files, consisting of header and photon data sent over ethernet, are interpreted and saved into a HDF5 (Hierarchical Data Format) table format. The table has one entry for each photon with the following fields: pixel ID, arrival time, phase height (or wavelength), and two additional weight fields to be set in later calibration steps (spectral weight and noise weight). The photon list is rearranged so that it is first ordered by pixel location and then by time.

2. **Cosmic Ray Rejection**

Cosmic rays incident on an MKID detector have the effect of illuminating most of the array with false high energy photon counts. This calibration step removes time chunks from further analysis that are identified as containing a cosmic ray. The advantage of MKID's timing resolution is that these time chunks can be precisely selected to remove an average of only 0.01% of a given observation. This retains as much of the original exposure time as possible.

3. **Wavelength Calibration**

The wavelength calibration is essential to utilize MKID's energy resolving capabilities. Several monochromatic laser exposures are used to determine a quadratic, $a^2\phi + b\phi + c = hc/\lambda$, that converts phase, ϕ, into wavelength, λ for each pixel. To save space, the phase height float column is overwritten with the calibrated wavelength for each photon that has a valid wavelength solution.

4. **Bad Pixel Masking**

Hot pixels are defective pixels registering an abnormally high response to a given amount of light. Another type of defective pixel is a 'dead' pixel, a pixel incorrectly registering zero counts. These badly behaving pixels are prevalent in our data since we try to include as many pixels as possible from the readout step. Dead pixels are straightforward to locate as they register zero counts. Hot pixels are more difficult to pinpoint as they might be as bright as the maximum count rate (2500 CPS) or they might only be marginally brighter

than the surrounding pixels. We need a sensitive algorithm that takes into account the local behavior of pixels to identify which (if any) are behaving unexpectedly.

I started by adapting the ARCONS hot pixel removal algorithm (van Eyken et al., 2015) for MEC data. This algorithm, the *Gaussian Moving-Box Algorithm*, flags any pixel whose flux exceeds a theoretical maximum defined as Nσ above some maximum ratio which is calculated from a theoretical Gaussian PSF. This algorithm is effective, although computationally expensive, as the entire kilopixel array needs to be passed over by a Gaussian moving-box. Moreover, the ARCONS data did not have stable hot pixels, rather, a large number of pixels across the array might flash 'hot' on the order of seconds randomly throughout the observation sequence. This meant the algorithm needed to be applied over many small time bins. The MEC array is an order of magnitude larger than the ARCONS array. Moreover, our high-contrast imaging datasets are up to several hours long, making this calibration step a significant bottleneck in the pipeline.

In my process of speeding up the hot pixel code, I tried less expensive algorithms, for example, a *Median Moving-Box Algorithm* which cuts out any pixel registering a count rate higher than Nσ above the median of a box of pixels around it. I also tried an adaptation of the L.A.Cosmic code (van Dokkum, 2001) designed for catching cosmic rays in CCD data by convolving the images

with a Laplacian kernel to identify the sharp edges of a cosmic ray. Although I was looking to identify a different physical phenomenon, I thought the same mathematics could be applied to identify the sharp edges of a hot pixel.

Both of these algorithms succeeded at detecting lone hot pixels surrounded by faint pixels, but also flagged the core of the stellar PSF. Moreover, these algorithms only caught hot pixels close to the maximum count rate, they failed to find hot pixels that were not quite saturated. Given the yield of the MKID array (see Sec. 3.2.1), we could not afford to lose any well-behaved pixels. And given the scientific demands of high-contrast imaging, we absolutely could not allow hot pixels to slip into our final data products. My tests found the Gaussian Moving-Box was superior since it assumes the shape of the stellar PSF. This algorithm consistently flagged anomalies to the PSF without flagging speckles or the stellar core.

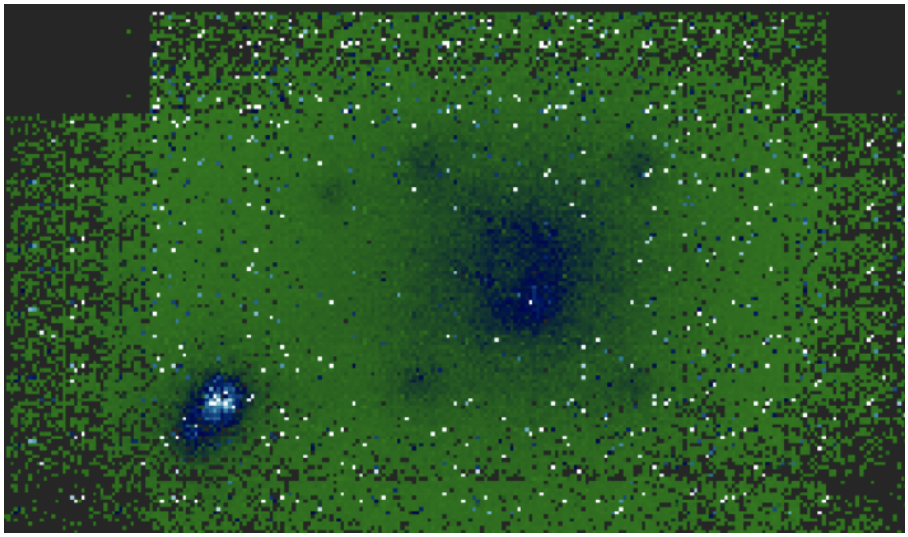

Figure 3.2 Image of the Trapezium Cluster before hot pixel masking.

Extensive testing on MEC data obtained in early 2019 (among other systems, the observations of Kappa And and 51 Eri) revealed that the new generation of Platinum Silicide MKID arrays Szypryt et al. (2017) do not exhibit the 'flashing' hot pixels of the ARCONS arrays. Hot pixels remain consistently hot, meaning that the hot pixel algorithm needs to be applied only once over a single observing position. The solution to the hot pixel algorithm bottleneck was solved through engineering; the MEC Gaussian Moving-Box algorithm is robust and is currently the default hot pixel algorithm used in the pipeline. The default Nσ is 4σ (found empirically through this testing process), although the user can adjust this threshold along with the moving-box size, the background flux count, and the FWHM of the test PSF. The hot-pixel corrected image is presented for the user to inspect while running the pipeline. Maps of dead and hot pixels are saved as metadata and these pixels are removed from the final data product.

5. **Linearity Correction**

This calibration accounts for missing photons due to the detector dead time. This dead time (10 μs for MEC) is introduced in the firmware to avoid photon pile-up and limit the total count rate, but results in a non-linear detector response at high count rates. To account for this effect, a correction factor is applied to the spectral weight column for each photon depending on the local count rate.

6. Flat Field Calibration

The goal of flat-fielding is to normalize each pixel's response to light across the array. The quantum efficiency (QE), or pixel response to light, for the most part remains constant with count rate, but varies slightly from pixel to pixel due to physical differences stemming from optical alignment or from slight fabrication inconsistencies. This calibration is done as a function of wavelength (wavelength spacing corresponding to the energy resolution determined from the wavelength calibration).

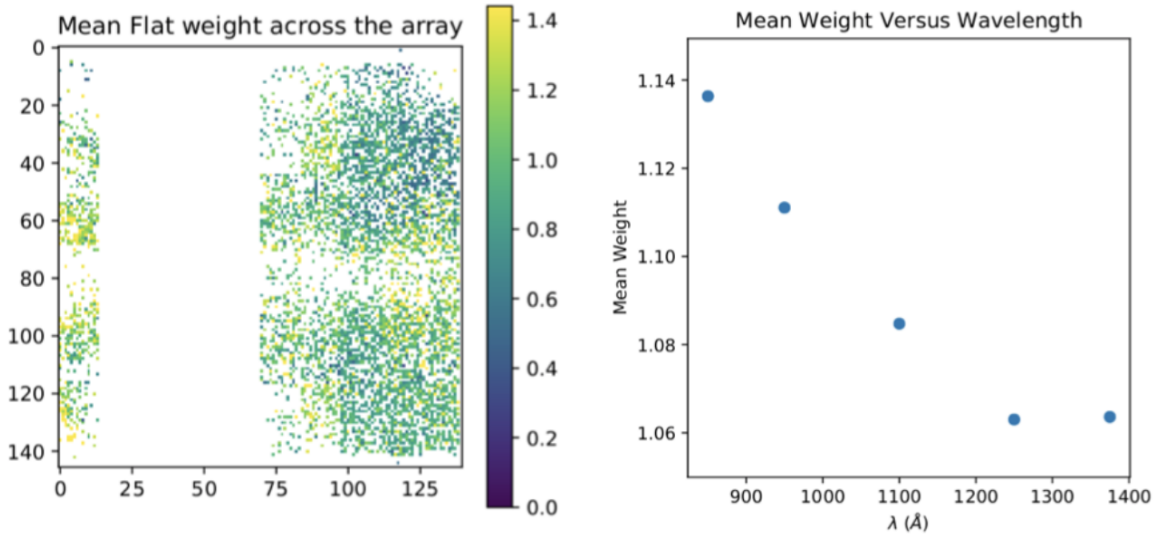

Figure 3.3 Flatcal solution summary plot made using a white light source. Left: Mean flat weight across the array; Right: Mean flat weight versus wavelength. Blank spaces are from failed pixels (see Section 3.2.1)

I adapted the original flat calibration algorithm written for the ARCONS pipeline (van Eyken et al., 2015) for the MEC instrument to be made from

either a white light source or the the monochromatic calibration data used for the wavelength calibration. On-sky time is precious and due to the complex MEC+SCExAO system, it is not always feasible to switch to a white light source in order to get a flat calibration each night (particularly if MEC is observing in conjunction with another Subaru instrument). I realized we could use the monchromatic wavelength data as a low-order approximation of a white light source. The energy resolution of MEC results in about 10 separate wavelength bins for a whitelight source, making the 5-6 monochromatic lasers used in the wavelength calibration a reasonable approximation.

The flat weight per pixel per wavelength slice are found by by dividing each wavelength slice by the mean intensity of that slice. The flat weights are roughly smooth in wavelength (Figure 3.3) and are fit with a low-order polynomial so we can interpolate between wavelength slices (a spline is not used as splines run the risk of smoothing the data and misrepresenting the errors in the data). The resulting flat weight multiplies into the spectral weight column of the HDF5 table to merge with the linearity weight for each photon.

7. **Astrometric Calibration**

This is an implementation of a standard astrometric calibration to relate (x,y) pixel coordinates on the MKID array to sky coordinates using a linear mapping with rotation.

8. **Spectral Calibration**

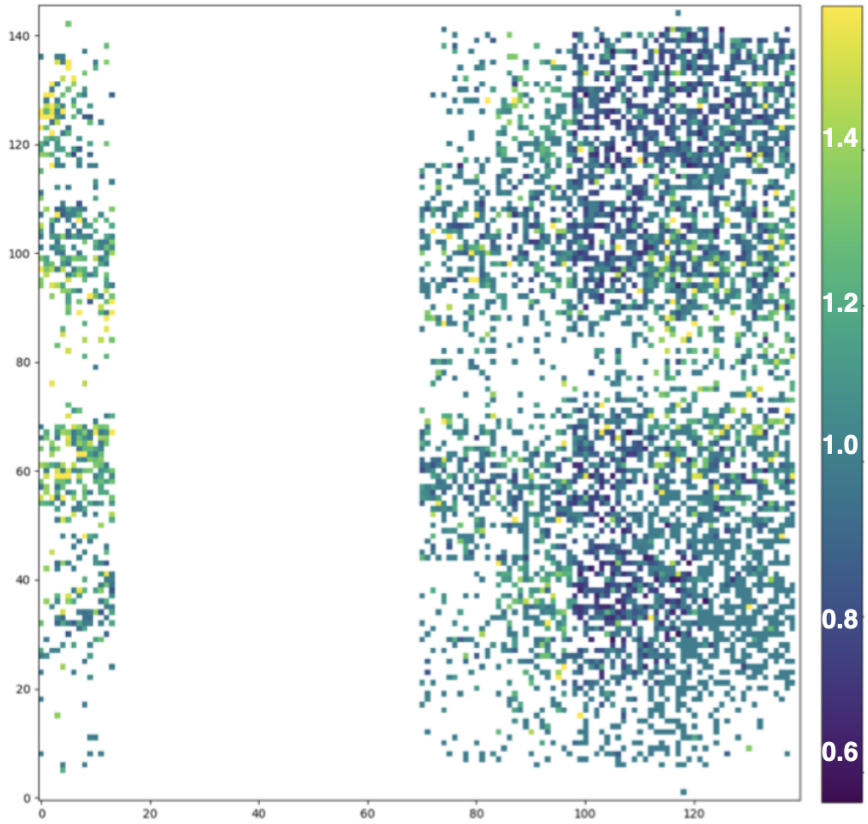

Figure 3.4 The resulting flatfield structure of a Y-band flat-calibrated image of star Kappa And divided by its raw image. Blank spaces are from failed pixels (see Section 3.2.1)

This calibration accounts for the total QE of the detector and system as a function of wavelength. A spectrum is taken of a spectral standard with MEC and is compared to a calibrated spectrum of the same object. The resulting correction multiplies into the spectral weight column of the HDF5 table to merge with the flat weight and linearity weight for each photon.

9. **Output Generation**

There are a variety of output file formats that the MKID Pipeline can generate. In addition to FITS files which are compatible with more standard post-

processing techniques, photon lists can be output directly to perform more specialized techniques that utilize the photon-counting ability of MKIDs.

Image Registration

Not all pixels in an MKID array are usable (see Section 3.2.1 for a discussion of the current MEC array's pixel yield). Pixels are subject to failure due to fabrication imperfections and electronic issues. If we held a target on a single part of the array for the entire exposure, it would appear 'patchy' due to the unresponsive pixels it is inevitably going to rest on. To counteract this, we 'dither' the target around on the array using a mirror mounted on a CONEX-AG-M100D piezo stage (this is build into the instrument's optical system, see Section 2.2). The target's position on sky does not change, rather it optically lands on a different part of the array with each dither. We typically set up a grid of 5 by 5 dither positions (25 total), each position held for about 30 seconds. This maximizes the chance that the target gets filled in by functioning pixels. This meant that we needed a calibration to map the CONEX mirror optical offsets to the actual physical position of the target on the array. I made this calibration using an unocculted dither on star 51 Eri taken on 1/12/2019 (x_{CONEX} and y_{CONEX} are saved in a file automatically for each dither). I used the photutils package from Astropy[1] (Astropy Collaboration et al., 2013, 2018) to fit a centroid to the star's PSF for each dither position, obtaining x_{pixel} and y_{pixel}. This process is shown in Figure 3.5. I fit a 2D geometric transform using scikit-image[2]

[1] http://www.astropy.org
[2] https://scikit-image.org

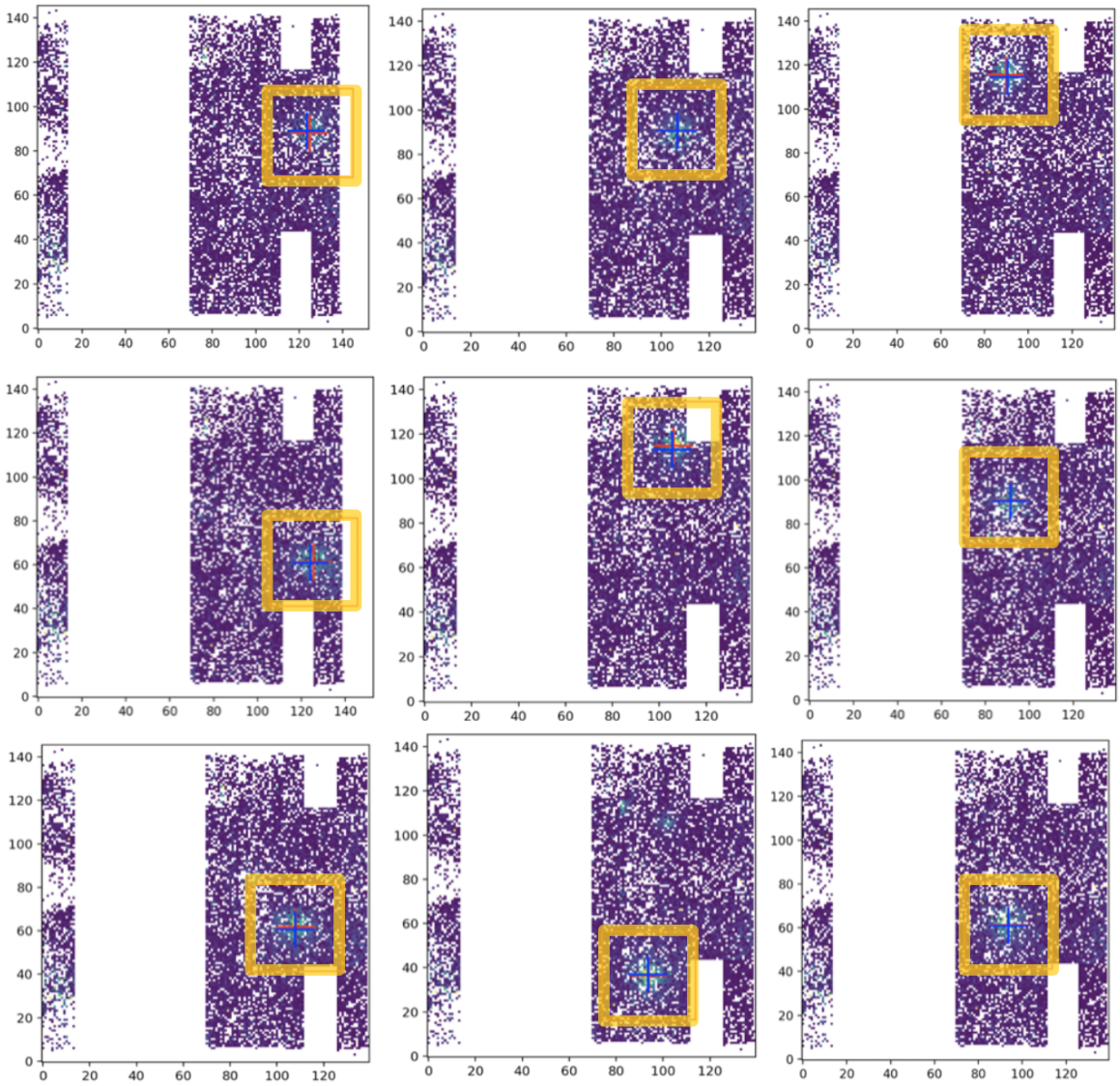

Figure 3.5 Tracking the 51 Eri PSF across a dither taken on 1/12/2019. From this dither, I obtained a CONEX-to-pixel mapping that could be applied to register all future dithers. This set of images also showcases our array yield circa 2019-2020 and hence the need for dithering.

(van der Walt et al., 2014) to obtain a functional form the CONEX-to-pixel mapping, which can be applied to return the pixel positions of all future dithers. Knowing the pixel positions of the target in each dither enables us to align and stack images.

3.1.3 Analysis of Calibrated Data

After the photon lists have been calibrated we can begin the analysis of astrophysical data produced by MEC. The easiest to understand procedure is to bin the photon list in time and wavelength to create images after which classical astronomy post-processing techniques can be used.

Figure 3.6 shows the five star system Theta[1] Orionis B taken in y-band by MEC at Subaru Telescope on Jan. 12, 2019. B1, behind the coronagraph, is a spectroscopic eclipsing binary with nominal magnitude of V=7.96. B2 and B3 are resolved by Subaru Telescope's 8.2 m mirror in conjunction with the AO correction provided by SCExAO (Jovanovic et al., 2015). The four astrogrid speckles artificially created by the DM are present in a square centered about B1, behind the coronagraph. These speckles are about 5.5 magnitudes fainter than B1. B4 is 4.98 magnitudes fainter than B1 in H-band (Close et al., 2013). It is important to note that this observation was taken before the re-coating of the secondary mirror at Subaru which occurred on November 7th, 2019. The throughput hit taken before the mirror re-coating, coupled with the already dim guide star, B1, leads to a worse AO correction than is possible either now on the same system, or on a similar system with a brighter guide star.

The image uses data from 25 different 30 s observations located at different positions on-sky collected in a dither. These individual observations underwent wavelength calibration, flat-fielding using the monochromatic laser data taken for the wavelength calibration, and hot/dead pixel masking. We use a drizzling code to place the list of

observed photons in a virtual pixel grid that correctly takes into account the translation from the dither position as well as sky rotation as observed from the Nasmyth port. This helps to account for the lack of full array coverage due to dead feedlines and pixels to generate a complete image.

This was our first star system image from MEC and it provided an example of MEC's contrast: B4, a star about 5 magnitudes fainter than B1, is clearly visible. It also demonstrated MEC's resolution: B2 and B3, separated by about 0.12" per Close et al. (2013), are discernible as separate stars in our image. This image also served as a testament to the ability of our data reduction pipeline to flat-field, remove misbehaving pixels from, and wavelength-calibrate our data to make a clean Y-Band image.

It is also possible to use the data directly without any binning in the calibrated photon list for more complex analysis, like the stochastic speckle discrimination technique outlined in Walter et al. (2019).

3.2 MEC On-Sky Performance

MEC underwent a major upgrade in late 2019 where we replaced internal microwave wiring that was degrading resonator performance due to crosstalk and excess noise (Smith et al., 2020). The results below reflect the performance after the upgrade, with the exception of the contrast which was measured with data from the January 2019 run. Due to fabrication problems we have also not yet been able to improve on the engineering grade MKID array in MEC, although we hope to install a science grade MKID array

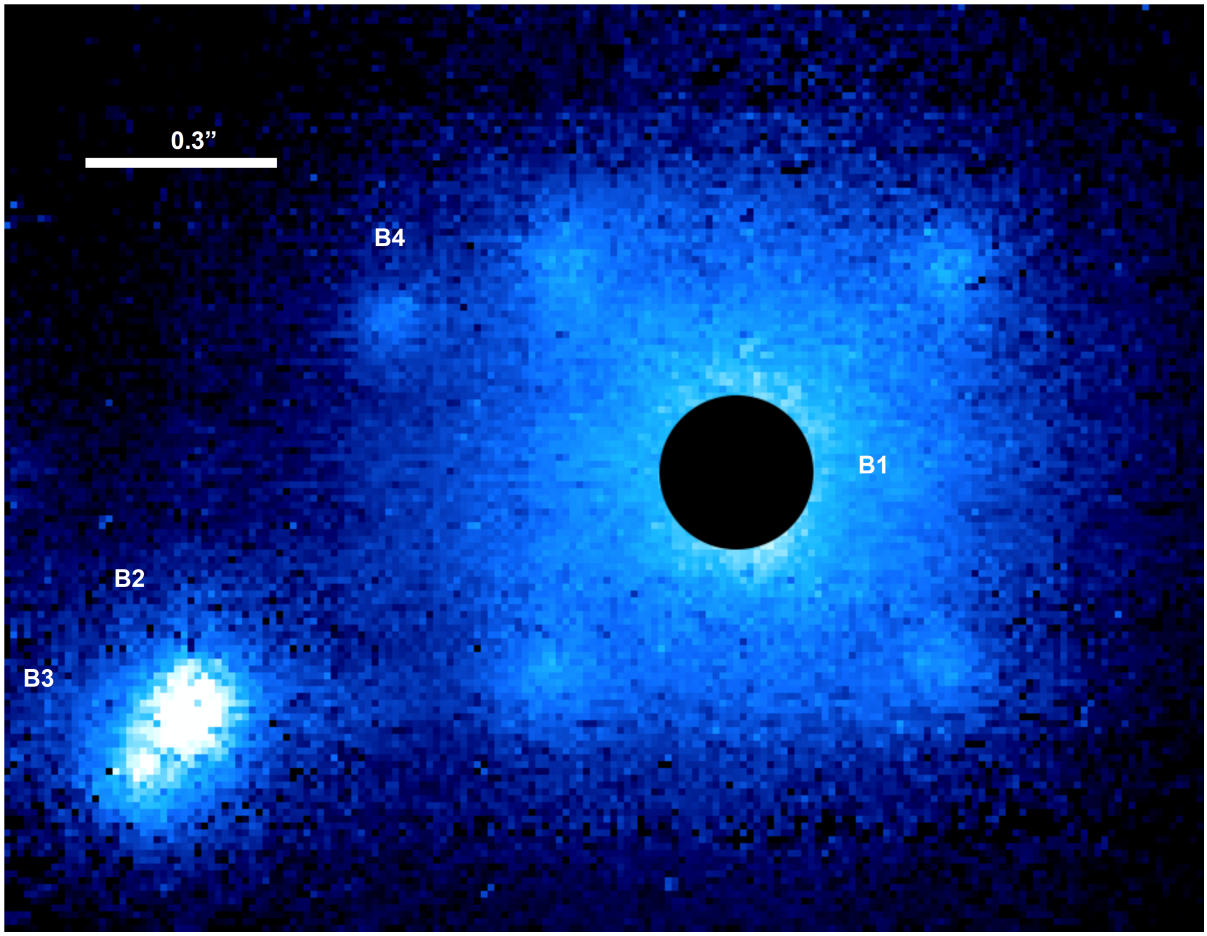

Figure 3.6 Y-Band image of Theta[1] Orionis B taken by MEC at the Subaru Telescope on Jan. 12, 2019. A dither sequence of 25 30 s images are stacked and then smoothed by a Gaussian filter. These individual observations underwent wavelength calibration, flat-fielding using the monochromatic laser data taken for the wavelength calibration, and hot/dead pixel masking. The black circle indicates the location of the coronagraph on B1. The four astrogrid speckles artificially created by the DM are present in a square centered about, and about 5.5 magnitudes fainter than, B1. B4 is 4.98 magnitudes fainter in H band than B1. The four artificial speckles are for astrometric and photometric calibration.

with all feedlines functional and higher yield in 2021. Luckily, most of the exoplanets of interest fit within the smaller field of view of the engineering grade array, although the full array will feature a 1.4” x 1.5” field of view to improve observations of disks.

3.2.1 Yield

Yield, or the number of functioning pixels compared to the total number of possible pixels, can be complex in an MKID array as every pixel is unique and can be compromised in a number of ways. For example, a speck of dust landing on a pixel during fabrication can short out a resonator, or merely move it to an unpredictable frequency. Non-uniformities in film thickness or composition can move resonators around in frequency, causing frequency overlaps that can render at least one of the pixels unable to be read out. Even worse, fabrication problems such as shorts due to photoresist bubbles can knock out entire feedlines, as seen in feedlines 2–4 in the MEC engineering array.

The engineering MEC array pixel map is shown in Figure 3.7. For the fully working feedlines (6-10), 75% of pixels are photosensitive with 61.4% having a good wavelength calibration solution. When only looking at the best part of the detector (the "sweet spot"), between 20 and 60 in the y direction, these numbers increase to 82.1% and 74.3%, respectively. The bad section in the center, between 60 and 80 in the y direction, is likely performing poorly as the device surface impedance was slightly higher than desired, so these resonators are lower frequency than designed (starting at 3.5 vs 3.9 GHz), causing some issues with resonator coupling to the feedline and HEMT gain.

Simulations with the MEDIS package (Dodkins et al., 2020) have been performed to estimate the impact of dead pixels on the raw contrast (before post processing with ADI/SDI/SSD/etc.) for exoplanet direct imaging. These simulations show that the raw contrast will be roughly two times worse with observed yield in the sweet spot compared

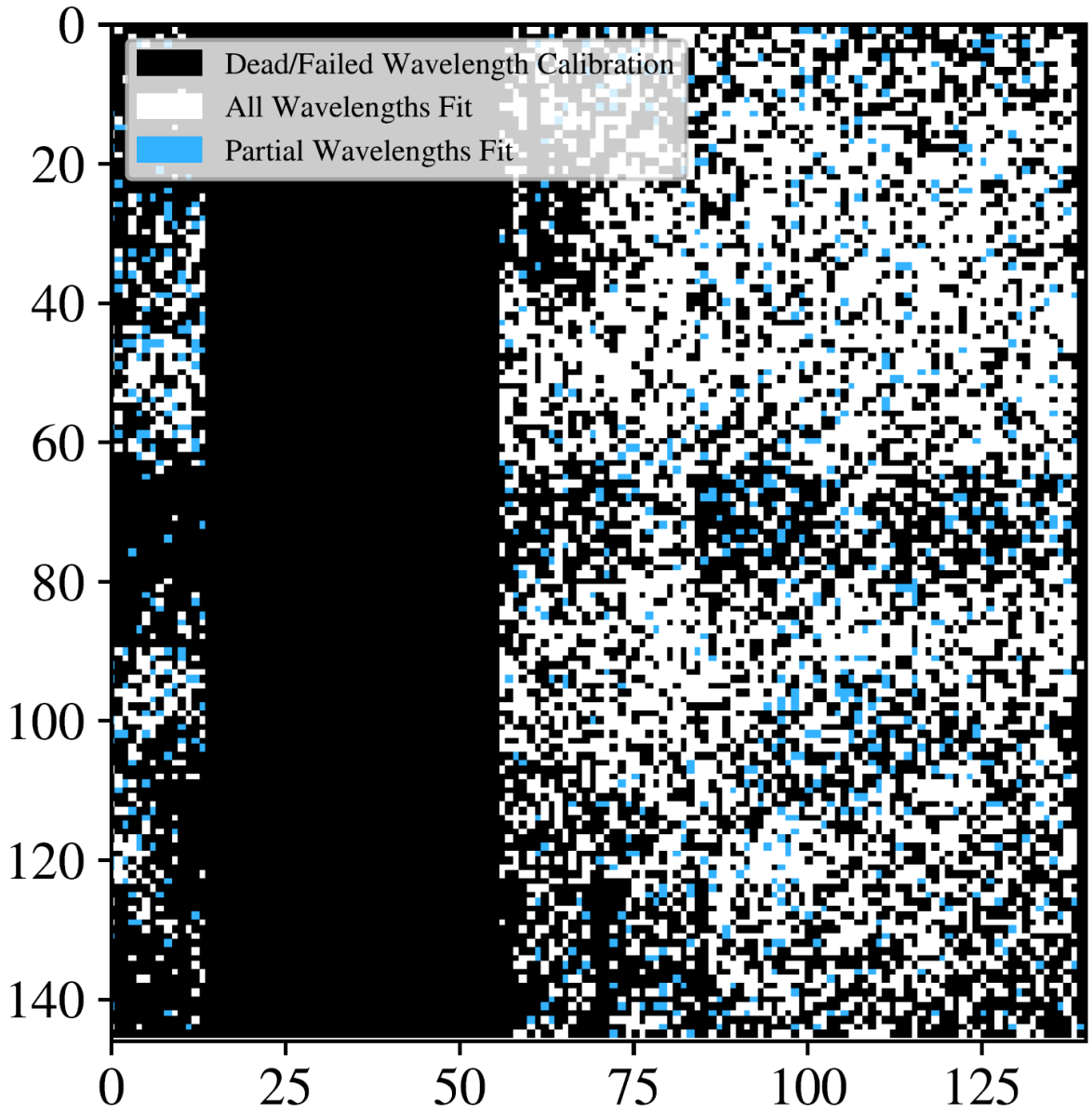

Figure 3.7 Wavelength calibration results for the engineering array in MEC. Fully wavelength calibrated pixels are shown in white, pixels calibrated using a subset of the available wavelengths are shown in blue, and pixels that had no wavelength calibration solution are shown in black.

with perfect yield, as shown in Figure 3.8.

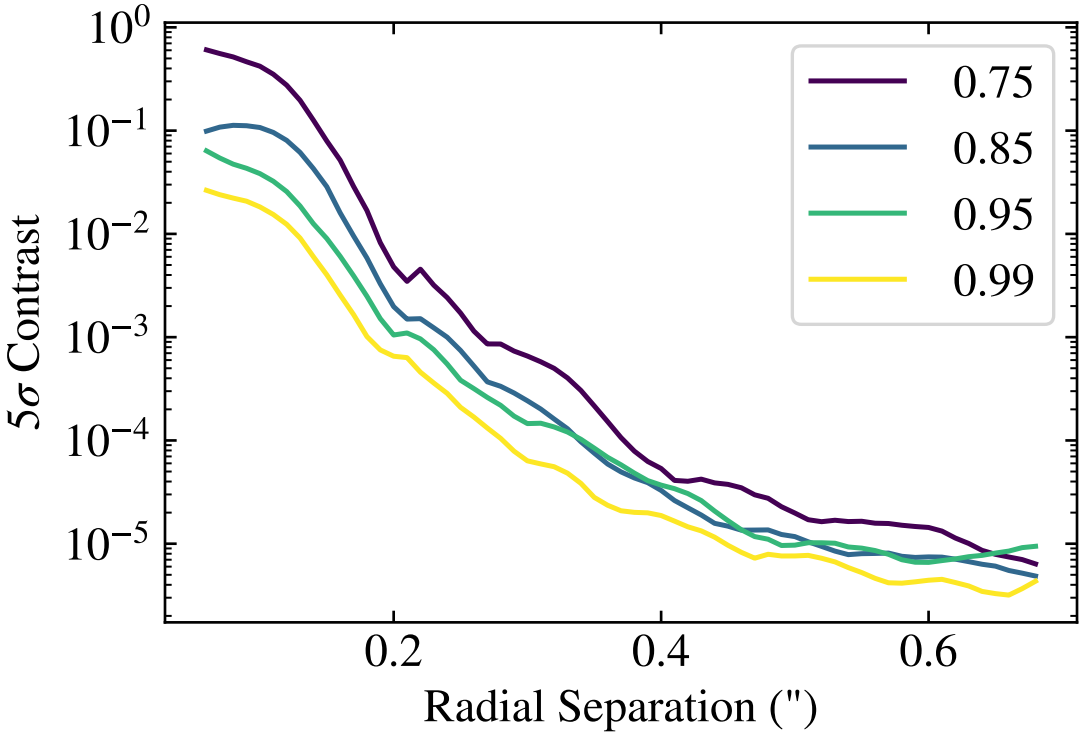

Figure 3.8 Simulation with the MEDIS package performed to evaluate the impact of dead pixels on the raw contrast of MEC. The four different lines represent the effect of varying pixel yield on the 5σ contrast.

3.2.2 Spectral Resolution

The spectral resolution of an MKID is a complex tradeoff between material, pixel geometry, and readout technique. The spectral resolution of the MKIDs used in MEC are explored in great detail in Zobrist et al. (2019). However, this data was taken under ideal circumstances in a dilution refrigerator in our lab, not in an ADR at the top of a mountain on an electrically noisy Naysmth platform. Figure 3.9 shows the actual measured spectral resolution histograms of all the pixels in MEC, while Figure 3.10 shows a map of spectral resolution at a single wavelength.

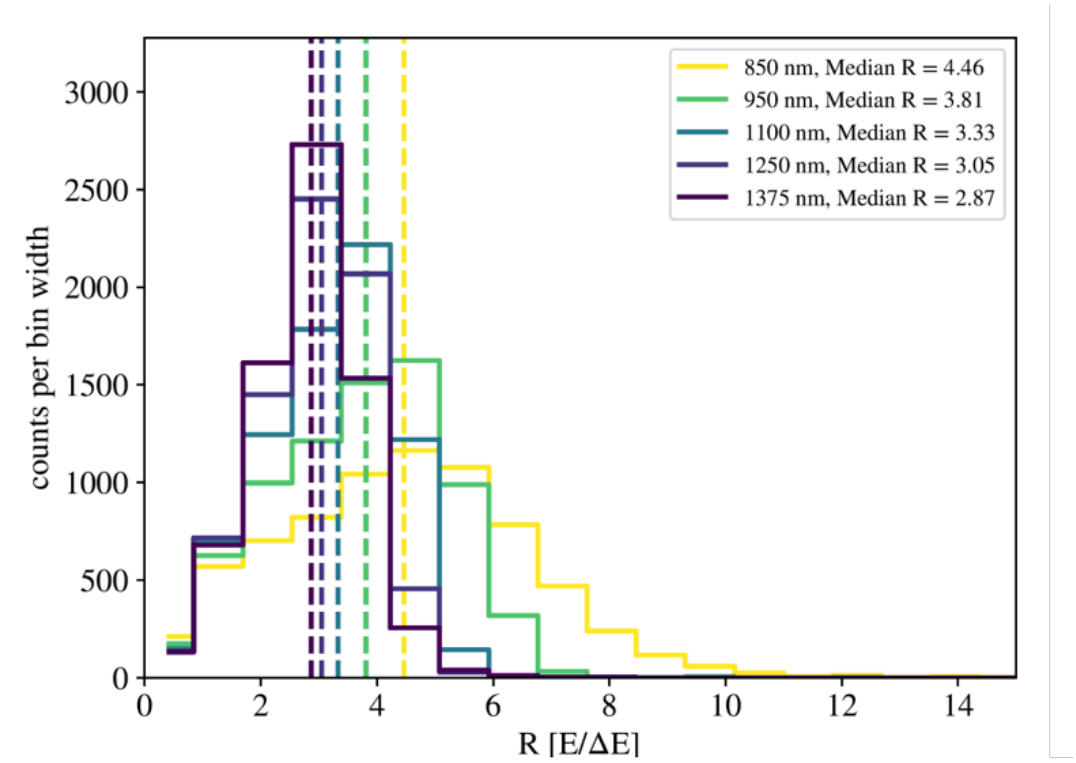

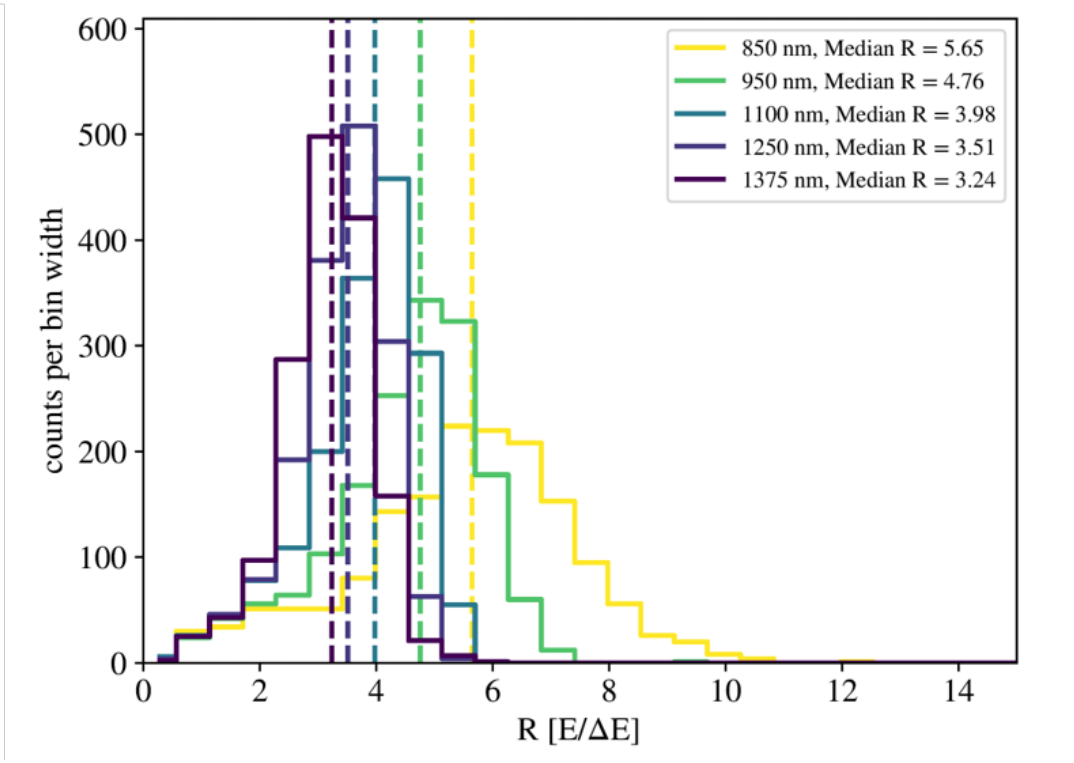

Figure 3.9 MEC spectral resolution for the whole array (top) and in the sweet spot (bottom). Note the differing vertical axes scales due to the smaller number of probed pixels in the best part of the array.

A hand selected MKID pixel on a MEC-style PtSi array measured with a HEMT in the lab has a spectral resolution of around R=7.5 at 980 nm, while in MEC the median pixel in the good region of the array has R=5 at 980 nm. This degradation is likely related to several factors, including:

- Excess noise in the readout caused primarily by loss of signal in the high density microwave cables (Smith et al., 2020) that bring the signals to the HEMT.
- Intermodulation products causing unwanted tones that interfere with the pulse readout.
- Many pixels are not ideal due to fabrication errors, such as frequency overlaps.

The readout itself does not appear to introduce noticeable degradation aside from the intermodulation products, which can be reduced through an optimization algorithm (Fruitwala et al., 2020).

3.2.3 Throughput

Throughput was calculated by comparing a spectrum of the G0 type star BD +172803 attained by MEC with a calibrated spectrum of the same target. This calibrated spectrum was generated by taking a G0 type stellar spectrum from the PHOENIX library and normalizing it to match the reported J and H band flux for this object (Husser et al., 2013; Cutri et al., 2003). In order to compare the two spectra, both were binned in 0.05 eV bins which over samples the median MKID energy resolution by a factor of $\sim$4.

Dividing this binned MEC spectrum by the binned calibrated spectrum should yield

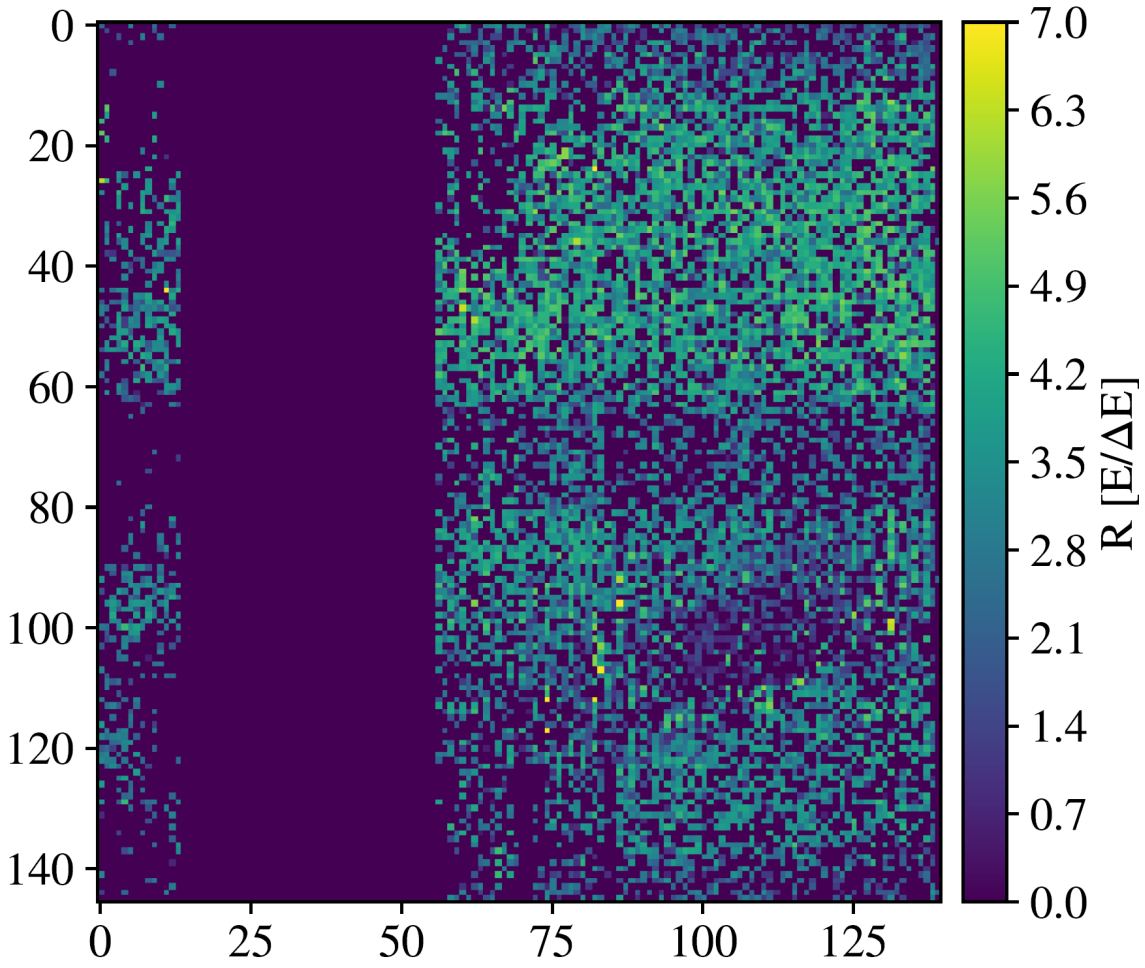

Figure 3.10 Map of energy resolution for MEC's engineering array at 1.1 μm

the total system throughput as a function of wavelength, but there are some additional factors that must first be taken into consideration. During this observation, a 90/10 beamsplitter upstream of the MEC optics in SCExAO was used which directed only 10% of the total available light to MEC. A dichroic was in place which reflected all light shorter than 950 nm, so we didn't expect flux at wavelengths below that for this observation. Additionally, since this target has a J band magnitude of 6.6 and an H band magnitude of 6.4, MEC's 2.5 OD filter had to be used so as to not saturate the array. This filter

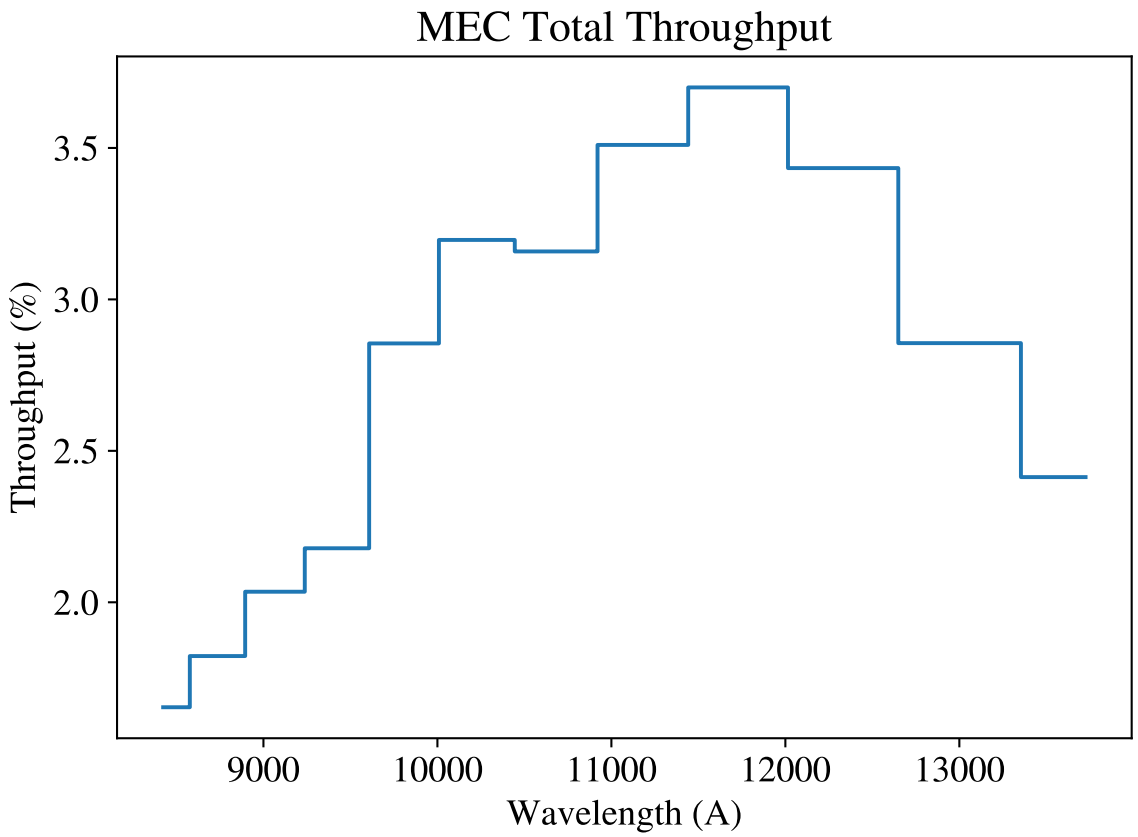

Figure 3.11 MEC throughput, from the top of the atmosphere to registered photons in the MKID detector, as a function of wavelength

has not been measured as a function of wavelength for MEC and so represents a source of uncertainty in this calculation. Finally, the measured Strehl during this observation was found using the C-RED 2 IR camera in SCExAO to be 78% in H band which must also be accounted for since a tight aperture was used so as to only encompass the core of the PSF. Since the Strehl is expected to be worse at shorter wavelengths, using this measured H band Strehl of 78% represents a lower limit on the J band throughput.

Taking all of these factors into consideration, the resulting average J band throughput of the total optical system is 3.3±0.1%, see Figure 3.11. This is roughly consistent

with what we expect if the total throughput of the atmosphere, telescope, AO188, and SCExAO are roughly 20%. It is possible slight misalignment of the microlens is reducing detector quantum efficiency, so careful measurements of the science grade array QE will be performed before installation to allow modelling of the full system thoughput to compare with on-sky measurements.

3.2.4 Contrast

Different ratio performance metrics are sometimes interchangeably referred to as *contrast*. In this section, I will be using the concept of contrast as defined in Martinez et al. (2013):

> The contrast refers to the ratio of intensity in the raw coronagraphic image, averaged azimuthally at a given angular separation, to the peak intensity of the direct flux.

Contrast is distinct from detectability, which is also defined by Martinez et al. (2013):

> When studying a differential image, implying the subtraction of a reference image, the average contrast is no longer suited. The detectability is used then, which stands for the azimuthal standard deviation measured in a ring of width λ/D

I used our January 2019 observations of 51 Eri to determine MEC's on-sky contrast, as that was one of the few targets for which we had an unocculted (coronagraph out) and occulted (coronagraph in) dither. 51 Eri is a high-proper motion (V Mag = 5.22) star with

a young Jovian planetary companion (51 Eri b Macintosh et al., 2015b). We suspected at this stage in MEC's career, we weren't going to detect the planetary companion ($\sim$ 14.5 magnitude contrast between planet and star), but the host star itself would be useful for the calculation of MEC's contrast limit.

I wavelength-calibrated, flat-fielded, and bad pixel-masked our 51 Eri observations, aligning the individual positions of each Y-Band dither and median-combining them for optimal array coverage (I also normalized them by exposure time). I used photutils to fit a PSF to the unocculted image of 51 Eri in order to obtain a value for the unocculted PSF flux. The FWHM of the central star is $\sim$2.5 pixels (λ/D for Y-Band using the Subaru Telescope's 8.2 m mirror). In order to generate the PSF profiles for both the unocculted and coronagraphic images, I generated a series of annuli of non-overlapping apertures at each λ/D. An example of these for a few annuli is shown in Figure 3.12 for Kappa And. Again using photutils aperture photometry, I calculated the flux of each aperture, taking the azimuthal average for each annulus (masking out the annuli that contained the satellite speckles). The mean flux in each annulus divided by the unocculted PSF flux is the contrast. The standard deviation of the flux in each aperture is the detectability.

Figure 3.13 depicts the raw Y-Band contrast as measured with 51 Eri. The top left image is a Y-band image of the unocculted PSF, processed through the MKIDPipeline as described in Section 3.1.2. The bottom left image is a Y-band image of the occulted PSF also processed through the MKIDPipeline. The graph on the right depicts different performance metrics. The blue curve is the unocculted contrast curve and the orange

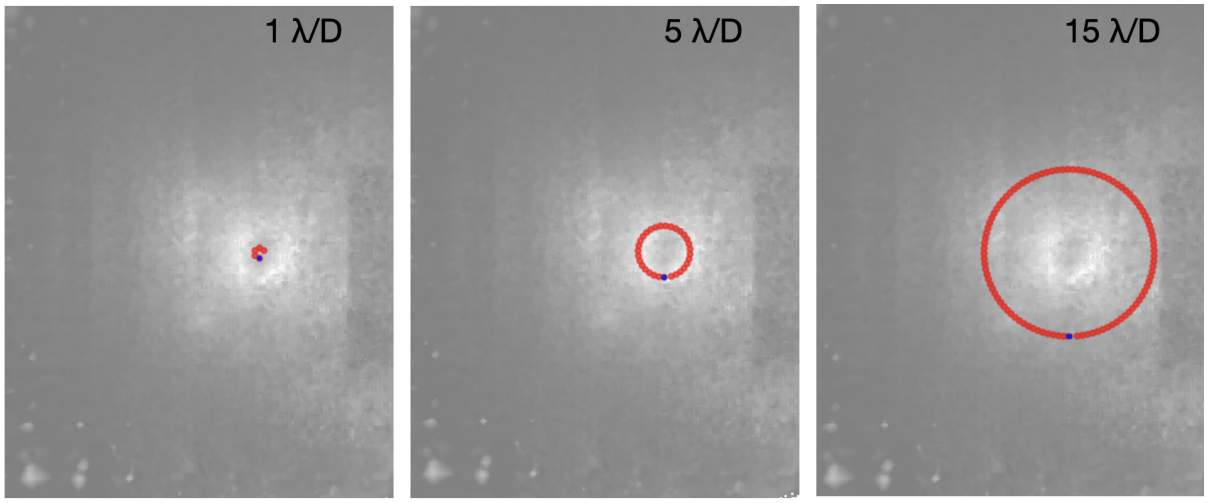

Figure 3.12 A sample of annuli for the coronagraphic Y-Band Kappa And image. Left to right: 1 λ/D, 5 λ/D, and 15 λ/D. Some of the annuli have little gaps because there was not enough space in the annulus to squeeze in another aperture that wouldn't overlap with the other apertures.

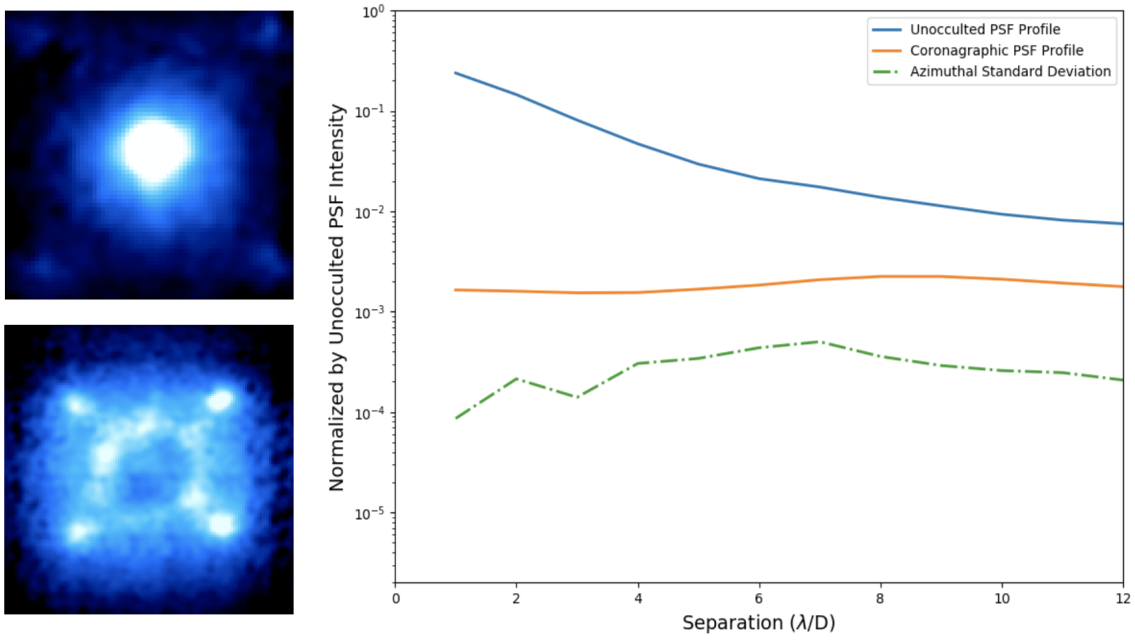

Figure 3.13 Raw Y-Band contrast as measured with 51 Eri. Top Left: Unocculted PSF; Bottom Left: Coronagraphic PSF; Right: Contrast curves for unocculted (blue) and occulted (orange) images; detectability curve (green)

curve is the coronagraphic contrast curve. The green dashed curve is the azimuthal standard deviation versus separation (the detectability). As of now, our MEC on-sky contrast is around $\sim 10^{-3}$ at 2 λ/D and detectability is around $\sim 10^{-4}$ at 2 λ/D. We have some ways to go before we can push into the high-contrast regime. Our hardware and software upgrades should get us there over the next few years.

3.3 Future Plans

3.3.1 Upgrades to MEC

Future hardware upgrades include a new anti-reflection coated science grade array which will roughly double the quantum efficiency and include fabrication process improvements that should greatly improve pixel yield. The MKID Pipeline will also be undergoing continual improvements which will allow us to more accurately determine the energy of each incident photon and to better remove false counts. For additional details on how future array improvements will affect the performance of MEC, see Dodkins et al. (2020).

3.3.2 Wavefront Sensing and Control

MEC has already done on-sky speckle nulling using a code derived from Bottom et al. (2016b) and demonstrated significant suppression of the quasistatic speckle halo which will be published in a future paper. This is the first step towards making MEC both a science camera and an effective focal plane wavefront sensor. Development is proceeding

to speed speckle nulling up to allow suppression of not just quasi-static speckles, but fast atmospheric speckles, with expected full probing and cancellation cycles occurring at frequencies of at least 200 Hz. The implementation of more advanced coherent differential imaging (CDI) probing techniques (Matthews et al., 2017) are also being developed for use both in post-processing and in real time.

In the long term, a fully optimized real time control package using the Frazin algorithm (Frazin, 2016, 2018) or similar predictive control (Males & Guyon, 2018) and sensor fusion approaches could help MEC use all available information simultaneously to approach fundamental photon noise limits and enable detection and characterization of smaller planets closer to their parent star. This technology will allow the next generation of instruments on 30-m class telescopes to potentially detect and characterize rocky planets in the habitable zones of nearby M-dwarfs.

3.3.3 Science Goals

MEC was designed with the goal of enabling imaging of exoplanets in reflected light. Figure 3.14 shows all currently known planets with their separation plotted against the expected contrast ratio. With MEC we hope to reach final contrasts of at 10^{-7} at 2 λ/D after post-processing, enabling the imaging of at least GJ 876 b. This contrast limit is theoretically achievable by MEC given the inner working angle of the instrument and assuming we are photon noise dominated. Future papers, as mentioned above, will detail the use of both high speed realtime and post-processing techniques to reach this noise

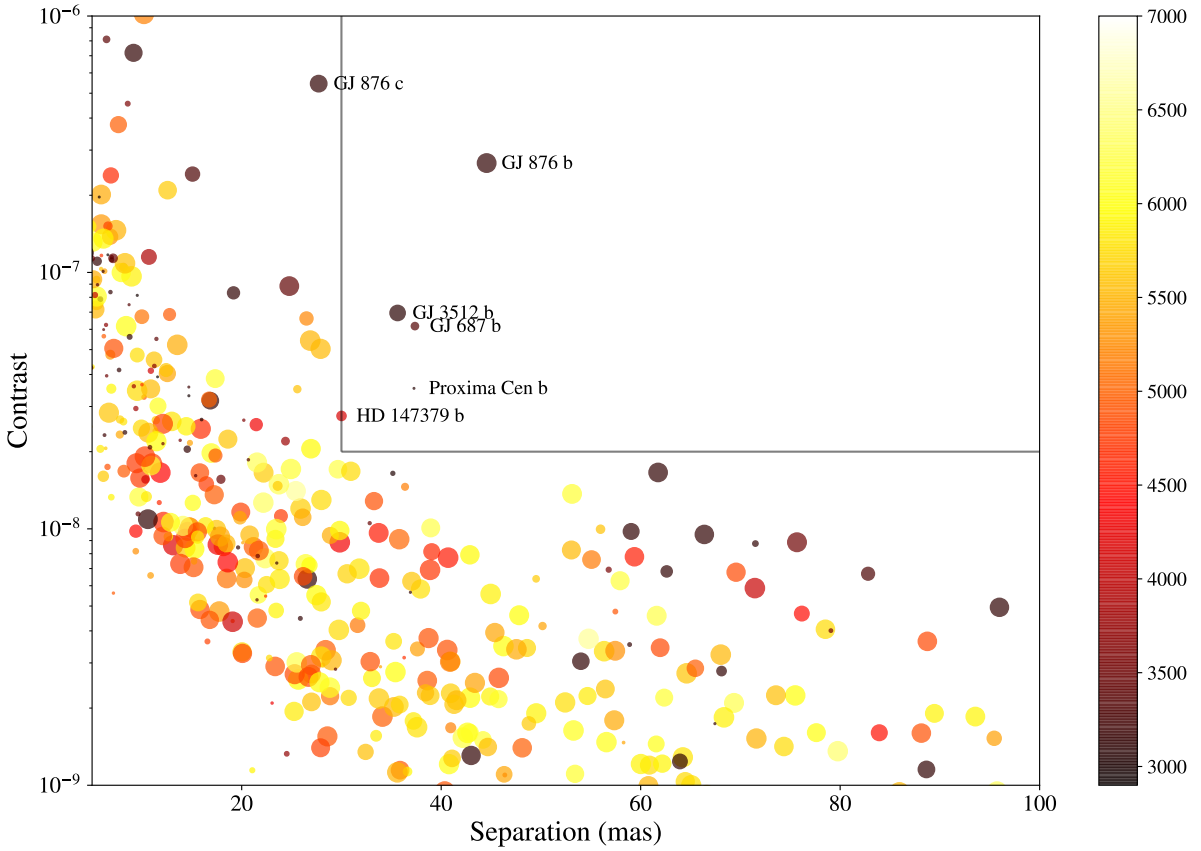

Figure 3.14 Angular separation vs. contrast for known exoplanets viewable with MEC/SCExAO and it's companion instrument DARKNESS (Meeker et al., 2018) on MagAO-X. The size of the point represents the radius of the planet, and the color of the point represents the T_{eff} of the host star. The horizontal line at 2×10^{-8} and the vertical line at 30 mas are meant to guide the eye to the most promising targets, which are labelled with their common names. Of these targets, GJ 876 b is by far the most promising.

limit and ultimately enhance the discovery reach of SCExAO.

In addition to reflected light planets, MEC is also a powerful tool for the discovery and characterization of young giant planets still glowing from the heat of their formation. The shorter wavelengths MEC probes allows for superior angular resolution, and the high final contrast at small inner working angles, due to focal plane wavefront sensing and novel post-processing, should allow us to probe new parameter space.

Chapter 4

Binaries in Open Clusters

4.1 Introduction

Stellar multiplicity is ubiquitous: nearly all high-mass stars live in binaries (Duchêne & Kraus, 2013) and around half of nearby Solar-mass field stars are binaries (Raghavan et al., 2010). It is also a function of environment: binaries in dense environments are especially subject to dynamical evolution with interactions changing or disrupting their orbits (Binney & Tremaine, 2008). Indeed, binaries (and higher order systems) are rarer in dense globular clusters, where frequent, strong dynamical encounters serve to disrupt wide binaries and harden tight binaries (Vesperini et al., 2011; Vesperini et al., 2013; Lucatello et al., 2015). Such encounters are rarer in the less dense environments of open clusters (Portegies Zwart et al., 2010). Yet open clusters show observed binary fractions ranging from 13% to 70% for solar-type stars (Duchêne & Kraus, 2013), while NGC 2516 could have a total binary fraction as high as 85% (Jeffries et al., 2001). The binary

fraction does not appear to show a clear dependence on the cluster's age, density, or chemical composition (Portegies Zwart et al., 2010; Duchêne & Kraus, 2013).

Open clusters are co-natal, co-eval environments through which we can explore stellar multiplicity as a universal outcome of star formation (Goodwin, 2010). The properties of stellar binaries in open clusters may be used to probe a cluster's initial conditions. For example, Griffiths et al. (2018) discussed how the presence of massive binaries on wide orbits gives insight to the cluster's initial density and structure.

Astrophysical parameters, luminosity functions, and stellar orbital properties have also been studied across clusters (e.g. Kharchenko et al., 2005, 2009, 2013; Griffin, 2012). The period distribution for binaries with solar-type primary stars in open clusters appears to be broad and unimodal over the range of 1 day to 10^4 years (Duchêne & Kraus, 2013). Wider binaries are much rarer: only two to three percent of stars with masses between 0.5 $M_\odot$ and 1.5 $M_\odot$ have binary companions on orbits between 300 and 3000 AU (Deacon & Kraus, 2020). The mass ratio distribution for solar-type stars is approximately flat for both spectroscopic and visual binaries, and substellar companions appear to be rare (Duchêne & Kraus, 2013).

Clusters are prime candidates for spectroscopic surveys due to the close grouping of the targets. Precision spectroscopic measurements enable characterization of the cluster chemical environment by determining elemental abundances (e.g. Bailey et al., 2018; Donor et al., 2020; Poovelil et al., 2020). Characterization of a cluster's chemical environment further informs simulations of the cluster's natal environment (e.g. Geller et al.,

2012; Geller, 2013; Geller et al., 2015). Precise stellar radial velocities (RVs) obtained through modeling spectral lines enable identification of binaries in open clusters (e.g. Sales Silva et al., 2014; Badenes et al., 2018; Martinez et al., 2020) and constraints on a cluster's multiplicity fraction (e.g. Guerrero et al., 2015; Kounkel et al., 2016; Nine et al., 2020). Meanwhile, absolute astrometry from *Gaia* has enabled a far more detailed picture of Galactic open clusters, with distances and proper motions, photometry, and astrometric membership determinations (Gaia Collaboration et al., 2016; Cantat-Gaudin et al., 2018; Gaia Collaboration et al., 2018). *Gaia*'s Early Third Data Release (EDR3 Gaia Collaboration et al., 2020; Lindegren et al., 2020) offers a factor of ∼2–4 improvement in astrometric precision over DR2, promising even better results. With snapshots of diverse systems at different ages in well-characterized environments, we can assemble a more complete picture of stellar multiplicity.

In this paper, we build upon previous work completed by Bailey et al. (2016, hereafter B16) and Bailey et al. (2018, hereafter B18) exploring multiplicity in the open clusters NGC 2516 and NGC 2422. B16 obtained multi-epoch spectroscopy for all stars with colors consistent with F5-K5 in a half-degree field centered on each of these clusters, identifying 40 and 22 RV binaries in the fields of NGC 2516 and NGC 2422, respectively (B18). Here, we extend this work with orbital fits for the majority of these binaries.

In Section 4.2 we review relevant details from B16 and B18, present a new epoch for a subset of the sample, and describe an extension of the B16 modeling process to double-lined systems. We report cluster ages and distances as measured by *Gaia* Data Release

2, review membership in light of parallaxes and proper motions provided by *Gaia* Early Data Release 3, and give the details of our orbital fitting process. Section 4.3 describes the results of the orbital fits and Section 4.4 discusses orbital parameter trends. We conclude with Section 4.5.

4.2 Observations and Data Analysis

In the following subsections, we discuss the observations, data reduction, and orbital fitting for the 62 binaries in the fields of NGC 2516 and NGC 2422. Table 4.1 summarizes the cluster properties determined in B16 and B18, with updates from *Gaia* DR2 and EDR3 where relevant.

4.2.1 Observations

B16 obtained multi-epoch spectroscopy in 2013 and 2014 for all photometric F5V-K5V members (N$\sim$125 each) in the core half-degree of the open clusters NGC 2516 and NGC 2422. They obtained $\sim$12 epochs ($\sim$2 hr exposures) in NGC 2516 and $\sim$10 epochs ($\sim$2.5 hr exposures) in NGC 2422, providing a temporal baseline of $\sim$1.1 years. B16 used Michigan/Magellan Fiber System (M2FS, Mateo et al., 2012), a multiplexed high-resolution optical fiber-fed spectrograph – deployed at the Magellan/Clay 6.5 meter telescope at Las Campanas Observatory – in its cross-dispersed echelle mode for order 49 (7160-7290 Å) to obtain a total of $\sim$2700 spectra. B16 selected order 49 for its combination of stellar and telluric absorption lines to provide a simultaneous RV and wavelength reference.

Observations had a median resolution $R \sim 50,000$ and a mean per-pixel signal-to-noise ratio (S/N) of 55. This configuration has a limiting RV precision of 25 m/s, with a median per-epoch precision of 80 m/s.

Here we incorporate an additional epoch for 36 stars in NGC 2516 obtained from a 3 hr exposure taken in February 2016 with a median S/N of ∼107, extending 33 of our targets to a baseline of ∼3.25 years. This epoch benefits from a newer M2FS filter tailored to the measured optical blaze, significantly improving throughput albeit with a slightly different wavelength coverage of 7180-7360 Å. We reduce these spectra following B16.

B16 targeted NGC 2516, a 120-150 Myr cluster (Meynet et al., 1993; Kharchenko et al., 2005; Sung et al., 2002; Fritzewski et al., 2020) at 415 pc (Gaia Collaboration et al., 2018) and NGC 2422, a 74 - 130 Myr cluster (Loktin et al., 2001; Kharchenko et al., 2005) at 487 pc (Gaia Collaboration et al., 2018) for a balance of astrophysical and instrumental reasons described therein. Gaia Collaboration et al. (2018) used *Gaia* DR2 photometry to derive cluster ages by fitting color-magnitude diagrams (CMDs). While this gave an age consistent with prior works for NGC 2422 (130 Myr), it gave NGC 2516 an age of 300 Myr, far above the age range found previously. The new *Gaia* analysis confirms that several luminous, mid B-type stars are indeed members of NGC 2516. Recent work by Fritzewski et al. (2020) indicates that NGC 2516 is comparable to the Pleiades in terms of rotation period distribution and age; we therefore take 150 Myr as an appropriate upper age limit for this cluster.

4.2.2 Data Reduction and Cluster Properties

B18 fit model stellar spectra to the data in order to simultaneously extract each target's $T_{\rm eff}$, [Fe/H], [α/Fe], $v_r \sin i$ (stellar rotational velocity), and line of sight RV. They used the relation of Torres et al. (2010) to compute stellar masses, which we adopt herein, albeit updated with new SB2 spectral fits.

To obtain RVs for double-lined systems, we employed the reduction package from B16 in binary mode where the model is constructed using a pair of stellar spectra. In this mode, the model gains a second set of stellar parameters and a flux fraction parameter that sets the normalized flux ratio between the component stellar spectra. We first performed an initial round of fits where we held one T_{eff} fixed to that in B18, the other with that as a starting guess. We used the [Fe/H] and [α/Fe] values from B18 for both components throughout. The veiling and $v_r \sin i$ parameters were fixed to unity and zero for both stars. This first round was carefully supervised to determine initial RV guesses within $\sim$ 20 km/s ($\sim$10 pixels) for all components. The spectra were then refit for stellar parameters, allowing T_{eff} (and the coupled $log(g)$), $v_r \sin i$, and flux fraction to float while still holding veiling fixed (these parameters are presented in Table 4.2). We ensured component spectra remained associated with the same spectral source by checking stellar parameters (e.g. whether stellar temperatures flipped) and by refitting each spectrum with the adopted stellar properties intentionally flipped to check for an improved chi-square. We also separately validated this by fitting Keplerian orbits (Section 4.2.4) to the absolute value of the RV difference, $|\mathrm{RV}_1 - \mathrm{RV}_2|$. This approach obtained

the correct orbital parameters even if the several spectra were assigned to the wrong source; we could then straightforwardly check the source identification. We adopted stellar parameters and flux fraction as described in B16 but excluding fits with RVs closer than 1.5 resolution elements. We then performed a final round of fits to determine RVs with the adopted stellar parameters and flux fraction constant, but allowing veiling to float for each component.

We got successful two component fits for targets 146-012622, 147-012265, 147-012499, 377-035049, 378-036176, and 378-036252, all of which were identified as SB2s in B18, as well as 379-035982 and 147-012164, two SB2s that were missed in B18. We were not able to get reliable orbits for these last two SB2s, as they appear to be higher order systems whose details we will discuss in Section 4.3. Stellar and fit properties of these stars are reported in Table 4.2.

Two stars reported as SB2 in B18, 147-012424 and 379-035886, proved impossible to fit for a second stellar component. Both were identified as non-members by Gaia (see next section) and on further review of their spectra we now believe these to be off main-sequence, possibly chemically peculiar stars with a significant number of unfit lines. We treated them as SB1s in our analysis, and ultimately excluded 379-035886 for poor data quality.

Table 4.1. Cluster Properties

System	NGC 2516	NGC 2422
Age (Myr)	120-150	74-130
Distance (pc)	415	487
N_{Mem}	2518	907
R_{core} (pc)	$0.9^{+0.23}_{-0.17}$	1.58 ± 0.75
Cluster RV (km/s)	24.5 ± 0.12	35.97 ± 0.09
σ_{RV} (m/s)	734 ± 104	750 ± 65
Stellar Jitter (m/s)	74 ± 9	138 ± 2
[Fe/H] (dex)	-0.08 ± 0.01	-0.05 ± 0.02
[α/Fe] (dex)	0.03 ± 0.01	0.02 ± 0.01
Binary Fraction (%)	100^{+0}_{-15}	62 ± 16

Note. — Age as described §4.2.1, distance and membership per Gaia Collaboration et al. (2018). Core radii derived from King profile modelling for 0.87 - 1.48 $M_\odot$ stars for NGC 2516 (Jeffries et al., 2001) and 0.7 - 1.0 $M_\odot$ stars for NGC 2422 (Prisinzano et al., 2003). Everything else per B18. σ_{RV} is the cluster velocity dispersion.

Table 4.2. Stellar Properties for SB2 Targets

Target ID	T_{eff} 1 (K)	T_{eff} 2 (K)	log(g) 1	log(g) 2	[Fe/H] (dex)	[α/Fe] (dex)	$v_r \sin i$ 1 (km/s)	$v_r \sin i$ 2 (km/s)	Flux 1 (%)
146-012622	5602 ± 22	5473 ± 21	4.54	4.55	-0.57	0.10	7.5 ± 0.2	6.5 ± 0.1	53 ± 1
147-012265	6273 ± 29	5538 ± 88	4.43	4.54	-0.25	0.04	16.4 ± 0.1	13.8 ± 0.6	80 ± 1
147-012499	5242 ± 16	4904 ± 29	4.58	4.62	-0.36	0.06	4.9 ± 0.2	10.1 ± 0.2	61 ± 0
377-035049	4881 ± 30	4756 ± 23	4.61	4.63	-0.24	0.06	2.7 ± 0.5	2.8 ± 0.6	54 ± 1
378-036176	6151 ± 46	5982 ± 19	4.46	4.48	-0.44	0.06	6.6 ± 0.1	5.6 ± 0.1	57 ± 1
378-036252	6281 ± 24	4879 ± 78	4.43	4.63	-0.14	0.02	9.1 ± 0.1	6.0 ± 0.5	89 ± 0

4.2.3 Gaia EDR3 Membership

Figures 4.1 and 4.2 show all Gaia stars and M2FS targets in $1.^{\circ}5 \times 1.^{\circ}5$ fields centered on NGC 2516 and NGC 2422, respectively. We use red to indicate Gaia astrometric members as determined using EDR3 (for M2FS targets studied in this paper) or DR2 (all else, Gaia Collaboration et al., 2018), with larger symbols indicating M2FS targets and crosses indicating those that are RV-variable. The solid black line marks the half-degree M2FS field of view (FOV).

While B18 used the mean stellar RV to determine membership, we are now able to rely exclusively on the precise astrometry of *Gaia* EDR3. A target was considered a cluster member if its parallax and proper motions from *Gaia* EDR3 (Gaia Collaboration et al., 2020) were within 5σ and 2 mas/yr respectively of the cluster parallaxes and proper motions from Gaia Collaboration et al. (2018). All of the astrometric member singles have mean stellar RVs within 5 km/s of the cluster RV. The updates to membership in light of *Gaia* DR3 precision astrometry do not change the binary fraction within the margins of error reported by B18.

4.2.4 Orbital Fitting

We fit Keplerian orbits to our radial velocity measurements using a custom adaptation of `orvara`[1], a package for fitting stellar and exoplanet orbits using Markov Chain Monte Carlo (MCMC) through the package `ptemcee` (Foreman-Mackey et al., 2013; Vousden

[1] https://github.com/t-brandt/orbit3d

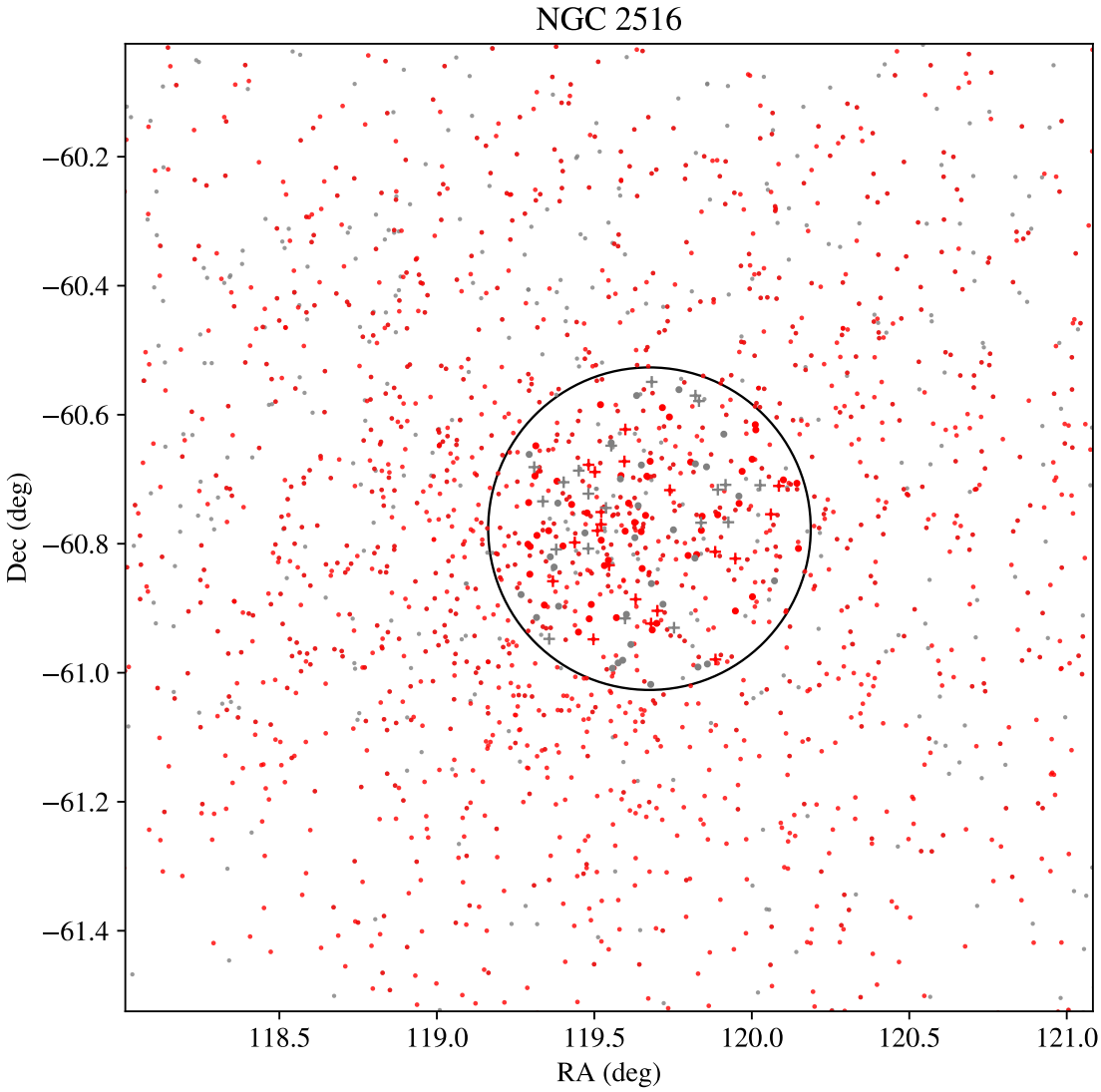

Figure 4.1 The NGC 2516 Field. The solid black circle marks the half-degree M2FS field of view. Red and grey points indicate membership and non-membership, respectively, based on EDR3 astrometry (for M2FS targets studied in this paper) or DR2 (all else, Gaia Collaboration et al., 2018). Larger symbols indicate M2FS targets and crosses indicate those that are RV-variable.

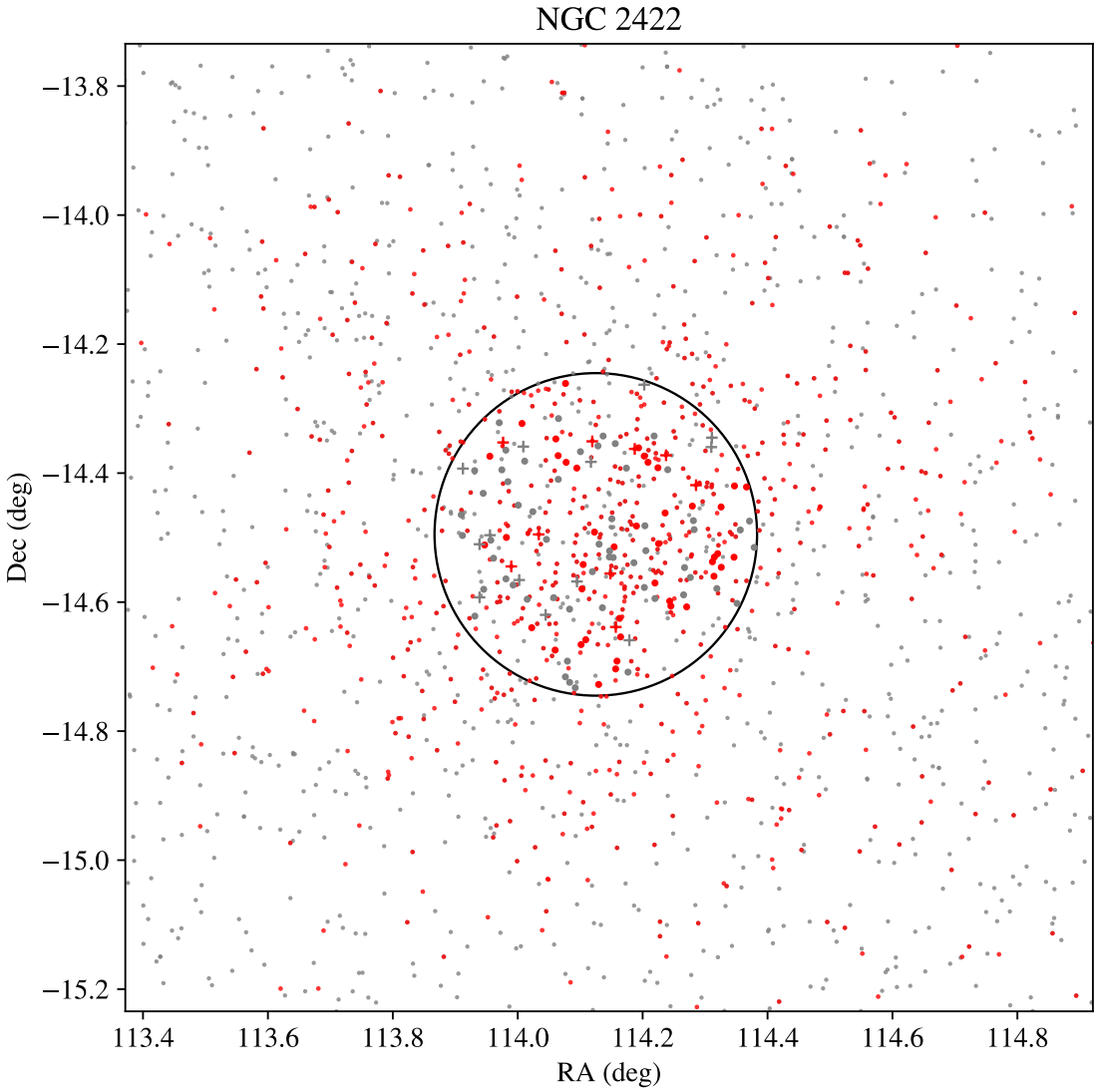

Figure 4.2 The NGC 2422 Field. The solid black circle marks the half-degree M2FS field of view. Red and grey points indicate membership and non-membership, respectively, based on EDR3 astrometry (for M2FS targets studied in this paper) or DR2 (all else, Gaia Collaboration et al., 2018). Larger symbols indicate M2FS targets and crosses indicate those that are RV-variable.

et al., 2016). We ran our fits using 20 temperatures and 200 walkers with 1 million steps each; we fit for the orbital period P, eccentricity e, mean anomaly at a reference epoch $\lambda_{\rm ref}$, argument of periastron ω, RV semi-amplitude K, and barycenter radial velocity RV_0. Our adaptation of `orvara` differs from the published version in its ability to analytically marginalize over K and ω, depending on the choice of prior for K. The fits that we present here adopt a uniform prior on all parameters. With this choice, K and RV_0 enter the likelihood linearly (Wright & Howard, 2009) and may be analytically marginalized out. The resulting chain stores the maximum likelihood values of K and RV_0 at the fixed values of the other parameters.

We fit the SB2 targets with a double-component fit with an additional parameter for the ratio of the radial velocity semi-amplitudes of the primary and secondary components, equivalent to their mass ratio:

$$K_{\rm ratio} = -\frac{\mathrm{RV}_2}{\mathrm{RV}_1} = \frac{K_2}{K_1} = \frac{M_1}{M_2}. \tag{4.1}$$

We calculated a per-star multiplicative factor, σ_χ, which would inflate the B18 RV errors σ_i sufficiently to yield a reduced χ^2 of 1, equivalent to a χ^2 of the number of degrees of freedom (DOF). The inflation factor σ_χ is simply the square root of the computed reduced χ^2, and is reported in Tables 4.3 and 4.4 in Section 4.3. This ad-hoc factor accounts for sources of RV uncertainty not previously addressed. For example, a poor estimate of the photon-weighted exposure midpoint could introduce uncertainty due to stellar acceleration throughout the exposure. We fold all of these effects into σ_χ, apply it

to σ_i, and rerun our chains a second time in order to derive the parameters and confidence intervals we report.

4.2.5 Secondary Mass Distributions

We obtain a secondary mass distribution for SB2s directly from the mass ratio parameter distribution. We obtain a secondary mass distribution for the remaining systems by computing a random mass for each step in the MCMC chain. First, we obtain a random inclination from a geometric prior by drawing $\cos(i)$ uniformly between 0 and 1. We then use the equation for radial velocity semi-amplitude

$$K = \left(\frac{2\pi G}{P}\right)^{\frac{1}{3}} \frac{M_2}{(M_1 + M_2)^{\frac{2}{3}}} \frac{\sin(i)}{\sqrt{1-e^2}} \tag{4.2}$$

to obtain a secondary mass, solving directly for the case of one real root. Values for M_1 were already found in B16, as described in Section 4.2. Figures 4.6-4.8 show secondary mass distributions for systems which returned a usable fit (see Section 4.3).

4.3 Results

Due to varying spectral quality and survey limitations, data sets for some RV variable stars lead to higher quality fits than for others. Our RV data are sparse, consisting of groups of 2-3 data points taken over a few days, with month or year-long gaps in between. For a minority of our targets this leads to aliasing and multimodal results,

which we discuss on a case-by-case basis in Sections 4.3.2-4.3.4.

Twenty-five systems did not return satisfactory orbital solutions. Some returned orbits with one-day periods equivalent to the window function, or orbits which placed the companion inside the primary at closest approach. Eighteen of these systems had low-signal-to-noise ($\sigma_{obs}/\sigma_{meas} \leq 5$) RV data sets; we did not consider their data quality high enough for further exploration. Five more systems had signal-to-noise ratios above this threshold, but we could not get reliable fits from the data at hand; we need either more epochs or a longer observational baseline. Some of these may simply be very active young stars. The final two systems, 147-012164 and 379-035982, stand out as systems worth further exploration because their component RVs suggest the presence of an additional companion. We discuss the status of these potentially higher-order systems in Section 4.3.

Tables 4.3 and 4.4 report the median values and 68% confidence intervals of the parameters for the remaining 37 systems with usable fits. These tables report target ID, **M**ember/ **N**on-**M**ember, line-of-sight stellar rotational velocity ($v_r \sin i$), and the binary properties as obtained in 4.2.4. We also report the system's primary mass (M_1) and median mass ratio ($q = M_1/M_2$, see §4.2.5). SB2s have a superscript 'D' next to their target ID and multimodal targets have an asterisk next to their periods. The final column, σ_χ, gives the multiplicative constant applied to RV measurement errors to get a reduced χ^2 of ~ 1. Out of these 37 systems, 11 had orbital solutions consistent with periods exceeding their observational baselines: their period posteriors lacked an upper

bound. We only report the 90% lower limits of the period and mass ratio distributions for these systems, as all their other orbital parameters (with the exception of the RV_0) are poorly constrained.

4.3.1 Orbital Plots

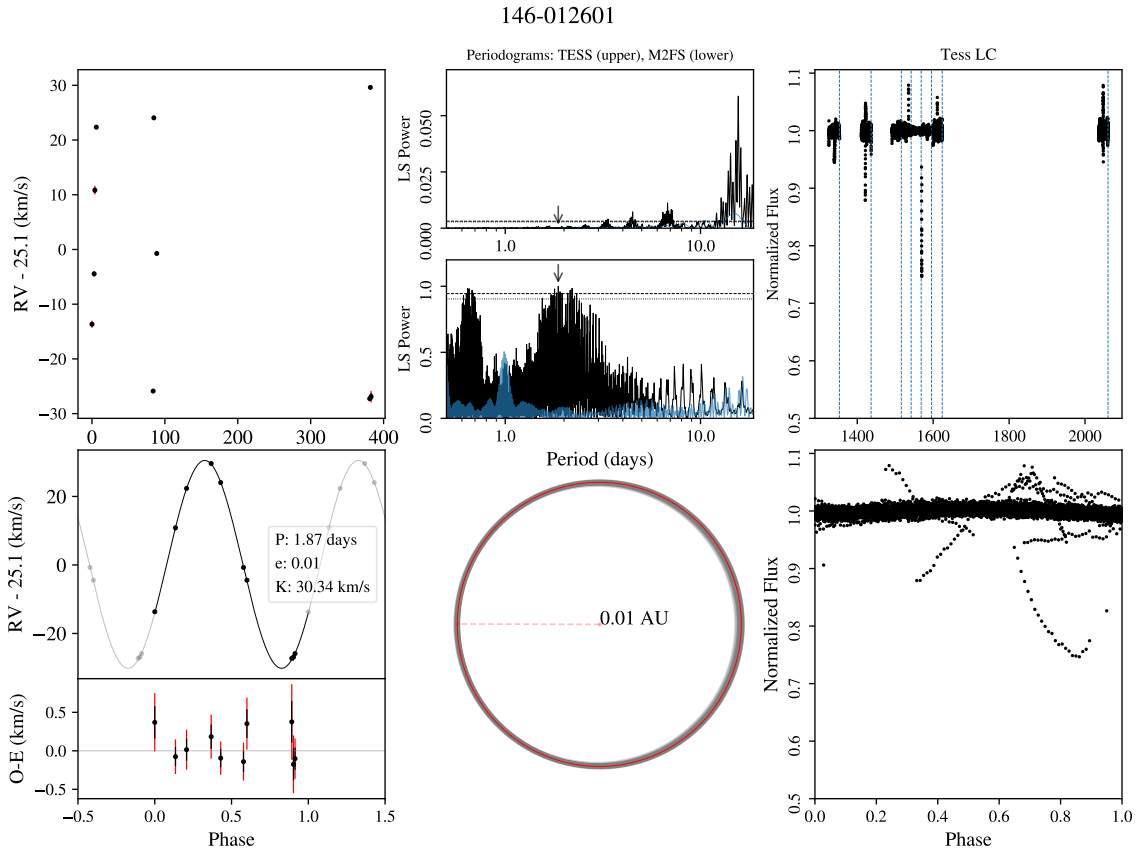

Figure 4.3 146-012601 (V=13.9) is a member of NGC 2516. The primary has a T_{eff} of 5116 ± 19 K and a $v_r \sin(i)$ of 16.1 ± 0.2 km/s. This system has a period of 1.87 ± 0.00 days (e=$0.01^{+0.01}_{-0.00}$) and a semi-amplitude of $30.37^{+0.22}_{-0.23}$ km/s. The systemic RV is $25.10^{+0.06}_{-0.05}$ km/s, -6.06 ± 6.20 km/s from the RV reported in B18. The primary mass is $0.82 M_{\odot}$ and the system's mass ratio is $0.25^{+0.14}_{-0.03}$. The phase-folded TESS lightcurve is suggestive of tidal ellipsoidal distortion.

Plots of the 37 systems for which we obtained a usable fit may be found in Appendix

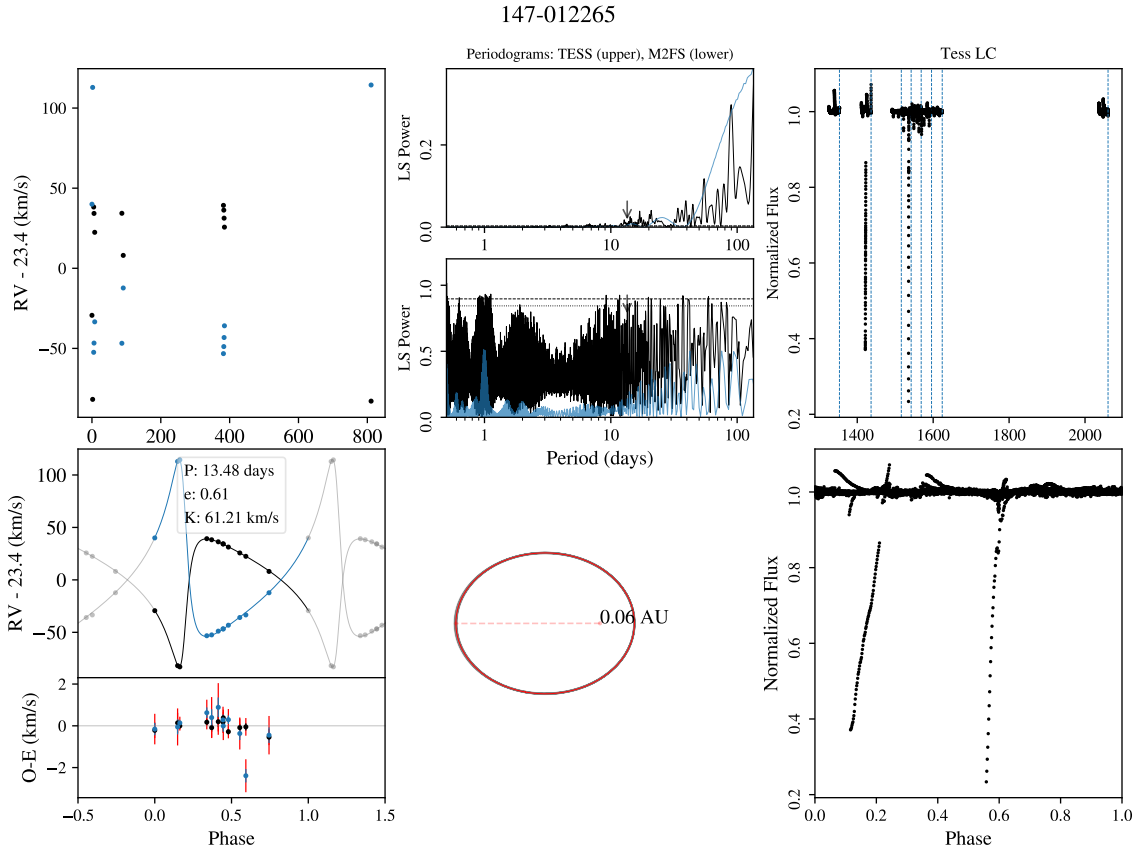

Figure 4.4 147-012265 (V=12.1) is a member of NGC 2516. The stars have a T_{eff} of 6482 ± 29 K and 5419 ± 29 K and $v_r \sin(i)$ of 16.4 ± 0.1 and 13.8 ± 0.1 km/s. This double-lined system has a period of 13.48 ± 0.00 days (e=0.61 ± 0.00) and a semi-amplitude of $61.18^{+0.27}_{-0.22}$ km/s. The systemic RV is 23.42 ± 0.04 km/s, -14.25 ± 11.53 km/s from the RV reported in B18. The primary mass is $1.12 M_{\odot}$ and the system's mass ratio is 0.73 ± 0.00. This is the shortest-period eccentric binary in our sample.

A. Three examples, Figures 4.3-4.5, are included here as they highlight target peculiarities that will be discussed in the following sections. The left column displays the RV time series (top) and the phase-folded RV with the maximum-likelihood fit (bottom). The very bottom plot displays the RV residuals from the fit. The black error bars are the original RV errors from B18. The red error margins show the extra error inflation from the per-star multiplicative factor, σ_χ.

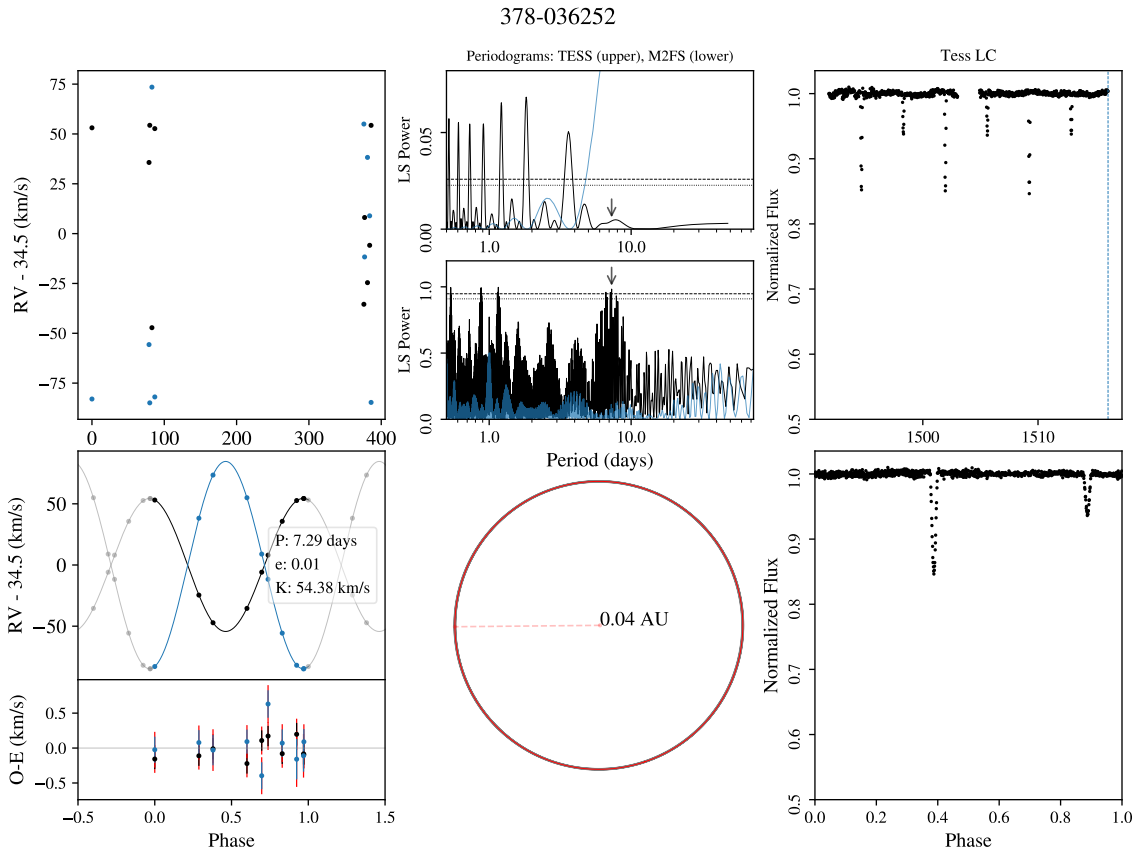

Figure 4.5 378-036252 (V=12.5) is a member of NGC 2422. The stars have a T_{eff} of 6495 ± 24 K and 4755 ± 24 K and $v_r \sin(i)$ of 9.1 ± 0.1 and 6.0 ± 0.1 km/s. This double-lined system has a period of 7.29 ± 0.00 days (e=0.01 ± 0.00) and a semi-amplitude of 54.39 ± 0.11 km/s. The systemic RV is 34.51 ± 0.02 km/s, -13.42 ± 11.97 km/s from the RV reported in B18. The primary mass is $1.15 M_{\odot}$ and the system's mass ratio is 0.64 ± 0.00. Primary and secondary eclipses are evident in the phase-folded TESS lightcurve.

We used `eleanor` (Feinstein et al., 2019) to download the Transiting Exoplanet Survey Satellite (TESS, Ricker et al., 2015) light curves for all available targets. We used these light curves to check for photometric periods of our binary systems and to examine individual systems more closely, particularly those that might demonstrate eclipses or tidal ellipsoidal distortion. The right column displays these TESS lightcurves, with the

bottom plot showing the lightcurve phase-folded over the period.

We compute a Lomb-Scargle periodogram for each of the targets, using a maximum period of twice our observational baseline and a minimum period of half a day. We caution that periodogram peaks at or below ∼1.1 day are likely due to aliasing from our observational cadence. The center column shows Lomb-Scargle periodograms of TESS (top) and M2FS data (bottom). The dotted and dashed lines denote 95% and 99% significance, respectively and the arrow points to the maximum-likelihood period. The faint blue lines represent their respective window functions. The bottom center plot shows a random selection of orbits from the MCMC chains with the maximum-likelihood orbit in red.

The following three subsections discuss targets of note, including those with multimodal posteriors. Corner plots for all targets with reliable orbits can be found in Appendix A.

4.3.2 NGC 2516

- **146-012455** (Fig. A15) has a bimodal posterior distribution, with two orbital modes of different eccentricities but each with a ∼110 day period.

- **146-012601** (Fig. A24) has a phase-folded TESS lightcurve which shows that the primary star may exhibit tidal ellipsoidal distortion.

- **147-012164** is an SB2 for which we could not get a reliable binary fit; its stellar parameters are not stable. This is because it is a higher-order system: we see

clear evidence for a third star in its spectra. The data could support a full orbital characterization with substantial extra work.

- **147-012175** (Fig. A25), **147-012270** (Fig. A30), and **148-012906** (Fig. A13) have broad, multimodal posterior distributions. Their best-fit orbits are accompanied by many long-period, high-eccentricity orbits. We recommend examining their corner plots in Appendix A to fully appreciate their posterior distributions.

- **147-012308** (Fig. A14) has a bimodal posterior distribution. The posterior has peaks at periods of ∼55 days and ∼210 days. The longer period orbits are more eccentric.

4.3.3 NGC 2422

- **378-036252** (Fig. A3) has a phase-folded TESS lightcurve which clearly shows the primary and secondary eclipses caused by the two stars in the system orbiting about one another.

- **378-036328** (Fig. A16) has a bimodal posterior distribution. The posterior has peaks at periods of ∼43 days and ∼28 days. The longer period orbits are more eccentric.

- **378-036814** (Fig. A32) has a broad, multimodal posterior distribution, spanning many possible orbits. We recommend examining its corner plot in Appendix A.

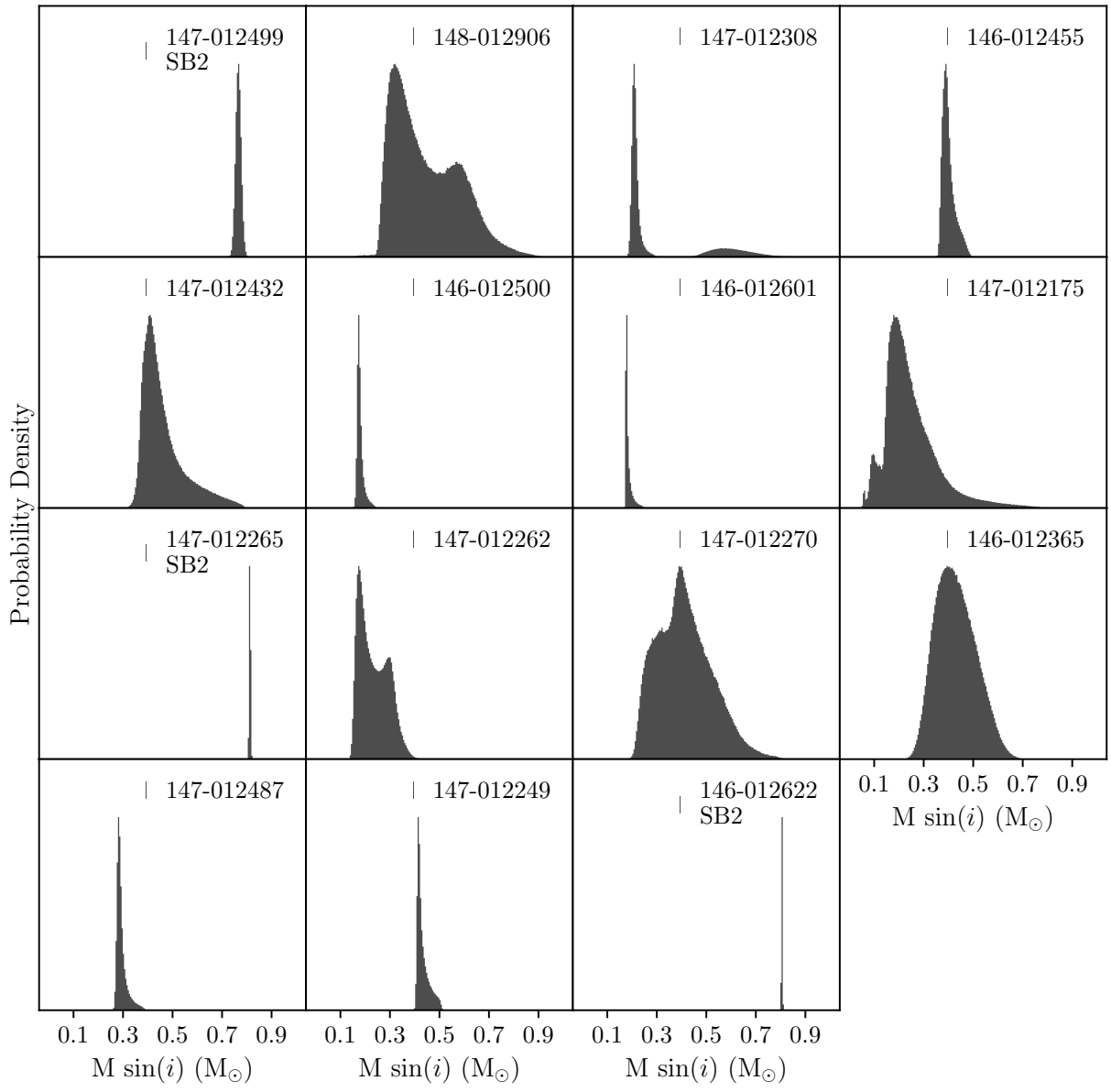

Figure 4.6 Secondary mass distributions for NGC 2516 members.

- **379-035982** is an SB2 for which we could not get a reliable binary fit. While there is no visual evidence for a third star in its spectra, this system's stellar properties and component RVs do not make sense without an additional companion. Further

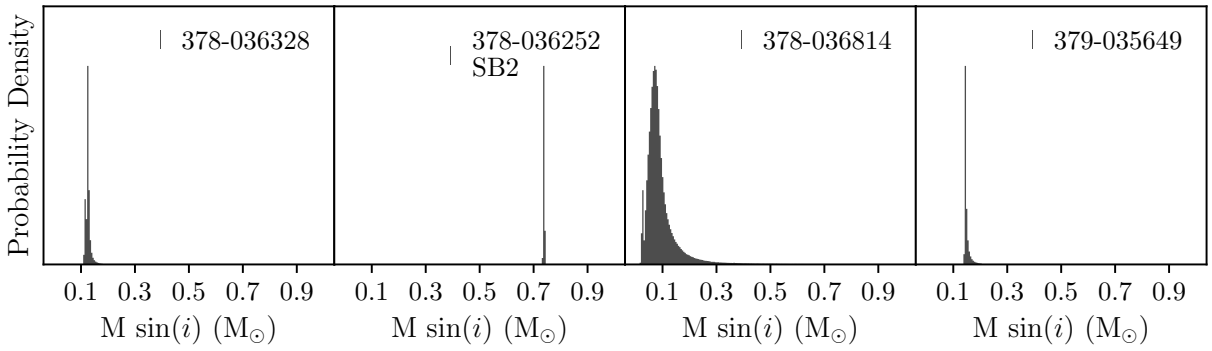

Figure 4.7 Secondary mass distributions for NGC 2422 members.

observations are needed in order to fully characterize this system.

4.3.4 Non-Members

- **146-012557** (Fig. A7) has a bimodal posterior distribution. The posterior has peaks at periods of ∼600 days and ∼150 days. The longer period orbits are more eccentric.

- **379-036194** (Fig. A8) has a trimodal posterior distribution. The posterior has peaks at periods of ∼130 days, ∼65, and ∼250 days. The longer period orbits are more eccentric.

- **379-036197** (Fig. A9) has a broad, multimodal posterior distribution, spanning many possible orbits. We recommend examining its corner plot in Appendix A.

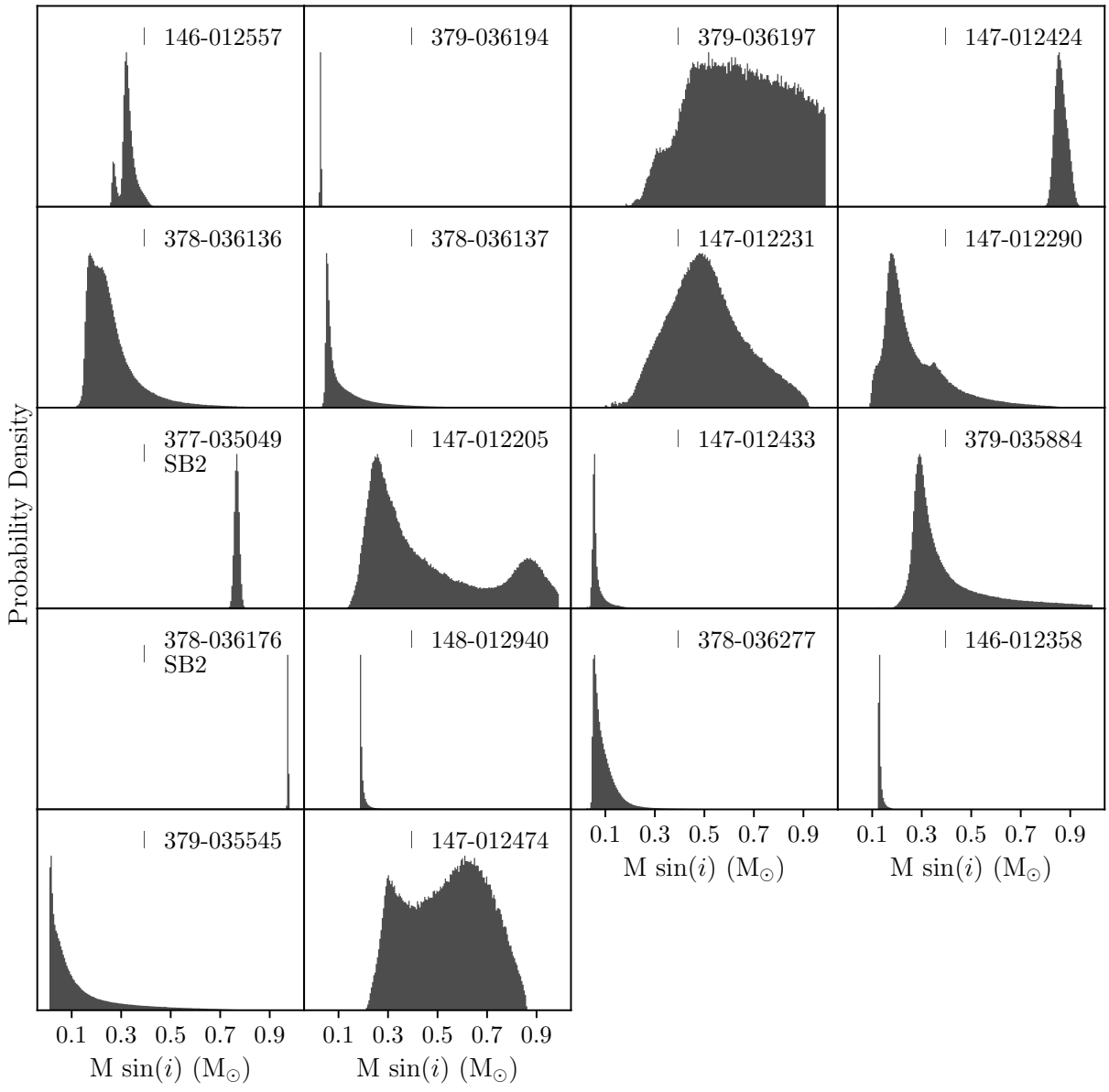

Figure 4.8 Secondary mass distributions for cluster non-members.

4.4 Discussion

Our Keplerian orbital fits provide a dynamical picture of binarity in NGC 2516 and NGC 2422. Figure 4.10 shows the astrophysically significant parameters: period, mass

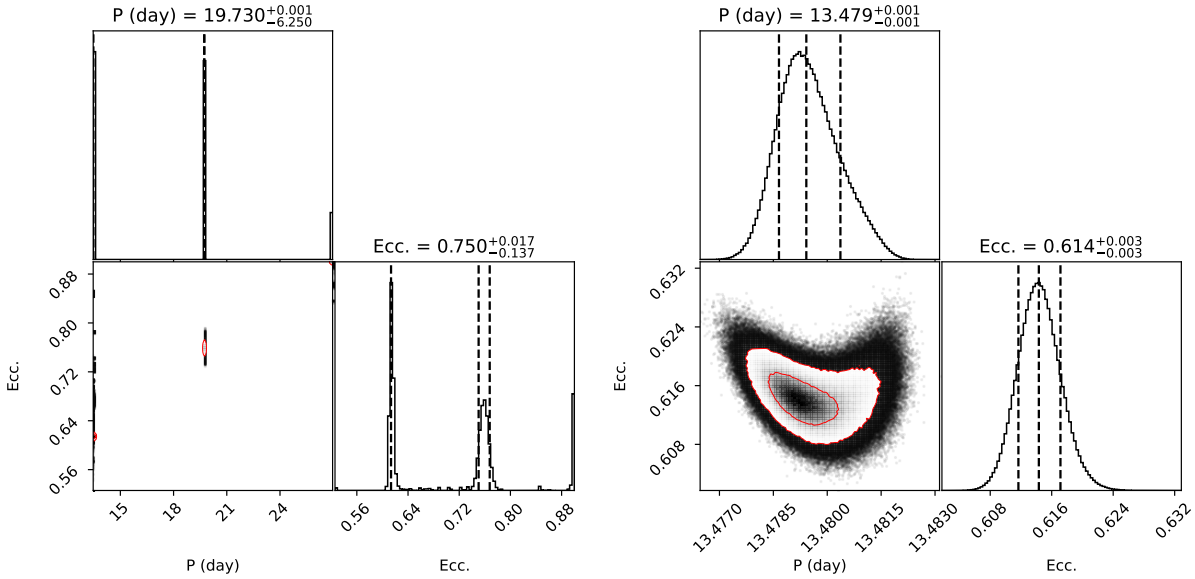

Figure 4.9 The period and eccentricity posteriors for NGC 2516 cluster member 147-012265 fit without (left) and with (right) a barycentric prior. The fits with the barycentric prior are well-constrained and unimodal.

ratio, and eccentricity. Our systems span periods of two days to several years. All of the <10 day systems are nearly circular, while the wider binaries show a range of eccentricities. In this section we discuss the significance of these results for binary star formation and evolution.

4.4.1 Orbital Parameter Distributions: Cluster vs Field

We find that our mass ratio distributions of binaries in the clusters as well as the field (see Figure 4.10) are relatively flat, consistent with previous works (e.g. Raghavan et al., 2010; Duchêne & Kraus, 2013). Recently, other works have noted an excess of equal-mass ($q \gtrsim 0.95$) twins at close separations (e.g. Pinsonneault & Stanek, 2006; Simon & Obbie, 2009; Kounkel et al., 2019) on top of a uniform distribution for systems with $q < 0.95$.

While we do not have a large enough sample among either cluster or field binaries to probe for a twin excess, we do note the equal-mass binaries we found in the hopes that this data might be incorporated into a future study of twin binaries. Two of our NGC 2516 SB2s, 146-012622 and 147-012499, have mass ratios of 0.97 and 0.93 respectively. Two field SB2s 377-035049 and 378-036176, are close-in binaries with mass ratios of 0.99 and 0.94 respectively.

We note an excess of short-period (P<100 days) binaries along the cluster members. Moreover, a statistically significant excess of the systems with periods greatly exceeding their observational baselines (some of which have periods over 1000 days) are cluster non-members. The physical explanation for this effect is likely that these stars, which have a magnitude consistent with an FGK star at $\sim$ 450 pc despite being distant background stars, are giants which cannot physically support short-period companions.

4.4.2 *Gaia* EDR3 and RV Binary Characterization

We use the high-precision parallaxes and proper motions from *Gaia* EDR3 to definitively establish cluster membership. This enables us to impose a prior on the radial velocity of a system's barycenter when fitting the orbit of an astrometric member. As a result, we obtain excellent fits for nearly all cluster members, collapsing the multimodality present in the posteriors of several targets into well-constrained and unimodal posteriors. Figure 4.9 shows an example of this effect for NGC 2516 member 147-012265. The application of a prior effected reliable, unimodal fits for some of our notable systems, examples

being 146-012601, a tight circular binary (P$\sim$ 2 days), and 146-012622, an equal-mass SB2. 147-012265, an eccentric SB2, had over five visible orbital modes originally, but the application of the prior identified the dominant mode. As we discuss in the following section, 147-012265 is the shortest-period eccentric binary in our sample.

Future spectroscopic binary surveys over clusters will benefit from the use of *Gaia* EDR3 precision astrometry to not only exclusively target cluster members (losing less observational time to background stars mistaken as photometric members), but also to impose barycentric priors using *Gaia* cluster RVs and velocity dispersions in the fitting process. This will result in well-constrained orbital solutions for each cluster member, generating cluster-wide distributions of periods, eccentricities, and mass ratios. Characterizing the binaries within open clusters will give insight into the dynamical evolution of the cluster and enable the mapping of orbital properties across different populations of binaries.

4.4.3 Tidal Circularization

Binary stars exert tidal forces on each other, causing them to *circularize* over time, i.e. approach a state where stellar rotation is synchronous with binary orbital motion and the stellar rotation axis is aligned with the normal to the orbital plane of motion (Mazeh, 2008). Eccentricity damps due to the mismatch between the orbital frequency, which varies with orbital phase if $\varepsilon > 0$, and the rotational frequency of either star.

Orbital characterization of binary star systems in open clusters enables us to de-

termine the transition period separating circular from eccentric binaries. For example, Mathieu et al. (2004) determined the tidal circularization cutoff period for NGC 188 ($\sim$ 6 Gyr) to be around 15 days using spectroscopic binaries. Meibom & Mathieu (2005)'s sample of transition periods for 8 coeval systems shows a tendency for longer transition periods in older clusters. Geller et al. (2021) recently found a tidal circularization cutoff period of $11^{+1.1}_{-1.0}$ days for open cluster M67 ($\sim$4 Gyr), in agreement with the value of $12.1^{+1.0}_{-1.5}$ days found by Meibom & Mathieu (2005). All the clusters in the sample in the age range of NGC 2516 and NGC 2422 have cutoff periods within the 5-15 day window.

We find two binaries within this period window: 147-012265, a SB2 in NGC 2516 (e$\sim$0.61, P$\sim$13.48 days), and 378-036252, a circular binary in NGC 2422 (P$\sim$7.29 days). Both of these systems are consistent with previous work. Meibom & Mathieu (2005) find a tidal circularization cutoff period for M35, a cluster around the same age as NGC 2516 and NGC 2422, of 10.2 days. Notably, all stars in their M35 sample with periods under 20 days are less eccentric than 147-012265. The discovery of other systems in NGC 2516 and NGC 2422 within this period window, particularly short-period eccentric binaries, would help constrain the transition period for these clusters. 147-012265 and 378-036252, however, could contribute to a meta-analysis looking at binaries within this crucial period window along with other systems from clusters of similar ages.

4.4.4 Substellar Companions

The dearth of stars with a companion mass in the brown dwarf range (5-80 M_{Jup}) is known as the 'brown dwarf desert' (Marcy & Butler, 2000). Less than 1% of Sun-like stars have brown dwarf companions according to Grether & Lineweaver (2006).

Consistent with the brown dwarf desert, almost all of our well-constrained binaries have stellar companions. Only one field star, 379-036194, has a secondary with a median derived mass of 0.036 solar masses, which is below the hydrogen-burning limit. Recent work by Fontanive et al. (2019) found that a significant fraction of brown dwarf desert inhabitants are themselves members of higher-order systems. This provides additional motivation for the full characterization of the higher-order systems we introduced in Section 4.3, 147-012164 and 379-035982, to determine if either of these might have a substellar companion.

4.5 Conclusion

In this paper we derive the Keplerian orbital parameters of 37 binary stars in the young open clusters NGC 2516 and NGC 2422. The systems span periods of two days to several years, mass ratios from ∼0.1 to unity, and eccentricities up to ∼0.9. One of these systems, 147-012265, has an unusually high eccentricity of 0.62 given its 13.48 day orbital period. Another, 378-036252, is an eclipsing binary; TESS will enable a more complete characterization. One non-member system, 379-036194, has a companion with a secondary mass in the brown dwarf range. We are not able to reliably fit two

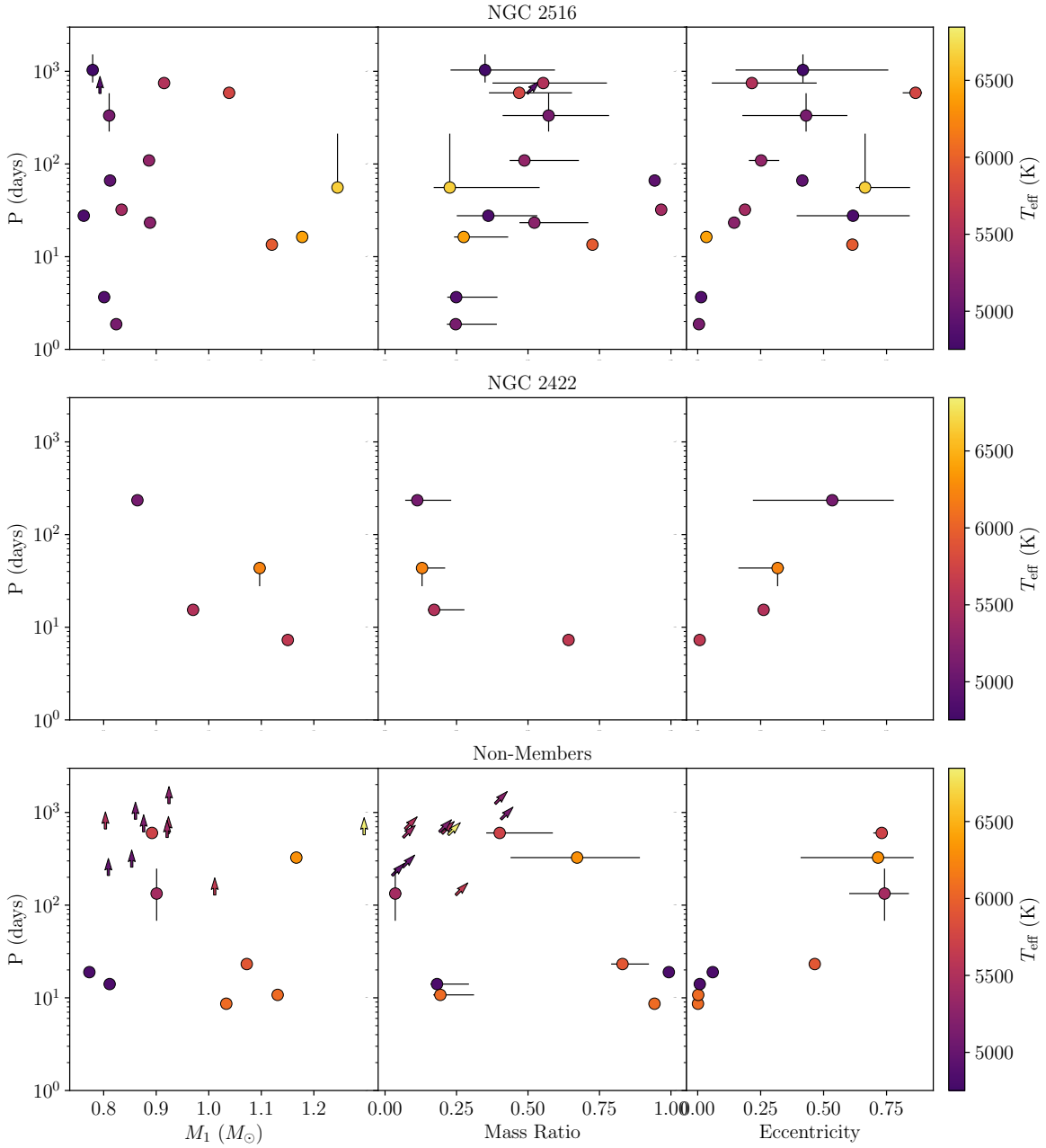

Figure 4.10 Scatter plots of the physically meaningful binary parameters for members of NGC 2516 and NGC 2422 (top and middle rows) and non-members (bottom row). The markers are colored according to the temperature of the primary star. The panels from left to right display in turn the system's primary mass, median mass ratio (M_2/M_1), and median eccentricity plotted against the median period, with $\pm1\sigma$ errors. We represent the 11 systems with weakly constrained orbital solutions with an arrow placed at the 90% quantile lower limit in the mass-period and mass ratio-period plots only.

systems, 147-012164 and 379-035982, as binaries. Their RVs indicate they are higher-order systems and require either substantial more work or spectroscopic observations for complete characterization.

We use precise stellar parallaxes and proper motions from *Gaia* EDR3 to definitively determine target membership status. Thanks to the *Gaia* EDR3 astrometric membership, we impose an extra barycentric prior on all cluster members in the fitting process. This transformed the multimodal posteriors seen in several systems before the application of the prior into well-constrained and unimodal solutions. We urge future cluster surveys to incorporate *Gaia* EDR3 astrometry to set an informative prior on the barycenter RV of cluster members.

We find that the mass ratio distribution for binaries across the clusters and the field is relatively flat, consistent with previous works. We identify four nearly equal-mass binaries (two in NGC 2516 and two in the field). We also find an overabundance of long-period systems in the field relative to the clusters. This is likely a selection effect: many of these field stars are background giants which are physically unable to have short-period companions.

Finally, we find two systems with periods between 5-15 days, which is the critical window from Meibom & Mathieu (2005) in which the tidal circularization cutoff period separating circular from eccentric binaries was found for clusters of a similar age to our own. One of them, 378-036252, is a circular binary in NGC 2422 with a period around 7 days. The other, the $\sim$13.5-day NGC 2516 SB2 147-012265, is more eccentric than all

similar-period systems found by Meibom & Mathieu (2005) in M35 (a cluster of a similar age to NGC 2516). These binaries should be included in future analyses of circularization across similarly-aged clusters.

In conclusion, we present orbital parameters for 37 stars in open clusters NGC 2516 and NGC 2422. Our results describe the types of binaries within these clusters, and have the potential to provide insight into the evolution of these clusters. They will also help constrain stellar multiplicity and binary properties across different stellar populations.

Table 4.3. Binary Solutions in the Field of NGC 2516

Target ID	Mem.	$v_r \sin i$ (km/s)	Period (days)	Ecc.	λ	ω	K (km/s)	RV_0 (km/s)	M_1 ($M_\odot$)	q (M_2/M_1)	σ_χ
146-012358	N	4.48 ± 0.25	14.07 ± 0.00	0.01 ± 0.01	$1.81^{+3.37}_{-1.15}$	$1.32^{+1.15}_{-3.14}$	$11.67^{+0.10}_{-0.09}$	69.46 ± 0.09	0.81	$0.18^{+0.11}_{-0.02}$	2.24
146-012365	M	6.34 ± 0.09	$586.17^{+17.42}_{-20.56}$	$0.87^{+0.03}_{-0.05}$	$3.35^{+0.24}_{-0.28}$	$-0.92^{+0.15}_{-0.20}$	$16.18^{+4.25}_{-4.05}$	$23.59^{+0.53}_{-0.57}$	1.04	$0.47^{+0.18}_{-0.11}$	1.21
146-012455	M	7.57 ± 0.06	$109.17^{+0.80*}_{-2.01}$	$0.25^{+0.07}_{-0.05}$	$2.16^{+0.32}_{-0.33}$	$-1.43^{+0.13}_{-0.20}$	$15.05^{+0.20}_{-0.17}$	$25.20^{+0.43}_{-0.97}$	0.89	$0.49^{+0.19}_{-0.05}$	1.72
146-012500	M	8.83 ± 0.23	3.66 ± 0.00	0.01 ± 0.01	$3.28^{+1.92}_{-2.07}$	$0.21^{+1.95}_{-2.35}$	$24.15^{+0.66}_{-0.62}$	$24.31^{+0.32}_{-0.30}$	0.80	$0.25^{+0.14}_{-0.03}$	5.43
146-012557	N	4.93 ± 0.17	$601.32^{+17.97*}_{-46.34}$	$0.73^{+0.01}_{-0.03}$	$6.27^{+0.00}_{-0.01}$	$-3.05^{+0.09}_{-0.03}$	10.35 ± 0.05	$-26.87^{+0.10}_{-0.31}$	0.89	$0.40^{+0.19}_{-0.05}$	1.00
146-012601	M	16.07 ± 0.14	1.87 ± 0.00	$0.01^{+0.01}_{-0.00}$	$4.05^{+0.89}_{-1.90}$	$0.01^{+1.80}_{-0.86}$	$30.37^{+0.22}_{-0.23}$	$25.10^{+0.06}_{-0.05}$	0.82	$0.25^{+0.14}_{-0.03}$	1.81
146-012622[D]	M	9.16 ± 0.30	32.12 ± 0.00	0.19 ± 0.00	5.19 ± 0.01	-0.39 ± 0.01	42.54 ± 0.08	24.07 ± 0.00	0.83	0.97 ± 0.00	1.19
147-012175	M	10.83 ± 0.21	$1032.93^{+491.71*}_{-275.57}$	$0.42^{+0.34}_{-0.27}$	$3.56^{+1.42}_{-1.35}$	$-1.61^{+4.38}_{-0.92}$	$5.19^{+6.05}_{-1.20}$	$24.32^{+0.69}_{-0.72}$	0.78	$0.35^{+0.24}_{-0.12}$	3.01
147-012205	N	3.97 ± 0.09	$\geq 128.70^*$	-	-	-	-	$21.26^{+9.20}_{-5.35}$	1.01	≥ 0.25	6.34
147-012231	N	4.53 ± 0.44	$\geq 1243.58^*$	-	-	-	-	$21.02^{+6.05}_{-2.34}$	0.92	≥ 0.38	4.96
147-012249	M	6.73 ± 0.10	23.28 ± 0.00	0.14 ± 0.01	$4.54^{+0.07}_{-0.06}$	-2.43 ± 0.07	26.07 ± 0.22	$23.90^{+0.05}_{-0.04}$	0.89	$0.52^{+0.19}_{-0.05}$	5.20
147-012262	M	4.61 ± 0.30	$27.65^{+0.01}_{-0.03}$	$0.62^{+0.23}_{-0.22}$	3.02 ± 0.16	-1.57 ± 0.15	$19.66^{+17.07}_{-6.09}$	24.49 ± 0.71	0.76	$0.36^{+0.17}_{-0.11}$	4.56
147-012265[D]	M	16.94 ± 0.52	13.48 ± 0.00	0.61 ± 0.00	5.09 ± 0.01	-2.20 ± 0.01	$61.18^{+0.27}_{-0.22}$	23.42 ± 0.04	1.12	0.73 ± 0.00	2.46
147-012270	M	7.47 ± 0.56	$333.26^{+247.00*}_{-109.35}$	$0.43^{+0.16}_{-0.25}$	$4.94^{+1.12}_{-4.81}$	$0.63^{+1.97}_{-3.24}$	$11.40^{+3.46}_{-1.50}$	$24.50^{+0.72}_{-0.71}$	0.81	$0.57^{+0.21}_{-0.16}$	3.95
147-012290	N	3.36 ± 0.12	$\geq 617.62^*$	-	-	-	-	$11.52^{+4.18}_{-1.08}$	0.88	≥ 0.19	2.14
147-012308	M	37.77 ± 0.23	$55.77^{+157.01*}_{-0.12}$	$0.66^{+0.18}_{-0.04}$	$0.63^{+0.51}_{-0.09}$	$-1.85^{+0.72}_{-0.07}$	$11.93^{+13.32}_{-0.45}$	$25.08^{+0.76}_{-0.12}$	1.24	$0.23^{+0.31}_{-0.06}$	2.20
147-012424	N	6.39 ± 0.22	23.15 ± 0.00	0.46 ± 0.01	3.66 ± 0.01	-0.49 ± 0.01	$46.17^{+0.69}_{-0.66}$	17.79 ± 0.27	1.07	$0.83^{+0.09}_{-0.04}$	2.99
147-012432	M	5.87 ± 0.09	≥ 576.26	-	-	-	-	$24.36^{+0.74}_{-0.67}$	0.79	≥ 0.50	2.36
147-012433	N	4.06 ± 0.30	$\geq 256.90^*$	-	-	-	-	$26.51^{+0.23}_{-1.57}$	0.85	≥ 0.06	1.00
147-012474	N	3.68 ± 0.09	≥ 844.99	-	-	-	-	$-1.61^{+5.20}_{-10.94}$	0.86	≥ 0.41	2.57
147-012487	M	10.38 ± 0.11	16.32 ± 0.00	0.03 ± 0.01	$5.70^{+0.34}_{-0.59}$	$1.52^{+0.41}_{-0.37}$	$18.27^{+0.38}_{-0.36}$	$23.77^{+0.24}_{-0.23}$	1.18	$0.28^{+0.16}_{-0.03}$	3.73
147-012499[D]	M	8.42 ± 1.28	66.31 ± 0.05	0.42 ± 0.01	1.80 ± 0.04	0.30 ± 0.02	$30.77^{+0.56}_{-0.54}$	24.96 ± 0.08	0.81	0.94 ± 0.01	3.26
148-012906	M	15.26 ± 0.98	$747.20^{+10.04*}_{-99.41}$	$0.22^{+0.26}_{-0.16}$	$4.96^{+0.70}_{-3.40}$	$0.14^{+0.98}_{-1.49}$	$8.92^{+2.46}_{-2.00}$	$24.47^{+0.70}_{-0.54}$	0.92	$0.55^{+0.22}_{-0.18}$	2.42
148-012940	N	5.96 ± 0.07	10.76 ± 0.00	0.00 ± 0.00	$3.93^{+1.50}_{-2.38}$	$0.16^{+1.43}_{-1.71}$	15.09 ± 0.05	32.52 ± 0.02	1.13	$0.19^{+0.12}_{-0.02}$	1.00

*Denotes target with a multimodal fit

[D]SB2: q given is $1/K_{\rm ratio}$

Table 4.4. Binary Solutions in the Field of NGC 2422

Target ID	Mem.	$v_r \sin i$ (km/s)	Period (days)	Ecc.	λ	ω	K (km/s)	RV_0 (km/s)	M_1 ($M_\odot$)	q (M_2/M_1)	σ_χ
377-035049[D]	N	6.82 ± 1.66	18.92 ± 0.00	0.06 ± 0.01	$3.14^{+0.10}_{-0.11}$	$2.27^{+0.11}_{-0.09}$	46.06 ± 0.38	21.04 ± 0.13	0.77	0.99 ± 0.01	2.75
378-036136	N	9.02 ± 0.20	≥ 591.51	-	-	-	-	$35.47^{+1.41}_{-1.37}$	0.92	≥ 0.20	1.00
378-036137	N	3.01 ± 0.22	≥ 663.45*	-	-	-	-	$119.96^{+1.27}_{-0.66}$	0.80	≥ 0.07	1.00
378-036176[D]	N	9.13 ± 1.23	8.64 ± 0.00	0.00 ± 0.00	$4.45^{+1.14}_{-2.99}$	$-1.36^{+3.35}_{-1.13}$	46.40 ± 0.06	41.92 ± 0.00	1.03	0.94 ± 0.00	1.59
378-036252[D]	M	9.84 ± 0.32	7.29 ± 0.00	0.01 ± 0.00	$5.04^{+0.22}_{-0.21}$	$1.46^{+0.21}_{-0.22}$	54.39 ± 0.11	34.51 ± 0.02	1.15	0.64 ± 0.00	1.37
378-036277	N	3.40 ± 0.14	≥ 537.19*	-	-	-	-	$27.33^{+0.33}_{-0.61}$	0.92	≥ 0.06	1.00
378-036328	M	7.93 ± 0.07	$43.54^{+0.02\ *}_{-15.82}$	$0.32^{+0.03}_{-0.16}$	$1.60^{+0.47}_{-0.08}$	$-2.02^{+0.15}_{-0.59}$	$6.98^{+0.12}_{-0.08}$	$36.08^{+0.23}_{-0.26}$	1.10	$0.13^{+0.08}_{-0.02}$	1.00
378-036814	M	6.91 ± 0.11	$234.54^{+25.54*}_{-22.66}$	$0.53^{+0.24}_{-0.32}$	$3.80^{+0.81}_{-0.38}$	$-0.82^{+0.40}_{-1.11}$	$3.11^{+3.30}_{-0.95}$	$36.10^{+0.48}_{-0.33}$	0.86	$0.11^{+0.12}_{-0.04}$	1.00
379-035545	N	4.26 ± 0.21	≥ 208.73*	-	-	-	-	$114.93^{+1.17}_{-2.99}$	0.81	≥ 0.02	2.33
379-035649	M	4.37 ± 0.09	15.40 ± 0.00	0.26 ± 0.01	0.17 ± 0.02	-1.07 ± 0.02	11.83 ± 0.08	35.92 ± 0.04	0.97	$0.17^{+0.11}_{-0.02}$	1.00
379-035884	N	19.03 ± 0.24	≥ 574.15	-	-	-	-	$59.09^{+1.42}_{-2.64}$	1.30	≥ 0.22	1.08
379-036194	N	4.12 ± 0.20	$133.39^{+114.48*}_{-65.54}$	$0.74^{+0.10}_{-0.14}$	$2.35^{+0.76}_{-1.20}$	$0.38^{+0.16}_{-0.13}$	1.85 ± 0.10	$105.73^{+0.34}_{-0.17}$	0.90	$0.04^{+0.02}_{-0.01}$	1.43
379-036197	N	6.60 ± 0.07	$325.95^{+9.35*}_{-8.87}$	$0.72^{+0.14}_{-0.31}$	$1.48^{+1.26}_{-0.89}$	$-0.43^{+0.37}_{-0.67}$	$67.49^{+165.55}_{-43.28}$	$26.86^{+37.83}_{-16.88}$	1.17	$0.67^{+0.22}_{-0.23}$	8.64

*Denotes target with a multimodal fit

[D]SB2: q given is $1/K_{\rm ratio}$

Appendix A

Orbital Plots and Corner Plots

We present the orbital plots for the 37 systems for which we obtained a usable fit. The left column displays the RV time series (top) and the phase-folded RV with the maximum-likelihood fit (bottom). The very bottom plot displays the RV residuals from the fit. The black error bars are the original RV errors from B18. The red error margins show the extra error inflation from the per-star multiplicative factor, σ_χ.

The center column displays TESS Lomb-Scargle periodogram (top) and M2FS LS periodograms (bottom). The dotted and dashed lines denote 95% and 99% significance, respectively. Each peridogram has an arrow hovering over the maximum likelihood period. The faint blue lines represent the window functions of the TESS and M2FS observations. The bottom plot in the center column shows a selection of orbits explored in the MCMC fitting process, with the maximum likelihood orbit in red. The right column displays the TESS lightcurves made using `eleanor`, with the bottom plot showing the

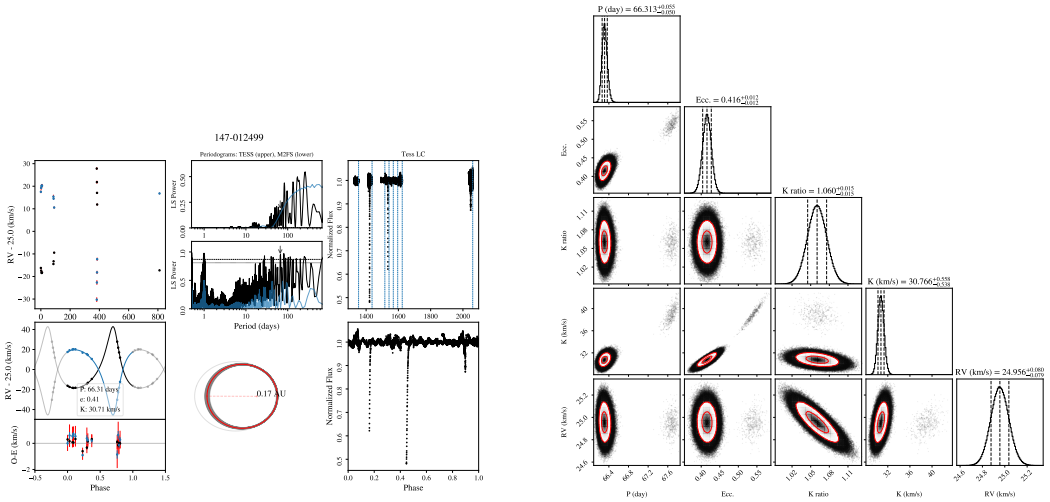

Figure A1 147-012499 (V=13.5) is a member of NGC 2516. The stars have a T_{eff} of 5119 ± 16 K and 4780 ± 16 K and $v_r \sin(i)$ of 4.9 ± 0.2 and 10.1 ± 0.2 km/s. This double-lined system has a period of 66.31 ± 0.05 days (e=0.42 ± 0.01) and a semi-amplitude of $30.77^{+0.56}_{-0.54}$ km/s. The systemic RV is 24.96 ± 0.08 km/s, 6.61 ± 4.09 km/s from the RV reported in B18. The primary mass is $0.81 M_{\odot}$ and the system's mass ratio is 0.94 ± 0.01. The TESS lightcurves show a periodic modulation of the primary star's flux.

lightcurve phase-folded over the period.

The text descriptions under the plots summarize the results of the fit, quoting each parameter's median value from the MCMC fit with errors representing $\pm 1\sigma$ values, assuming normalcy. The text descriptions also include updated membership status and some important notes about each target originally reported in B18, such as primary star temperature and rotational velocity.

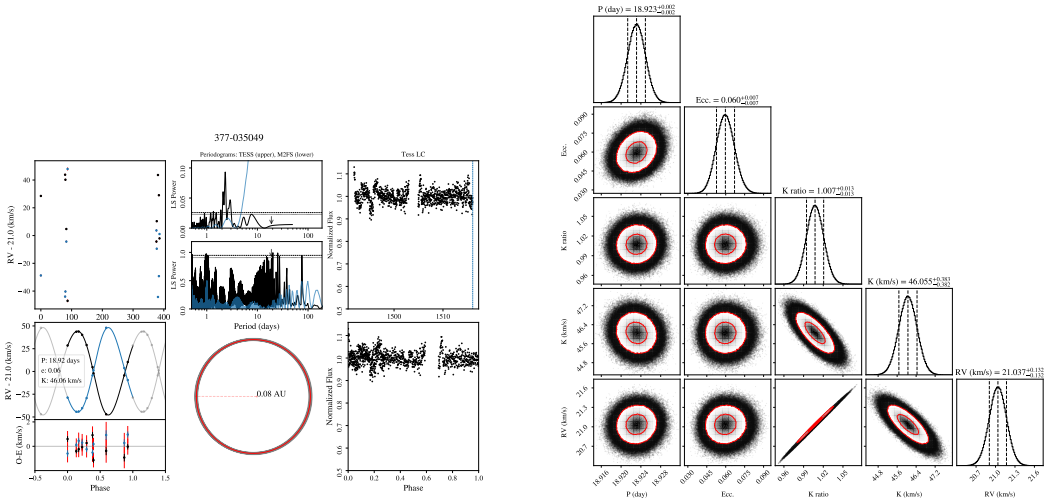

Figure A2 377-035049 (V=15.9) is a non-member in the field of NGC 2422, in contrast to B18. The stars have a T_{eff} of 4881±30 K and 4756±30 K and $v_r \sin(i)$ of 2.7±0.5 and 2.8±0.5 km/s. This double-lined system has a period of 18.92±0.00 days (e=0.06±0.01) and a semi-amplitude of 46.06 ± 0.38 km/s. The systemic RV is 21.04 ± 0.13 km/s, −16.30 ± 7.39 km/s from the RV reported in B18. The primary mass is $0.77 M_{\odot}$ and the system's mass ratio is 0.99 ± 0.01.

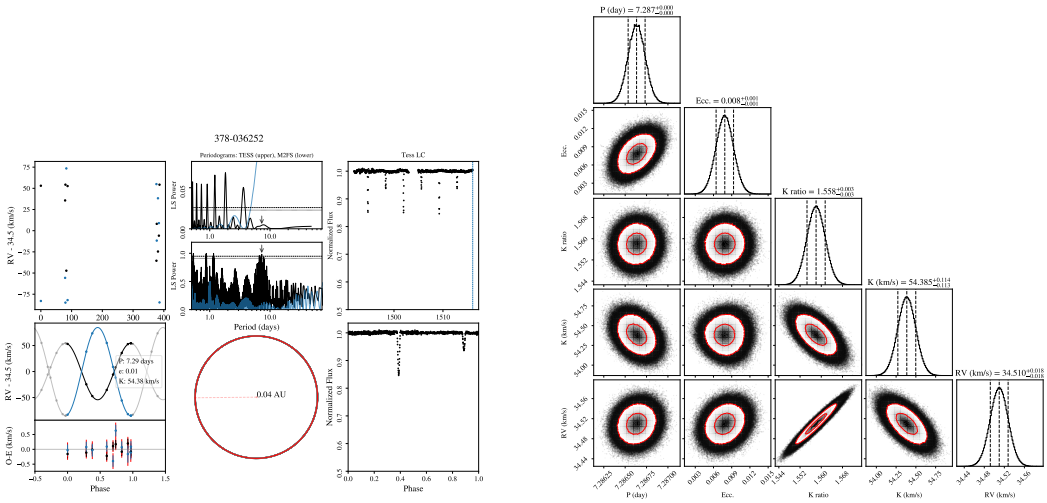

Figure A3 378-036252 (V=12.5) is a member of NGC 2422. The stars have a T_{eff} of 6495 ± 24 K and 4755 ± 24 K and $v_r \sin(i)$ of 9.1 ± 0.1 and 6.0 ± 0.1 km/s. This double-lined system has a period of 7.29 ± 0.00 days (e=0.01 ± 0.00) and a semi-amplitude of 54.39 ± 0.11 km/s. The systemic RV is 34.51 ± 0.02 km/s, −13.42 ± 11.97 km/s from the RV reported in B18. The primary mass is $1.15 M_{\odot}$ and the system's mass ratio is 0.64 ± 0.00. Primary and secondary eclipses are evident in the phase-folded TESS lightcurve.

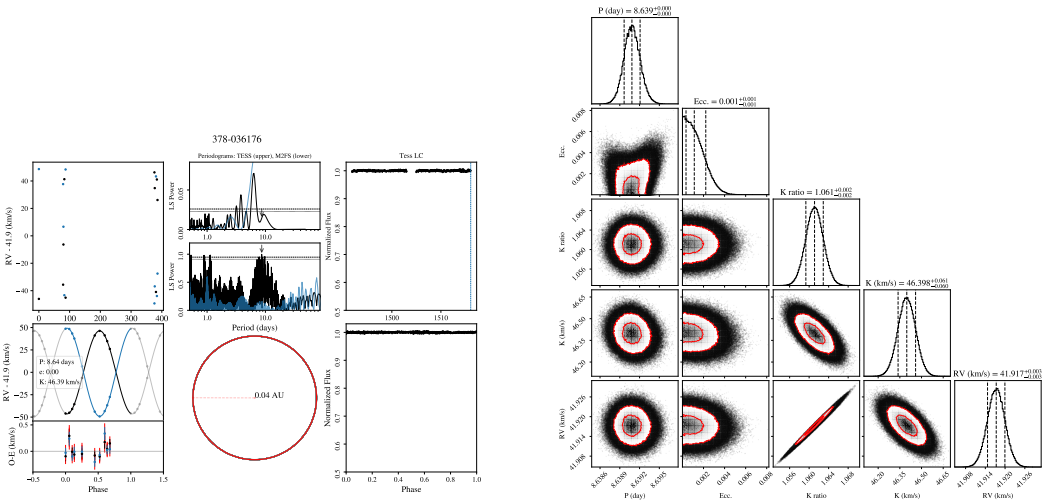

Figure A4 378-036176 (V=12.5) is a non-member in the field of NGC 2422. The stars have a T_{eff} of 6151 ± 46 K and 5982 ± 46 K and $v_r \sin(i)$ of 6.6 ± 0.1 and 5.6 ± 0.1 km/s. This double-lined system has a period of 8.64 ± 0.00 days (e=0.00 ± 0.00) and a semi-amplitude of 46.40 ± 0.06 km/s. The systemic RV is 41.92 ± 0.00 km/s, 37.58 ± 4.97 km/s from the RV reported in B18. The primary mass is $1.03 M_{\odot}$ and the system's mass ratio is 0.94 ± 0.00.

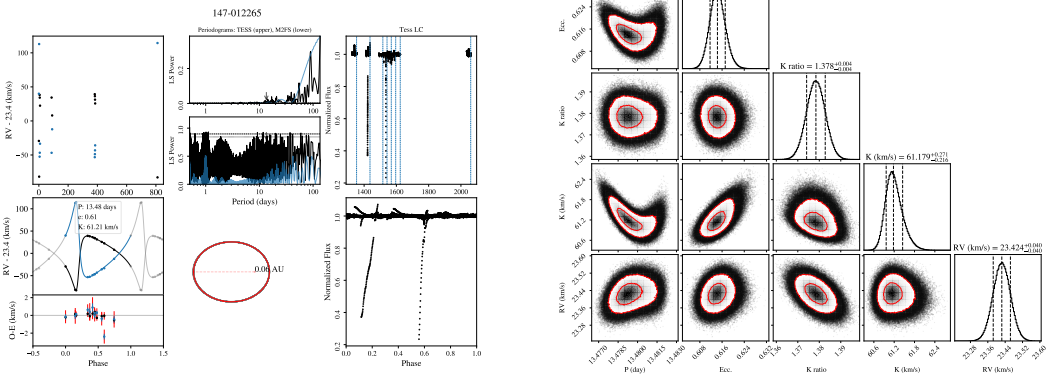

Figure A5 147-012265 (V=12.1) is a member of NGC 2516. The stars have a T_{eff} of 6482 ± 29 K and 5419 ± 29 K and $v_r \sin(i)$ of 16.4 ± 0.1 and 13.8 ± 0.1 km/s. This double-lined system has a period of 13.48 ± 0.00 days (e=0.61 ± 0.00) and a semi-amplitude of $61.18^{+0.27}_{-0.22}$ km/s. The systemic RV is 23.42 ± 0.04 km/s, -14.25 ± 11.53 km/s from the RV reported in B18. The primary mass is $1.12 M_{\odot}$ and the system's mass ratio is 0.73 ± 0.00.

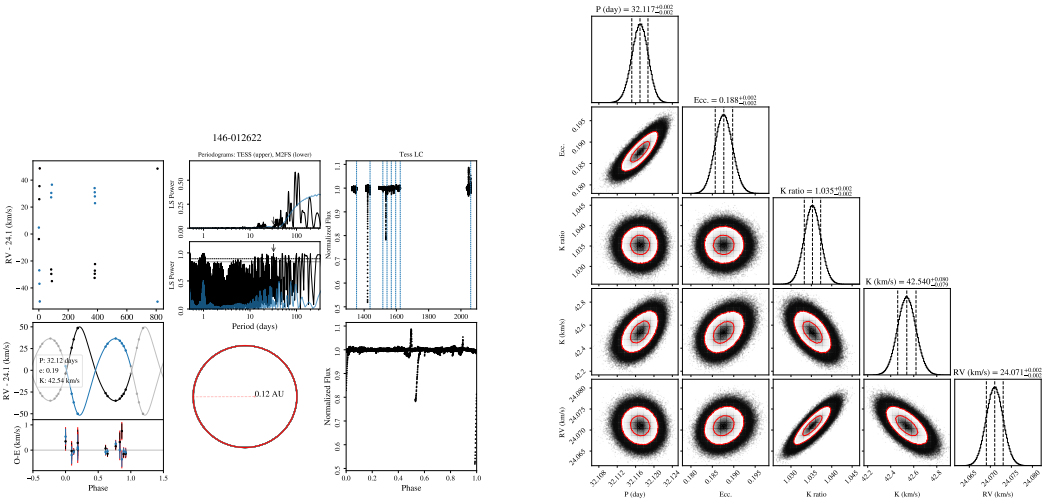

Figure A6 146-012622 (V=12.4) is a member of NGC 2516, in contrast to B18. The stars have a T_{eff} of 5485 ± 22 K and 5352 ± 22 K and $v_r \sin(i)$ of 7.5 ± 0.2 and 6.5 ± 0.2 km/s. This double-lined system has a period of 32.12 ± 0.00 days (e=0.19 ± 0.00) and a semi-amplitude of 42.54 ± 0.08 km/s. The systemic RV is 24.07 ± 0.00 km/s, 26.03 ± 4.02 km/s from the RV reported in B18. The primary mass is $0.83 M_{\odot}$ and the system's mass ratio is 0.97 ± 0.00.

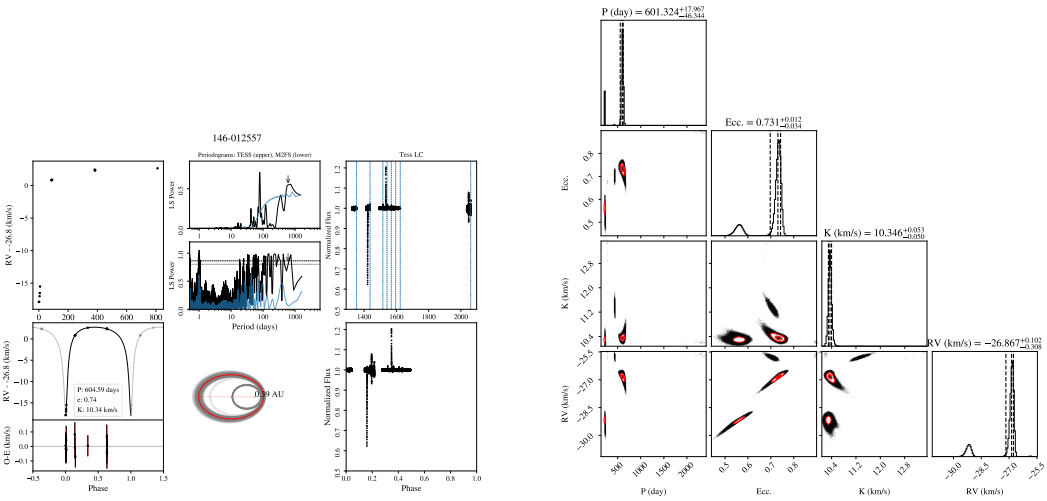

Figure A7 146-012557 (V=13.0) is a non-member in the field of NGC 2516. The primary has a T_{eff} of 5731 ± 34 K and a $v_r \sin(i)$ of 4.9 ± 0.2 km/s. This system has a period of $601.32^{+17.97}_{-46.34}$ days (e=$0.73^{+0.01}_{-0.03}$) and a semi-amplitude of 10.35 ± 0.05 km/s. The systemic RV is $-26.87^{+0.10}_{-0.31}$ km/s, $2.90^{+2.20}_{-2.22}$ km/s from the RV reported in B18. The primary mass is $0.89 M_{\odot}$ and the system's mass ratio is $0.40^{+0.19}_{-0.05}$. This system is notable for its highly elliptical orbit (~ 0.73) and well-constrained long-period without additional priors.

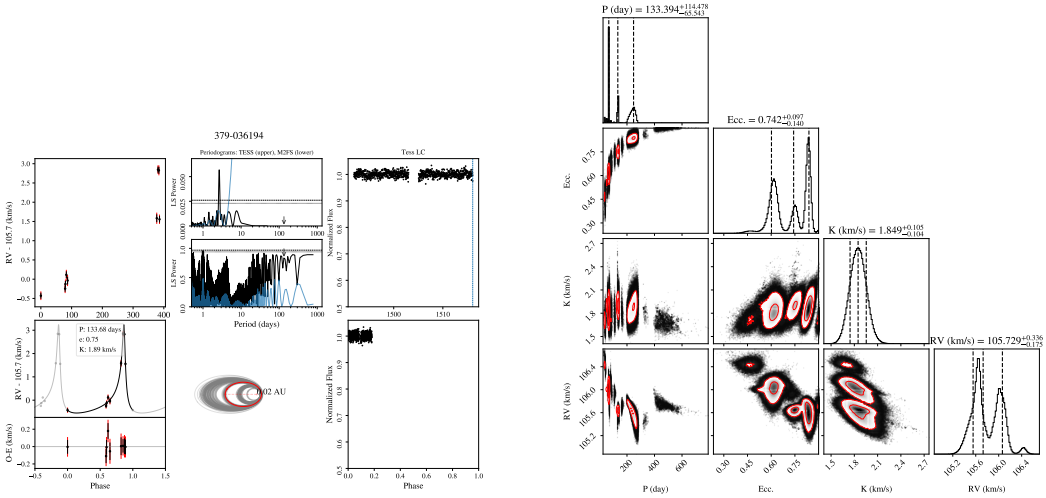

Figure A8 379-036194 (V=15.8) is a non-member in the field of NGC 2422. The primary has a T_{eff} of 5425 ± 29 K and a $v_r \sin(i)$ of 4.1 ± 0.2 km/s. This system has a period of $133.39^{+114.48}_{-65.54}$ days (e=$0.74^{+0.10}_{-0.14}$) and a semi-amplitude of 1.85 ± 0.10 km/s. The systemic RV is $105.73^{+0.34}_{-0.17}$ km/s, $-0.82^{+0.59}_{-0.52}$ km/s from the RV reported in B18. The primary mass is $0.90 M_{\odot}$ and the system's mass ratio is $0.04^{+0.02}_{-0.01}$. It is notable that the secondary has a $m_2 \sin(i)$ of 0.03 - 0.05 solar masses, indicating a possible brown dwarf.

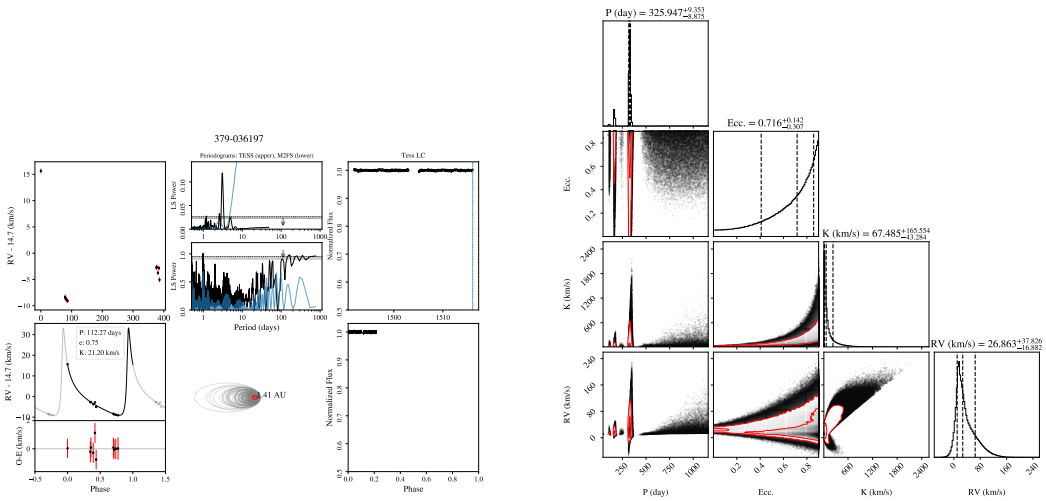

Figure A9 379-036197 (V=12.3) is a non-member in the field of NGC 2422. The primary has a T_{eff} of 6299^{+38}_{-30} K and a $v_r \sin(i)$ of 6.6 ± 0.2 km/s. This system has a period of $325.95^{+9.35}_{-8.87}$ days (e=$0.72^{+0.14}_{-0.31}$) and a semi-amplitude of $67.49^{+165.55}_{-43.28}$ km/s. The systemic RV is $26.86^{+37.83}_{-16.88}$ km/s, $15.48^{+37.91}_{-17.06}$ km/s from the RV reported in B18. The primary mass is $1.17 M_{\odot}$ and the system's mass ratio is $0.67^{+0.22}_{-0.23}$.

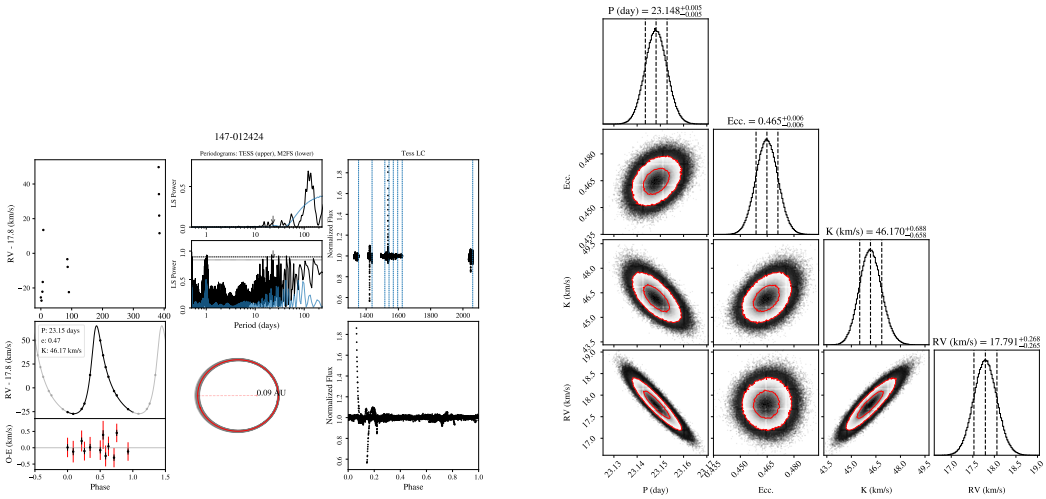

Figure A10 147-012424 (V=13.7) is a non-member in the field of NGC 2516, in contrast to B18. The primary has a T_{eff} of 6175^{+35}_{-33} K and a $v_r \sin(i)$ of 6.4±0.2 km/s. This system has a period of 23.15±0.00 days (e=0.46±0.01) and a semi-amplitude of $46.17^{+0.69}_{-0.66}$ km/s. The systemic RV is 17.79 ± 0.27 km/s, 2.34 ± 7.01 km/s from the RV reported in B18. The primary mass is $1.07 M_{\odot}$ and the system's mass ratio is $0.83^{+0.09}_{-0.04}$. B18 reported this system as an SB2 but we were unable obtain a second spectral fit and here consider it an SB1. This system is notable for its approximately equal-mass ratio (∼0.79 - 0.92).

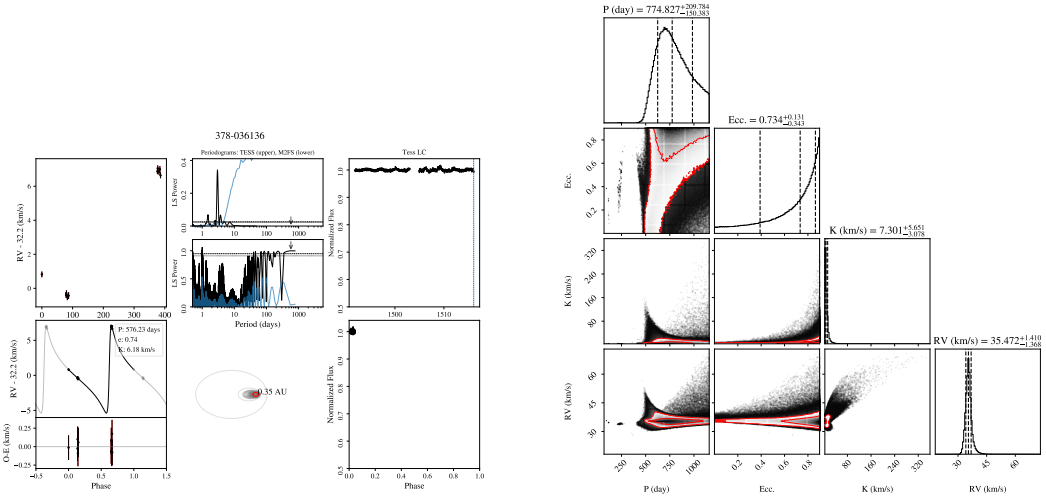

Figure A11 378-036136 (V=14.9) is a non-member in the field of NGC 2422, in contrast to B18. The primary has a T_{eff} of 5469 ± 41 K and a $v_r \sin(i)$ of 9.0 ± 0.2 km/s. We determine a 90% lower limit of 591.51 days for this system. The systemic RV is $35.47^{+1.41}_{-1.37}$ km/s, $-0.16^{+1.80}_{-1.77}$ km/s from the RV reported in B18. The primary mass is $0.92 M_{\odot}$ and the system's mass ratio is ≥ 0.20.

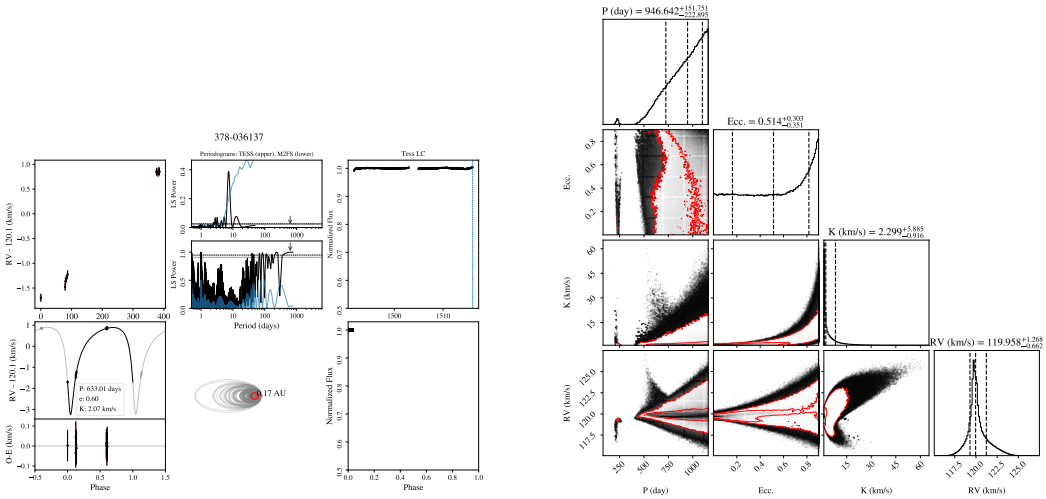

Figure A12 378-036137 (V=13.3) is a non-member in the field of NGC 2422. The primary has a T_{eff} of 5503±24 K and a $v_r \sin(i)$ of 3.0±0.2 km/s. We determine a 90% lower limit of 663.45 days for this system. The systemic RV is $119.96^{+1.27}_{-0.66}$ km/s, $-0.03^{+1.32}_{-0.76}$ km/s from the RV reported in B18. The primary mass is $0.80 M_{\odot}$ and the system's mass ratio is ≥ 0.07.

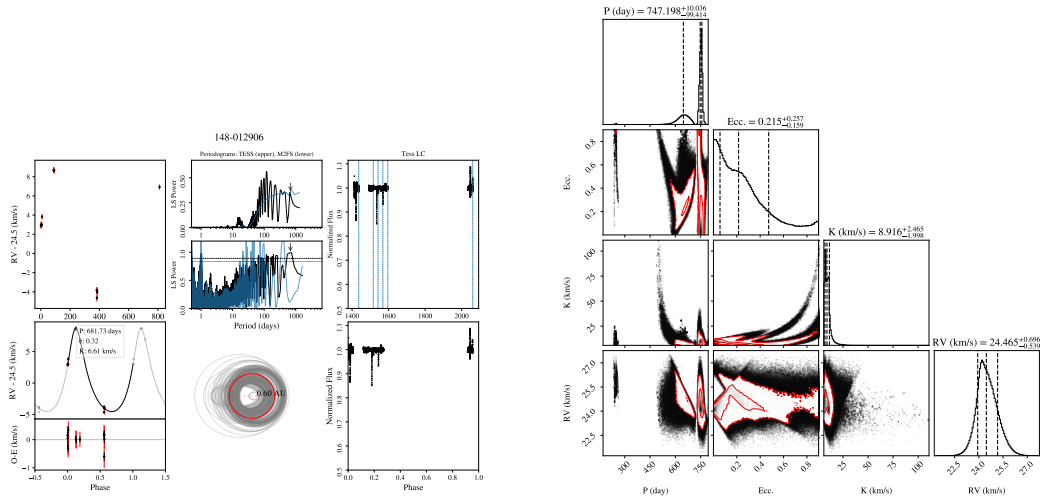

Figure A13 148-012906 (V=12.6) is a member of NGC 2516. The primary has a T_{eff} of 5516^{+22}_{-19} K and a $v_r \sin(i)$ of 15.3 ± 1.0 km/s. This system has a period of $747.20^{+10.04}_{-99.41}$ days (e=$0.22^{+0.26}_{-0.16}$) and a semi-amplitude of $8.92^{+2.46}_{-2.00}$ km/s. The systemic RV is $24.47^{+0.70}_{-0.54}$ km/s, $-2.64^{+1.54}_{-1.47}$ km/s from the RV reported in B18. The primary mass is $0.92 M_{\odot}$ and the system's mass ratio is $0.55^{+0.22}_{-0.18}$.

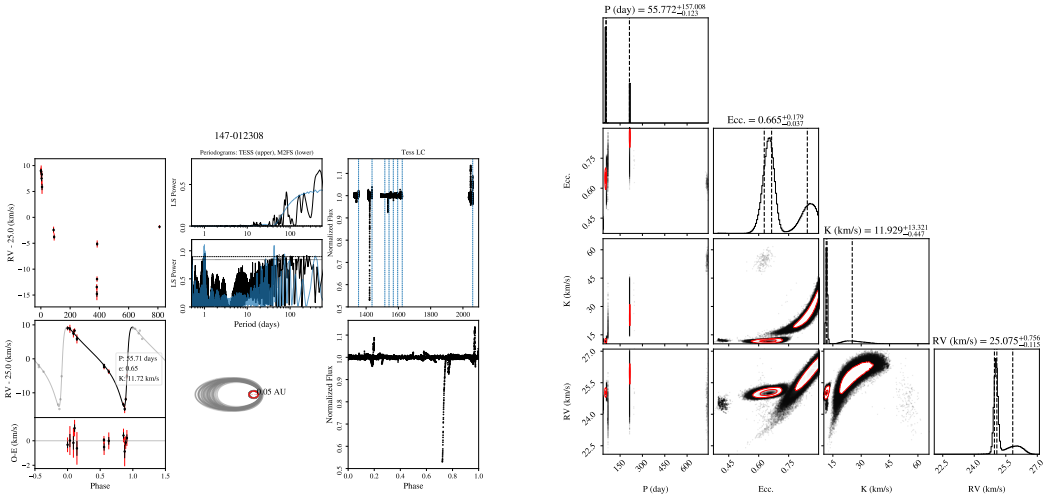

Figure A14 147-012308 (V=12.3) is a member of NGC 2516. The primary has a T_{eff} of 6658^{+49}_{-45} K and a $v_r \sin(i)$ of 37.8 ± 0.3 km/s. This system has a period of $55.77^{+157.01}_{-0.12}$ days (e=$0.66^{+0.18}_{-0.04}$) and a semi-amplitude of $11.93^{+13.32}_{-0.45}$ km/s. The systemic RV is $25.08^{+0.76}_{-0.12}$ km/s, $0.19^{+2.25}_{-2.12}$ km/s from the RV reported in B18. The primary mass is $1.24 M_{\odot}$ and the system's mass ratio is $0.23^{+0.31}_{-0.06}$.

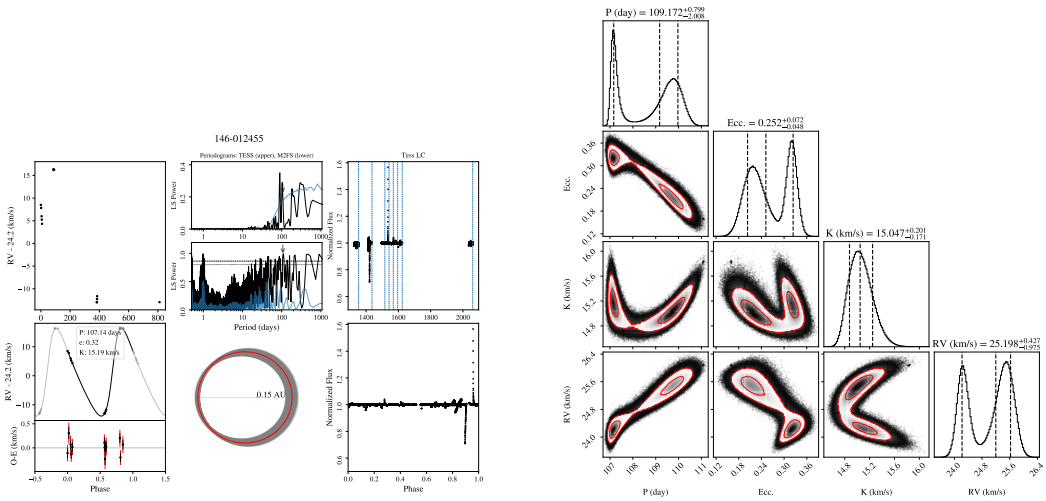

Figure A15 146-012455 (V=13.9) is a member of NGC 2516. The primary has a T_{eff} of 5308^{+21}_{-18} K and a $v_r \sin(i)$ of 7.6 ± 0.1 km/s. This system has a period of $109.17^{+0.80}_{-2.01}$ days (e=$0.25^{+0.07}_{-0.05}$) and a semi-amplitude of $15.05^{+0.20}_{-0.17}$ km/s. The systemic RV is $25.20^{+0.43}_{-0.97}$ km/s, $-0.07^{+3.78}_{-3.88}$ km/s from the RV reported in B18. The primary mass is $0.89 M_{\odot}$ and the system's mass ratio is $0.49^{+0.19}_{-0.05}$.

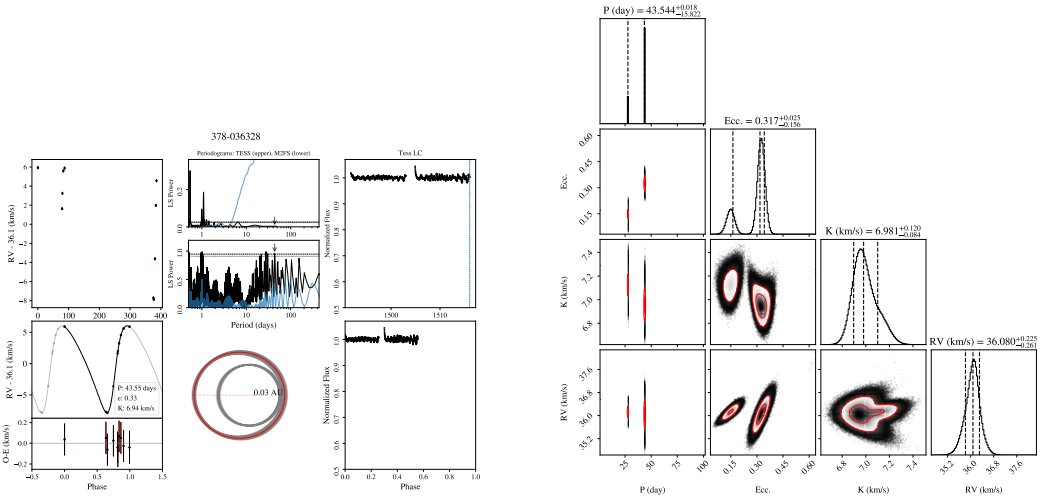

Figure A16 378-036328 (V=12.7) is a member of NGC 2422. The primary has a T_{eff} of 6222^{+38}_{-30} K and a $v_r \sin(i)$ of 7.9 ± 0.2 km/s. This system has a period of $43.54^{+0.02}_{-15.82}$ days (e=$0.32^{+0.03}_{-0.16}$) and a semi-amplitude of $6.98^{+0.12}_{-0.08}$ km/s. The systemic RV is $36.08^{+0.23}_{-0.26}$ km/s, $-0.85^{+1.57}_{-1.58}$ km/s from the RV reported in B18. The primary mass is $1.10 M_{\odot}$ and the system's mass ratio is $0.13^{+0.08}_{-0.02}$. The TESS lightcurves show a periodic modulation of the primary star's flux.

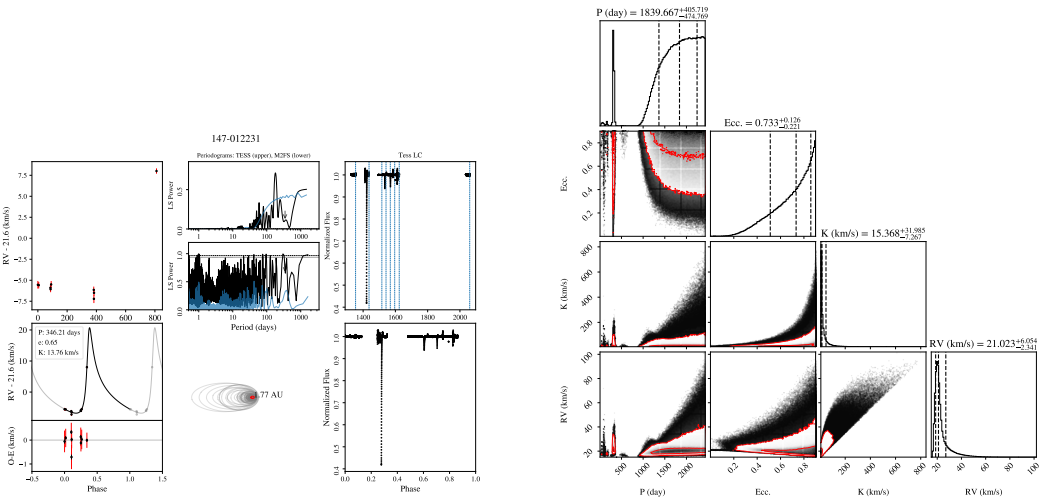

Figure A17 147-012231 (V=15.0) is a non-member in the field of NGC 2516. The primary has a T_{eff} of 5250^{+26}_{-22} K and a $v_r \sin(i)$ of 4.5 ± 0.4 km/s. We determine a 90% lower limit of 1243.58 days for this system. The systemic RV is $21.02^{+6.05}_{-2.34}$ km/s, $0.95^{+6.84}_{-3.96}$ km/s from the RV reported in B18. The primary mass is $0.92 M_{\odot}$ and the system's mass ratio is ≥ 0.38.

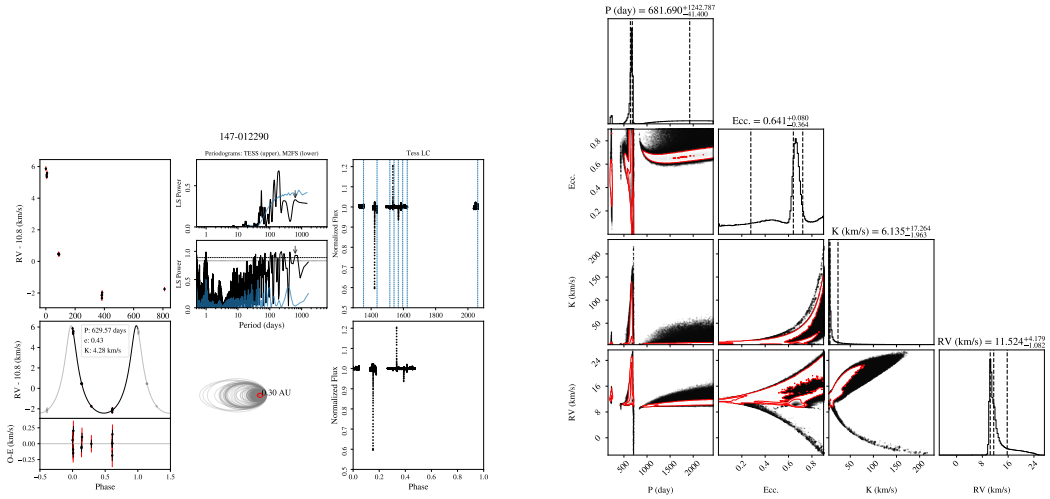

Figure A18 147-012290 (V=14.2) is a non-member in the field of NGC 2516. The primary has a T_{eff} of 5160^{+18}_{-13} K and a $v_r \sin(i)$ of 3.4 ± 0.2 km/s. We determine a 90% lower limit of 617.62 days for this system. The systemic RV is $11.52^{+4.18}_{-1.08}$ km/s, $-0.05^{+4.27}_{-1.38}$ km/s from the RV reported in B18. The primary mass is $0.88 M_{\odot}$ and the system's mass ratio is ≥ 0.19.

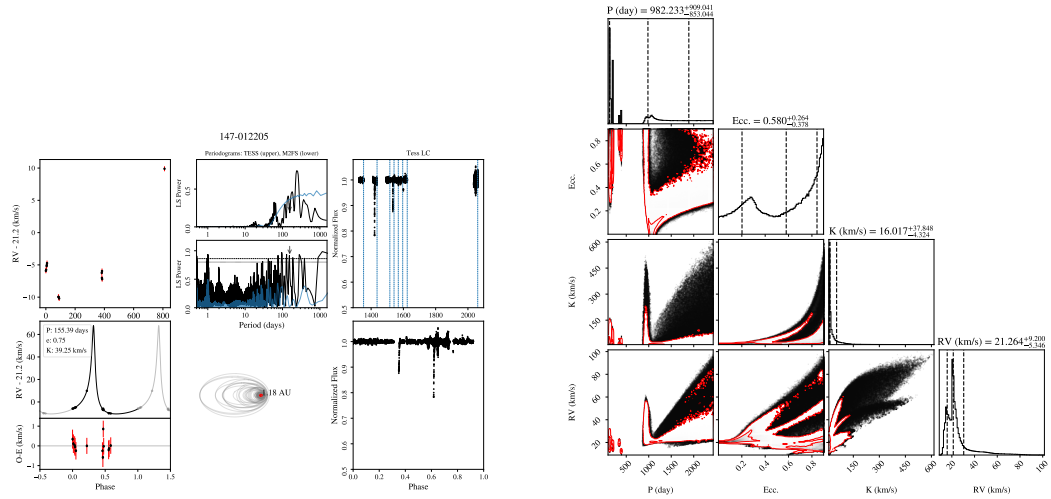

Figure A19 147-012205 (V=13.3) is a non-member in the field of NGC 2516. The primary has a T_{eff} of 5631^{+21}_{-18} K and a $v_r \sin(i)$ of 4.0 ± 0.1 km/s. We determine a 90% lower limit of 128.70 days for this system. The systemic RV is $21.26^{+9.20}_{-5.35}$ km/s, $4.73^{+9.46}_{-5.78}$ km/s from the RV reported in B18. The primary mass is $1.01 M_{\odot}$ and the system's mass ratio is ≥ 0.25.

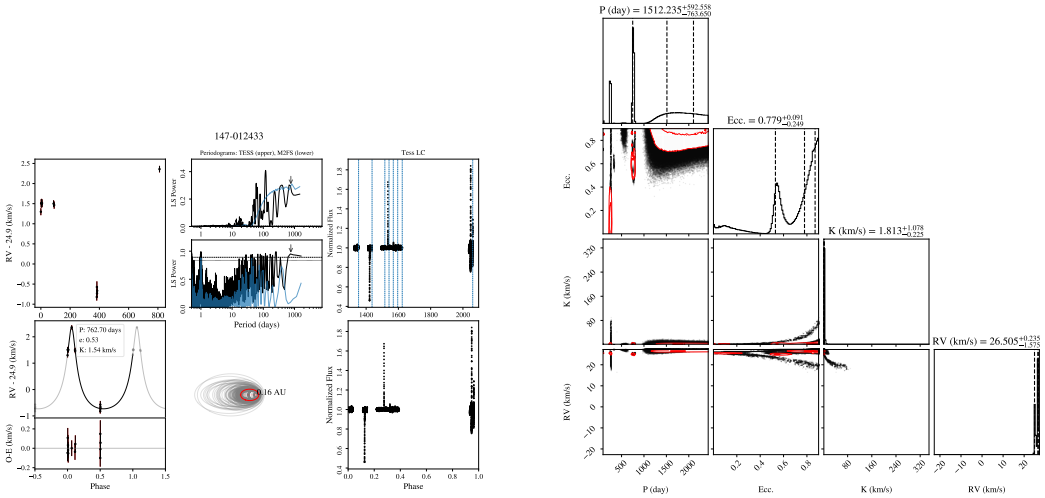

Figure A20 147-012433 (V=15.1) is a non-member in the field of NGC 2516, in contrast to B18. The primary has a T_{eff} of 5002 ± 23 K and a $v_r \sin(i)$ of 4.1 ± 0.3 km/s. We determine a 90% lower limit of 256.90 days for this system. The systemic RV is $26.51^{+0.23}_{-1.57}$ km/s, $0.47^{+0.41}_{-1.61}$ km/s from the RV reported in B18. The primary mass is $0.85 M_{\odot}$ and the system's mass ratio is ≥ 0.06. It is notable that the secondary has a $m_2 \sin(i)$ of 0.06 - 0.15 solar masses, indicating a possible brown dwarf.

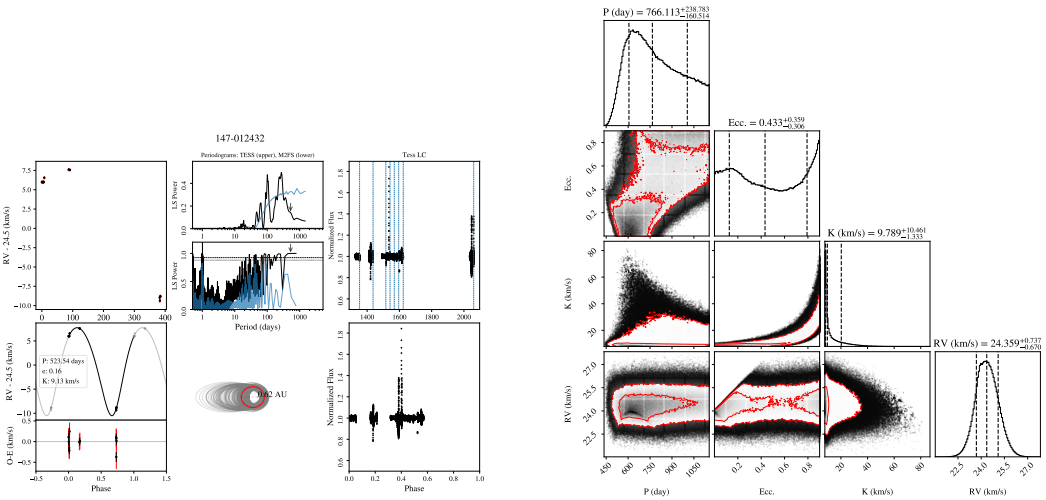

Figure A21 147-012432 (V=14.8) is a member of NGC 2516. The primary has a T_{eff} of 4898 ± 19 K and a $v_r \sin(i)$ of 5.9 ± 0.2 km/s. We determine a 90% lower limit of 576.26 days for this system. The systemic RV is $24.36^{+0.74}_{-0.67}$ km/s, $-1.82^{+2.43}_{-2.41}$ km/s from the RV reported in B18. The primary mass is $0.79 M_{\odot}$ and the system's mass ratio is ≥ 0.50. This system is notable for its near equal-mass ratio ($\sim$0.51 - 0.84).

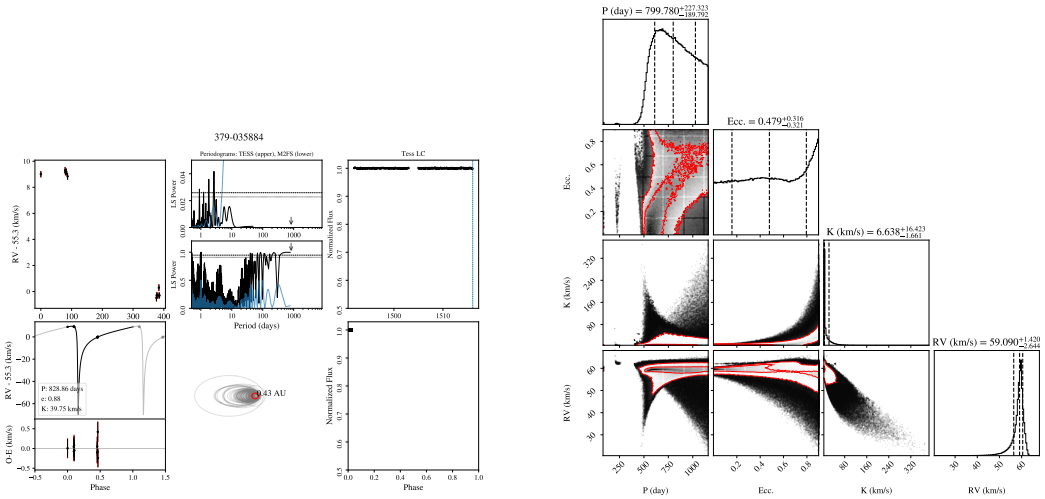

Figure A22 379-035884 (V=12.5) is a non-member in the field of NGC 2422. The primary has a T_{eff} of 6846^{+52}_{-40} K and a $v_r \sin(i)$ of 19.0 ± 0.3 km/s. We determine a 90% lower limit of 574.15 days for this system. The systemic RV is $59.09^{+1.42}_{-2.64}$ km/s, $-0.58^{+2.04}_{-3.02}$ km/s from the RV reported in B18. The primary mass is $1.30 M_{\odot}$ and the system's mass ratio is ≥ 0.22.

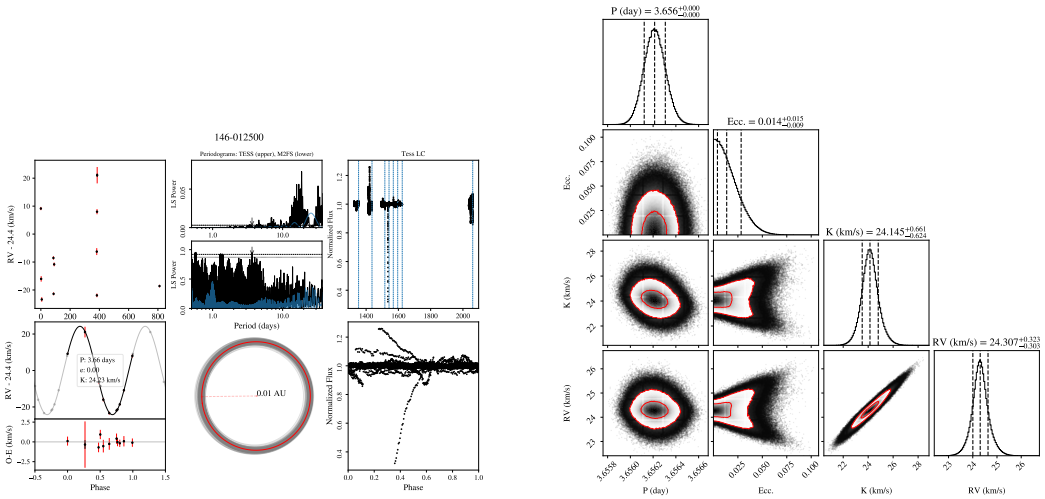

Figure A23 146-012500 (V=14.8) is a member of NGC 2516. The primary has a T_{eff} of 4877 ± 30 K and a $v_r \sin(i)$ of 8.8 ± 0.2 km/s. This system has a period of 3.66 ± 0.00 days (e=0.01 ± 0.01) and a semi-amplitude of $24.15^{+0.66}_{-0.62}$ km/s. The systemic RV is $24.31^{+0.32}_{-0.30}$ km/s, 11.00 ± 4.34 km/s from the RV reported in B18. The primary mass is $0.80 M_{\odot}$ and the system's mass ratio is $0.25^{+0.14}_{-0.03}$.

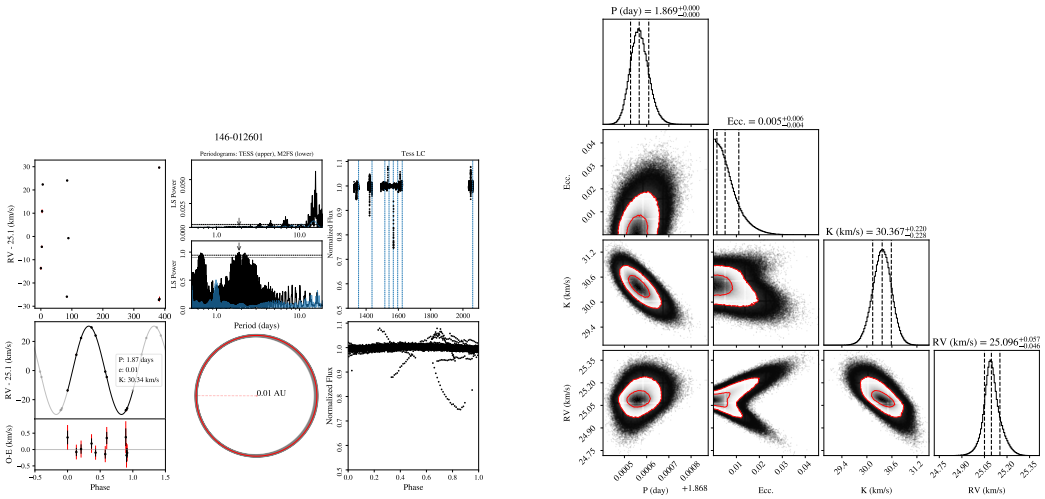

Figure A24 146-012601 (V=13.9) is a member of NGC 2516. The primary has a T_{eff} of 5116 ± 19 K and a $v_r \sin(i)$ of 16.1 ± 0.2 km/s. This system has a period of 1.87 ± 0.00 days (e=$0.01^{+0.01}_{-0.00}$) and a semi-amplitude of $30.37^{+0.22}_{-0.23}$ km/s. The systemic RV is $25.10^{+0.06}_{-0.05}$ km/s, -6.06 ± 6.20 km/s from the RV reported in B18. The primary mass is $0.82 M_{\odot}$ and the system's mass ratio is $0.25^{+0.14}_{-0.03}$. The phase-folded TESS lightcurve is suggestive of tidal ellipsoidal distortion.

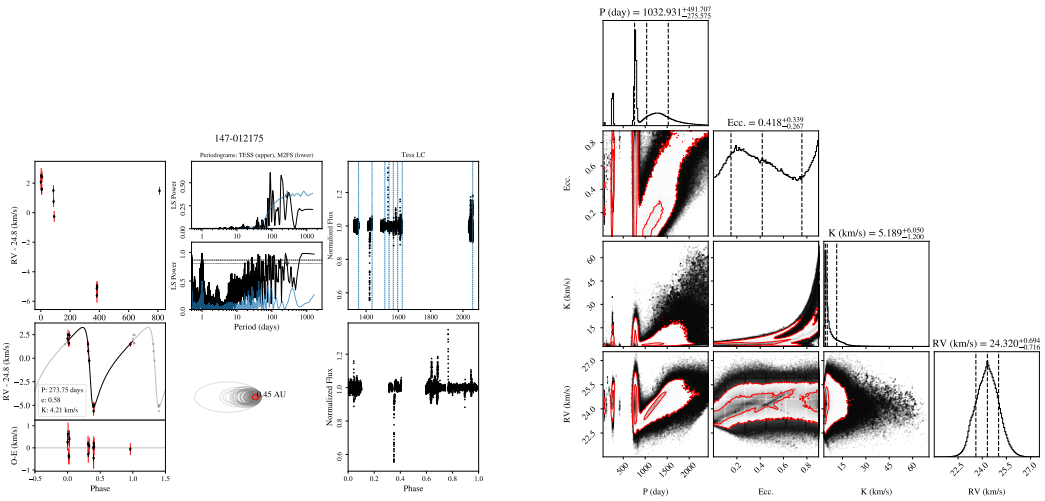

Figure A25 147-012175 (V=14.9) is a member of NGC 2516. The primary has a T_{eff} of 4752^{+17}_{-13} K and a $v_r \sin(i)$ of 10.8 ± 0.2 km/s. This system has a period of $1032.93^{+491.71}_{-275.57}$ days (e=$0.42^{+0.34}_{-0.27}$) and a semi-amplitude of $5.19^{+6.05}_{-1.20}$ km/s. The systemic RV is $24.32^{+0.69}_{-0.72}$ km/s, $-0.03^{+1.16}_{-1.17}$ km/s from the RV reported in B18. The primary mass is $0.78 M_{\odot}$ and the system's mass ratio is $0.35^{+0.24}_{-0.12}$.

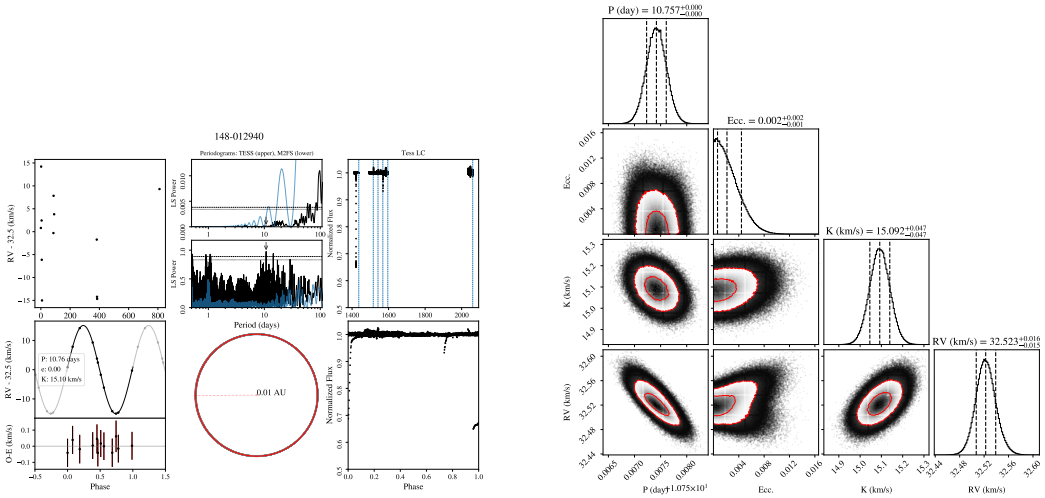

Figure A26 148-012940 (V=12.0) is a non-member in the field of NGC 2516, in contrast to B18. The primary has a T_{eff} of 6064^{+22}_{-19} K and a $v_r \sin(i)$ of 6.0±0.1 km/s. This system has a period of 10.76±0.00 days (e=0.00±0.00) and a semi-amplitude of 15.09±0.05 km/s. The systemic RV is 32.52 ± 0.02 km/s, 0.43 ± 2.44 km/s from the RV reported in B18. The primary mass is $1.13 M_{\odot}$ and the system's mass ratio is $0.19^{+0.12}_{-0.02}$.

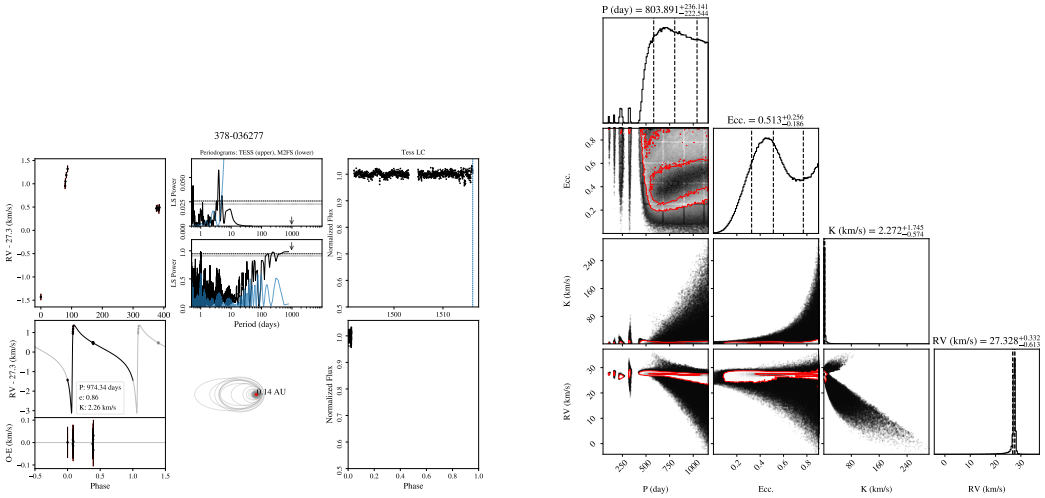

Figure A27 378-036277 (V=14.4) is a non-member in the field of NGC 2422. The primary has a T_{eff} of 5382^{+23}_{-20} K and a $v_r \sin(i)$ of 3.4 ± 0.1 km/s. We determine a 90% lower limit of 537.19 days for this system. The systemic RV is $27.33^{+0.33}_{-0.61}$ km/s, $-0.49^{+0.40}_{-0.65}$ km/s from the RV reported in B18. The primary mass is $0.92 M_{\odot}$ and the system's mass ratio is ≥ 0.06. The TESS lightcurves show a periodic modulation of the primary star's flux. It is notable that the secondary has a $m_2 \sin(i)$ of 0.06 - 0.21 solar masses, indicating a possible brown dwarf.

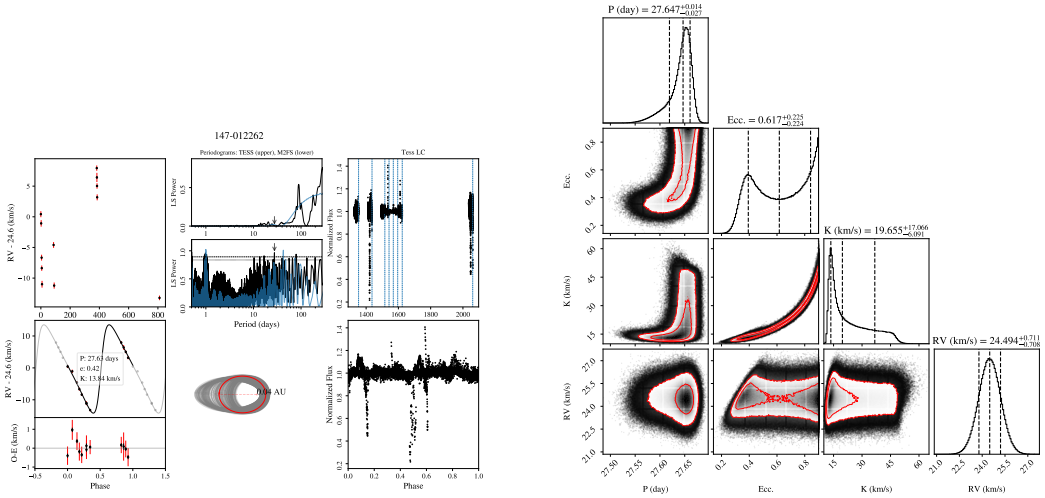

Figure A28 147-012262 (V=14.8) is a member of NGC 2516. The primary has a T_{eff} of 4821 ± 19 K and a $v_r \sin(i)$ of 4.6 ± 0.3 km/s. This system has a period of $27.65^{+0.01}_{-0.03}$ days (e=$0.62^{+0.23}_{-0.22}$) and a semi-amplitude of $19.66^{+17.07}_{-6.09}$ km/s. The systemic RV is 24.49 ± 0.71 km/s, 4.76 ± 2.86 km/s from the RV reported in B18. The primary mass is $0.76 M_{\odot}$ and the system's mass ratio is $0.36^{+0.17}_{-0.11}$.

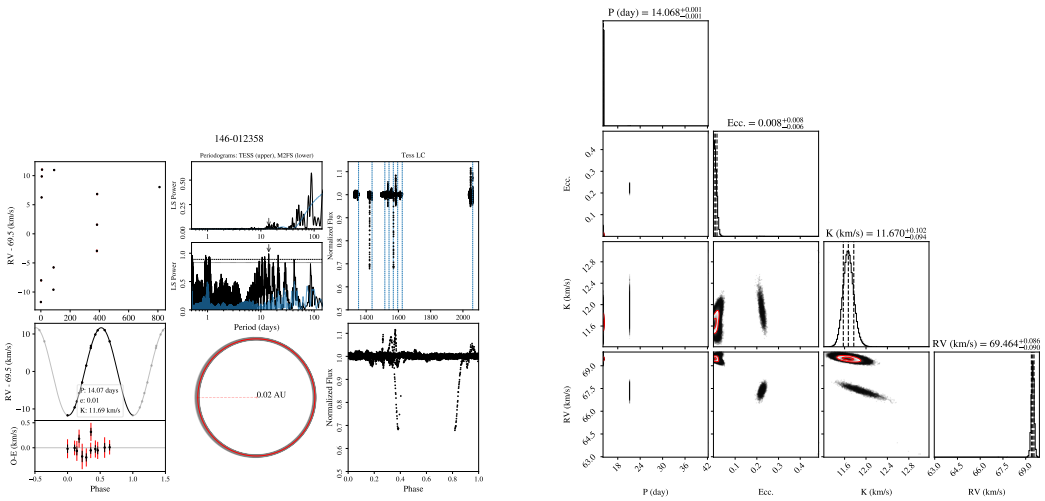

Figure A29 146-012358 (V=15.1) is a non-member in the field of NGC 2516. The primary has a T_{eff} of 4833 ± 18 K and a $v_r \sin(i)$ of 4.5 ± 0.2 km/s. This system has a period of 14.07 ± 0.00 days (e=0.01 ± 0.01) and a semi-amplitude of $11.67^{+0.10}_{-0.09}$ km/s. The systemic RV is 69.46 ± 0.09 km/s, -1.88 ± 2.92 km/s from the RV reported in B18. The primary mass is $0.81 M_{\odot}$ and the system's mass ratio is $0.18^{+0.11}_{-0.02}$.

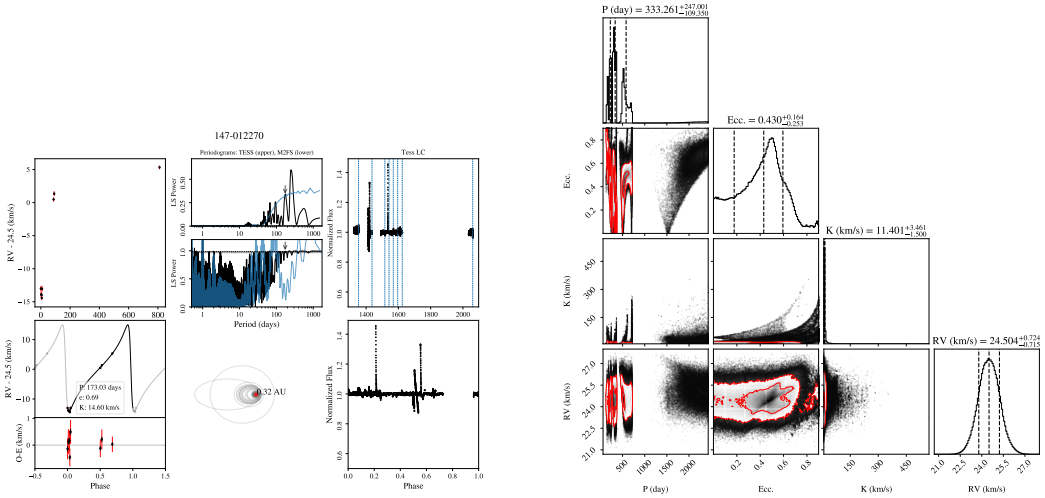

Figure A30 147-012270 (V=14.0) is a member of NGC 2516, in contrast to B18. The primary has a T_{eff} of 5117 ± 60 K and a $v_r \sin(i)$ of 7.5 ± 0.6 km/s. This system has a period of $333.26^{+247.00}_{-109.35}$ days (e=$0.43^{+0.16}_{-0.25}$) and a semi-amplitude of $11.40^{+3.46}_{-1.50}$ km/s. The systemic RV is $24.50^{+0.72}_{-0.71}$ km/s, $4.35^{+3.70}_{-3.69}$ km/s from the RV reported in B18. The primary mass is $0.81 M_{\odot}$ and the system's mass ratio is $0.57^{+0.21}_{-0.16}$.

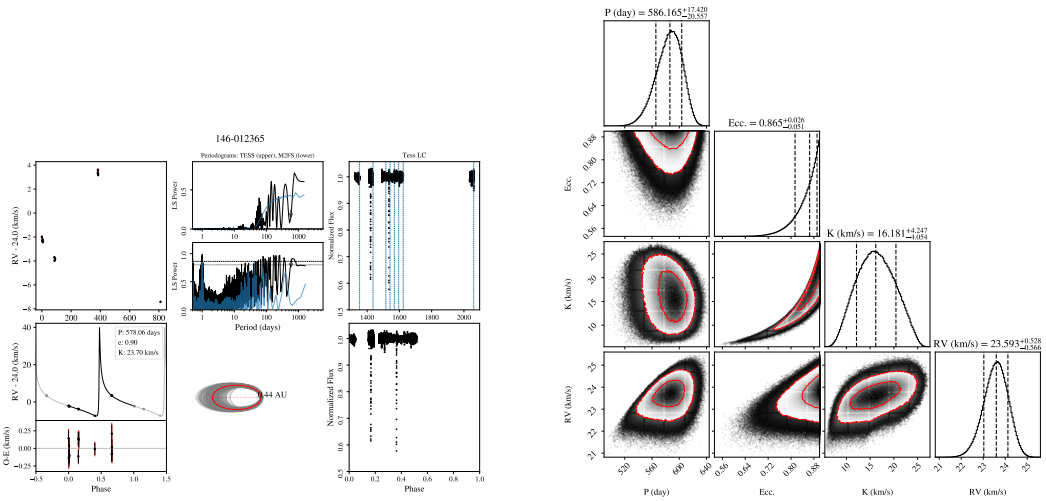

Figure A31 146-012365 (V=13.4) is a member of NGC 2516. The primary has a T_{eff} of 5774^{+21}_{-18} K and a $v_r \sin(i)$ of 6.3 ± 0.1 km/s. This system has a period of $586.17^{+17.42}_{-20.56}$ days (e=$0.87^{+0.03}_{-0.05}$) and a semi-amplitude of $16.18^{+4.25}_{-4.05}$ km/s. The systemic RV is $23.59^{+0.53}_{-0.57}$ km/s, $1.84^{+1.28}_{-1.29}$ km/s from the RV reported in B18. The primary mass is $1.04 M_{\odot}$ and the system's mass ratio is $0.47^{+0.18}_{-0.11}$.

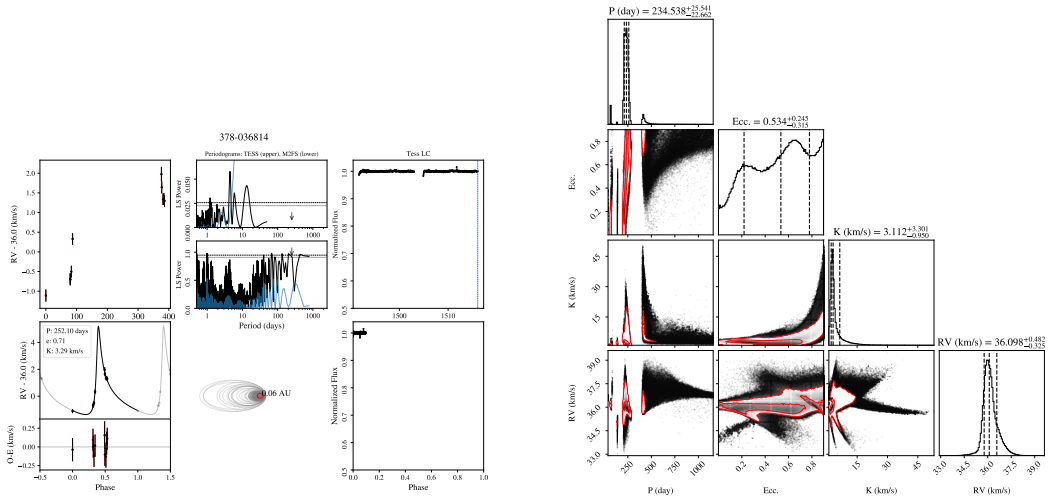

Figure A32 378-036814 (V=14.5) is a member of NGC 2422. The primary has a T_{eff} of 5098^{+19}_{-15} K and a $v_r \sin(i)$ of 6.9 ± 0.2 km/s. This system has a period of $234.54^{+25.54}_{-22.66}$ days (e=$0.53^{+0.24}_{-0.32}$) and a semi-amplitude of $3.11^{+3.30}_{-0.95}$ km/s. The systemic RV is $36.10^{+0.48}_{-0.33}$ km/s, $-0.22^{+0.59}_{-0.47}$ km/s from the RV reported in B18. The primary mass is $0.86 M_{\odot}$ and the system's mass ratio is $0.11^{+0.12}_{-0.04}$.

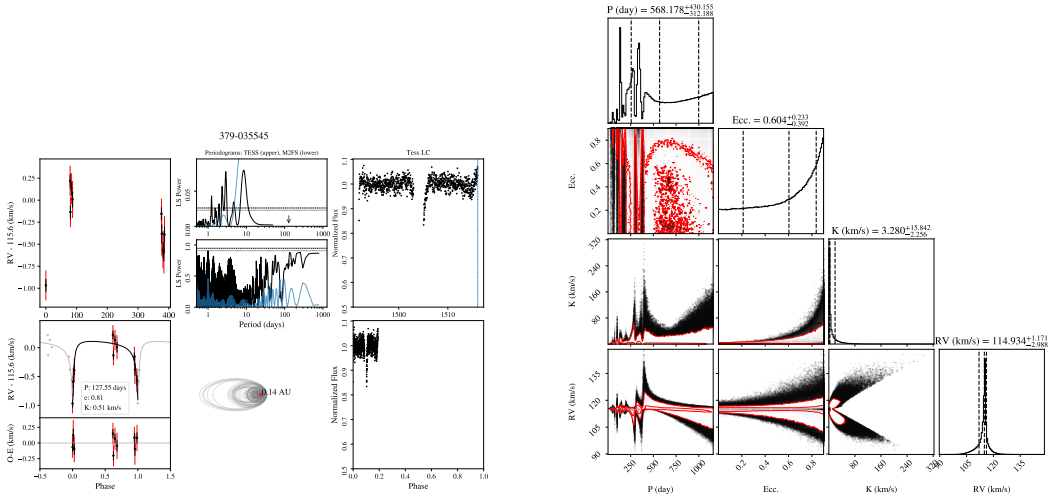

Figure A33 379-035545 (V=15.9) is a non-member in the field of NGC 2422. The primary has a T_{eff} of 4980^{+19}_{-14} K and a $v_r \sin(i)$ of 4.3 ± 0.2 km/s. We determine a 90% lower limit of 208.73 days for this system. The systemic RV is $114.93^{+1.17}_{-2.99}$ km/s, $-0.40^{+1.18}_{-2.99}$ km/s from the RV reported in B18. The primary mass is $0.81 M_{\odot}$ and the system's mass ratio is ≥ 0.02.

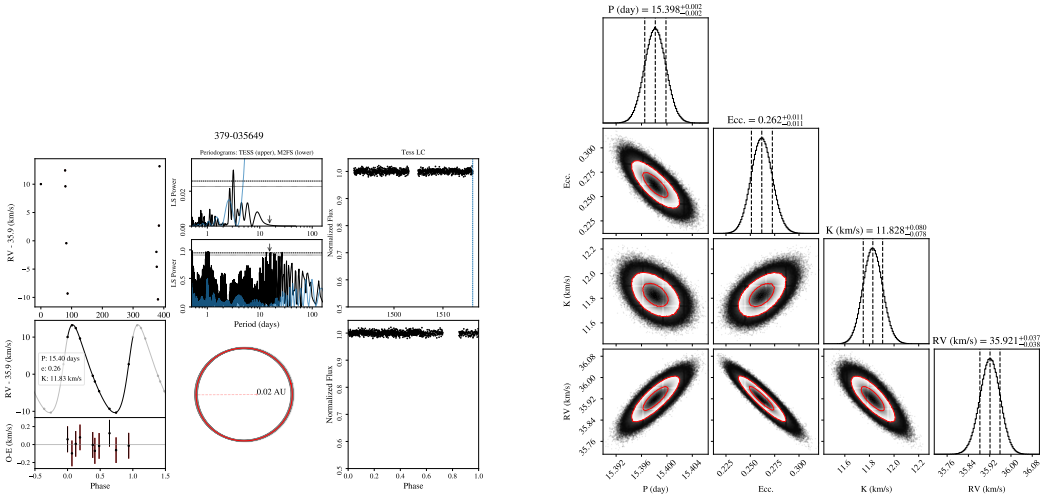

Figure A34 379-035649 (V=13.7) is a member of NGC 2422. The primary has a T_{eff} of 5533^{+23}_{-21} K and a $v_r \sin(i)$ of 4.4 ± 0.1 km/s. This system has a period of 15.40 ± 0.00 days (e=0.26 ± 0.01) and a semi-amplitude of 11.83 ± 0.08 km/s. The systemic RV is 35.92 ± 0.04 km/s, -2.74 ± 2.69 km/s from the RV reported in B18. The primary mass is $0.97 M_{\odot}$ and the system's mass ratio is $0.17^{+0.11}_{-0.02}$.

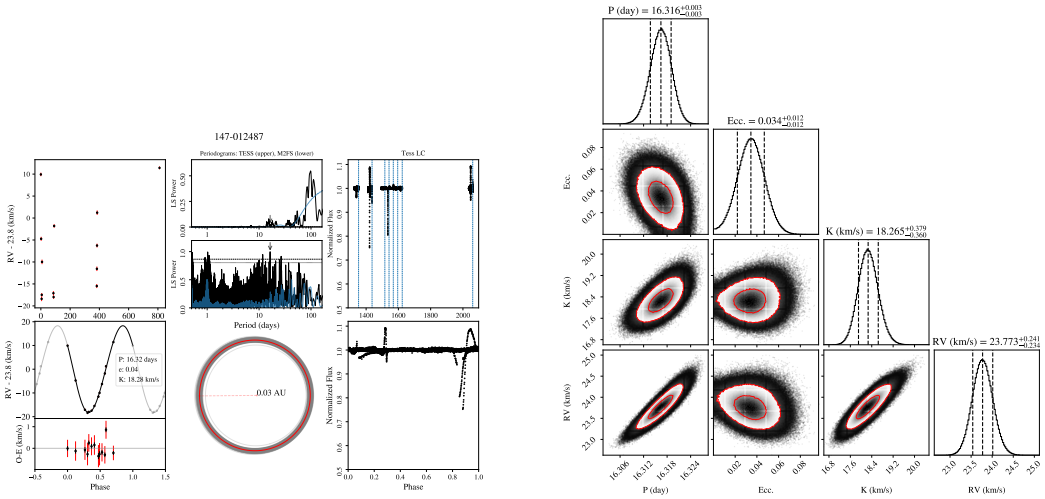

Figure A35 147-012487 (V=12.4) is a member of NGC 2516, in contrast to B18. The primary has a T_{eff} of 6408^{+35}_{-28} K and a $v_r \sin(i)$ of $10.4^{+0.2}_{-0.1}$ km/s. This system has a period of 16.32 ± 0.00 days (e=0.03 ± 0.01) and a semi-amplitude of $18.27^{+0.38}_{-0.36}$ km/s. The systemic RV is $23.77^{+0.24}_{-0.23}$ km/s, 5.14 ± 3.57 km/s from the RV reported in B18. The primary mass is $1.18 M_{\odot}$ and the system's mass ratio is $0.28^{+0.16}_{-0.03}$.

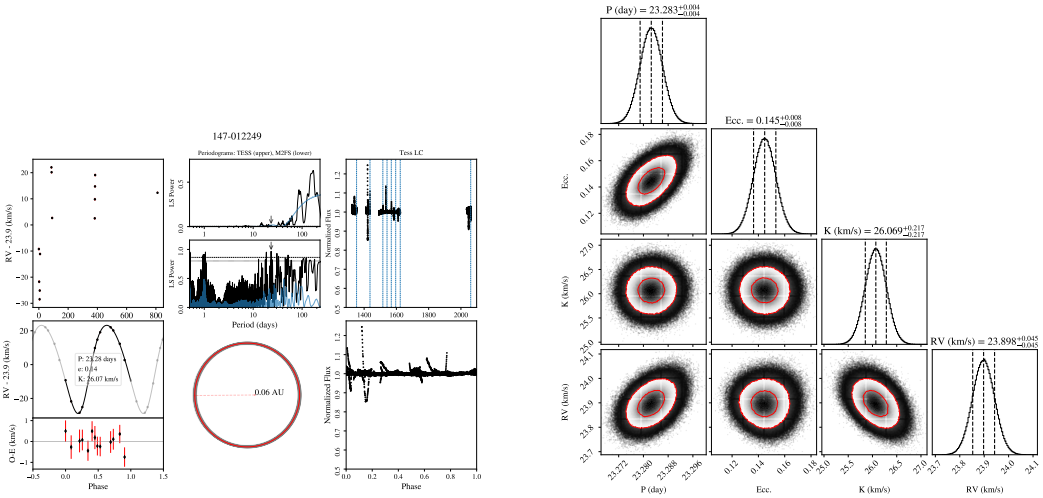

Figure A36 147-012249 (V=14.0) is a member of NGC 2516. The primary has a T_{eff} of 5250^{+17}_{-13} K and a $v_r \sin(i)$ of 6.7 ± 0.1 km/s. This system has a period of 23.28 ± 0.00 days (e=0.14 ± 0.01) and a semi-amplitude of 26.07 ± 0.22 km/s. The systemic RV is $23.90^{+0.05}_{-0.04}$ km/s, -3.63 ± 4.24 km/s from the RV reported in B18. The primary mass is $0.89 M_{\odot}$ and the system's mass ratio is $0.52^{+0.19}_{-0.05}$.

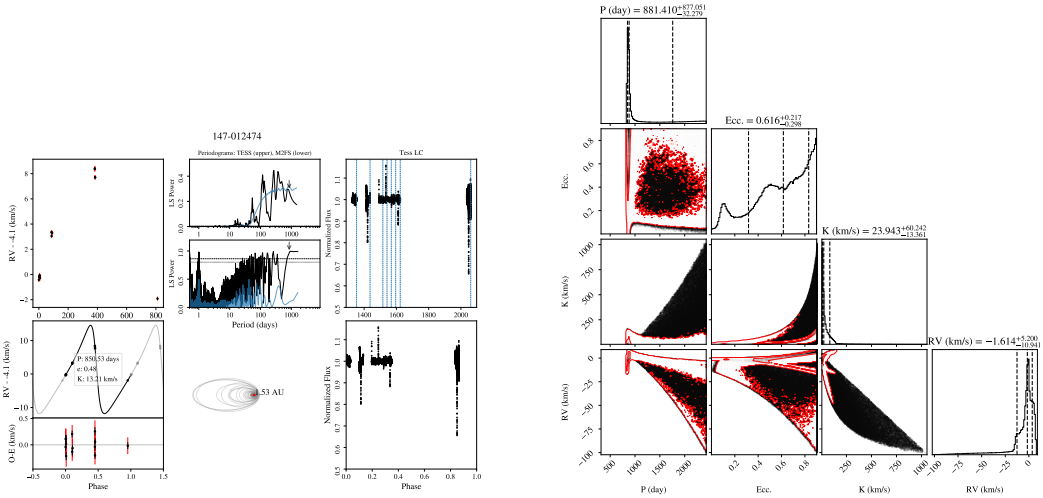

Figure A37 147-012474 (V=14.4) is a non-member in the field of NGC 2516. The primary has a T_{eff} of 5111 ± 20 K and a $v_r \sin(i)$ of 3.7 ± 0.1 km/s. We determine a 90% lower limit of 844.99 days for this system. The systemic RV is $-1.61^{+5.20}_{-10.94}$ km/s, $-0.03^{+5.34}_{-11.01}$ km/s from the RV reported in B18. The primary mass is $0.86 M_{\odot}$ and the system's mass ratio is ≥ 0.41. This system is notable for its approximately equal-mass ratio (0.46 - 0.90).

Bibliography

Aime, C., & Soummer, R. 2004, The Astrophysical Journal, 612, L85, doi: 10.1086/424381

Astropy Collaboration, Robitaille, T. P., Tollerud, E. J., et al. 2013, , 558, A33, doi: 10.1051/0004-6361/201322068

Astropy Collaboration, Price-Whelan, A. M., SipHocz, B. M., et al. 2018, aj, 156, 123, doi: 10.3847/1538-3881/aabc4f

Badenes, C., Mazzola, C., Thompson, T. A., et al. 2018, , 854, 147, doi: 10.3847/1538-4357/aaa765

Bailey, J. I., Mateo, M., White, R. J., Shectman, S. A., & Crane, J. D. 2018, , 475, 1609, doi: 10.1093/mnras/stx3266

Bailey, J. I., Mateo, M., White, R. J., et al. 2016, The Astronomical Journal, 152, 9, doi: 10.3847/0004-6256/152/1/9

Barman, T. S., Konopacky, Q. M., Macintosh, B., & Marois, C. 2015, Astrophysical Journal Supplement Series, 804

Beuzit, J.-L., Vigan, A., Mouillet, D., et al. 2019, Astronomy & Astrophysics, 631, A155

Binney, J., & Tremaine, S. 2008, Galactic Dynamics: Second Edition

Bottom, M., Femenia, B., Huby, E., et al. 2016a, SPIE, 9909, 9909

Bottom, M., Femenia, B., Huby, E., et al. 2016b, in Proceedings of the SPIE, California Institute of Technology (United States) (International Society for Optics and Photonics), 990955

Bottom, M., Shelton, J. C., Wallace, J. K., et al. 2016, , 128, 075003, doi: 10.1088/1538-3873/128/965/075003

Bouchez, A. H., Dekany, R. G., Roberts, J. E., et al. 2010, in Society of Photo-Optical Instrumentation Engineers (SPIE) Conference Series

Bowler, B. P. 2016, PASP, 128, 102001

Cantat-Gaudin, T., Jordi, C., Vallenari, A., et al. 2018, , 618, A93, doi: 10.1051/0004-6361/201833476

Carbillet, M., Bendjoya, P., Abe, L., et al. 2011, Experimental Astronomy, 30, 39, doi: 10.1007/s10686-011-9219-4

Close, L. M., Males, J. R., Morzinski, K., et al. 2013, ApJ, 774, 94

Crepp, J. R., Pueyo, L., Brenner, D., et al. 2011, ApJ, 729, 132

Currie, T., Burrows, A., Itoh, Y., et al. 2011, , 729, 128, doi: 10.1088/0004-637X/729/2/128

Cutri, R., Skrutskie, M., Van Dyk, S., et al. 2003, tmc

Day, P., Leduc, H., A Mazin, B., Vayonakis, A., & Zmuidzinas, J. 2003, Nature, 425, 817, doi: 10.1038/nature02037

Deacon, N. R., & Kraus, A. L. 2020, , 496, 5176, doi: 10.1093/mnras/staa1877

Dekany, R., Bouchez, A., Britton, M., et al. 2006, in Society of Photo-Optical Instrumentation Engineers (SPIE) Conference Series

Dodkins, R. H., Davis, K. K., Lewis, B., et al. 2020, Publications of the Astronomical Society of the Pacific, 132, 104503

Donor, J., Frinchaboy, P. M., Cunha, K., et al. 2020, The Astronomical Journal, 159, 199, doi: 10.3847/1538-3881/ab77bc

Duchêne, G., & Kraus, A. 2013, , 51, 269, doi: 10.1146/annurev-astro-081710-102602

Feinstein, A. D., Montet, B. T., Foreman-Mackey, D., et al. 2019, Publications of the Astronomical Society of the Pacific, 131, 094502, doi: 10.1088/1538-3873/ab291c

Fitzgerald, M. P., & Graham, J. R. 2006, ApJ, 637, 541

Fontanive, C., Rice, K., Bonavita, M., et al. 2019, Monthly Notices of the Royal Astronomical Society, 485, 4967, doi: 10.1093/mnras/stz671

Foreman-Mackey, D., Hogg, D. W., Lang, D., & Goodman, J. 2013, , 125, 306, doi: 10.1086/670067

Frazin, R. A. 2016, Journal of the Optical Society of America A, 33, 712

—. 2018, Journal of the Optical Society of America A, 35, 594

Fritzewski, D. J., Barnes, S. A., James, D. J., & Strassmeier, K. G. 2020, , 641, A51, doi: 10.1051/0004-6361/201936860

Fruitwala, N., Strader, P., Cancelo, G., et al. 2020, Review of Scientific Instruments, 91, 124705, doi: 10.1063/5.0029457

Gaia Collaboration, Brown, A. G. A., Vallenari, A., et al. 2020, Gaia Early Data Release 3: Summary of the contents and survey properties. https://arxiv.org/abs/2012.01533

Gaia Collaboration, Prusti, T., de Bruijne, J. H. J., et al. 2016, , 595, A1, doi: 10.1051/0004-6361/201629272

Gaia Collaboration, Babusiaux, C., van Leeuwen, F., et al. 2018, , 616, A10, doi: 10.1051/0004-6361/201832843

Geller, A. 2013, European Astronomical Society Publications Series, 64, 317–320, doi: 10.1051/eas/1364044

Geller, A., Hurley, J., & Mathieu, R. 2012, The Astronomical Journal, 145, doi: 10.1088/0004-6256/145/1/8

Geller, A. M., de Grijs, R., Li, C., & Hurley, J. R. 2015, , 805, 11, doi: 10.1088/0004-637X/805/1/11

Geller, A. M., Mathieu, R. D., Latham, D. W., et al. 2021, arXiv e-prints, arXiv:2101.07883. https://arxiv.org/abs/2101.07883

Gerard, B. L., Marois, C., Currie, T., et al. 2019, ApJ, 158, 36

Gladysz, S., & Christou, J. C. 2008, ApJ, 684, 1486

Gomez Gonzalez, C. A., Absil, O., Absil, P.-A., et al. 2016, A&A, 589, A54

Goodwin, S. 2010, Philosophical transactions. Series A, Mathematical, physical, and engineering sciences, 368, 851, doi: 10.1098/rsta.2009.0254

Grether, D., & Lineweaver, C. H. 2006, The Astrophysical Journal, 640, 1051, doi: 10.1086/500161

Griffin, R. F. 2012, Journal of Astrophysics and Astronomy, 33, 29, doi: 10.1007/s12036-012-9137-5

Griffiths, D. W., Goodwin, S. P., & Caballero-Nieves, S. M. 2018, , 476, 2493, doi: 10.1093/mnras/sty412

Guerrero, C. A., Orlov, V. G., Monroy-Rodríguez, M. A., & Borges Fernandes, M. 2015, , 150, 16, doi: 10.1088/0004-6256/150/1/16

Guyon, O. 2005, ApJ, 629, 592

Hodapp, K. W., Suzuki, R., Tamura, M., et al. 2008, in Ground-based and Airborne Instrumentation for Astronomy II, Vol. 7014, International Society for Optics and Photonics, 701419

Husser, T.-O., Wende-von Berg, S., Dreizler, S., et al. 2013, Astronomy & Astrophysics, 553, A6

Jeffries, R. D., Thurston, M. R., & Hambly, N. C. 2001, , 375, 863, doi: 10.1051/0004-6361:20010918

Jovanovic, N., Martinache, F., Guyon, O., et al. 2015, PASP, 127, 890

Jovanovic, N., Delorme, J.-R., Bond, C. Z., et al. 2019, arXiv preprint arXiv:1909.04541

Kharchenko, N. V., Piskunov, A. E., Röser, S., Schilbach, E., & Scholz, R. D. 2005, , 438, 1163, doi: 10.1051/0004-6361:20042523

Kharchenko, N. V., Piskunov, A. E., Röser, S., et al. 2009, , 504, 681, doi: 10.1051/0004-6361/200911979

Kharchenko, N. V., Piskunov, A. E., Schilbach, E., Röser, S., & Scholz, R. D. 2013, , 558, A53, doi: 10.1051/0004-6361/201322302

Konopacky, Q. M., Barman, T. S., Macintosh, B. A., & Marois, C. 2013, Science, 339, 1398, doi: 10.1126/science.1232003

Kounkel, M., Hartmann, L., Tobin, J. J., et al. 2016, , 821, 8, doi: 10.3847/0004-637X/821/1/8

Kounkel, M., Covey, K., Moe, M., et al. 2019, The Astronomical Journal, 157, 196, doi: 10.3847/1538-3881/ab13b1

Kuzuhara, M., Tamura, M., Kudo, T., et al. 2013, ApJ, 774, 11

Lafrenière, D., Marois, C., Doyon, R., Nadeau, D., & Artigau, É. 2007, ApJ, 660, 770

Lafrenière, D., Marois, C., Doyon, R., & Barman, T. 2009, The Astrophysical Journal, 694, L148–L152, doi: 10.1088/0004-637x/694/2/l148

Lagrange, A. M., Bonnefoy, M., Chauvin, G., et al. 2010, Science, 329, 57

Lewis, B., & Oppenheimer, R. 2017, Columbia Undergraduate Science Journal, 11

Lindegren, L., Klioner, S. A., Hernández, J., et al. 2020, arXiv e-prints, arXiv:2012.03380. https://arxiv.org/abs/2012.03380

Loktin, A. V., Gerasimenko, T. P., & Malysheva, L. K. 2001, Astronomical and Astrophysical Transactions, 20, 607, doi: 10.1080/10556790108221134

Lozi, J., Guyon, O., Jovanovic, N., et al. 2018, Journal of Astronomical Telescopes, Instruments, and Systems, 4, 1

Lucatello, S., Sollima, A., Gratton, R., et al. 2015, , 584, A52, doi: 10.1051/0004-6361/201526957

Macintosh, B., Graham, J. R., Ingraham, P., et al. 2014, Proceedings of the National Academy of Sciences, 111, 12661, doi: 10.1073/pnas.1304215111

Macintosh, B., Graham, J. R., Barman, T., et al. 2015a, Science, 350, 64

—. 2015b, Science, 350, 64, doi: 10.1126/science.aac5891

Macintosh, B. A., Grahamand, J. R., Palmer, D. W., et al. 2008, SPIE, 7015, 7015

Males, J. R., & Guyon, O. 2018, Journal of Astronomical Telescopes, 4, 019001

Males, J. R., Close, L. M., Miller, K., et al. 2018, SPIE, 10703

Marcy, G. W., & Butler, R. P. 2000, , 112, 137, doi: 10.1086/316516

Marois, C., Correia, C., Galicher, R., et al. 2014, in SPIE, Vol. 9148, Adaptive Optics Systems IV, 91480U

Marois, C., Doyon, R., Racine, R., & Nadeau, D. 2000, PASP, 112, 91

Marois, C., Lafrenière, D., Doyon, R., Macintosh, B., & Nadeau, D. 2006a, , 641, 556, doi: 10.1086/500401

—. 2006b, ApJ, 641, 556

Marois, C., Macintosh, B., Barman, T., et al. 2008, Science, 322, 1348–1352, doi: 10.1126/science.1166585

Martinez, C. F., Holanda, N., Pereira, C. B., & Drake, N. A. 2020, , 494, 1470, doi: 10.1093/mnras/staa647

Martinez, P., Kasper, M., Costille, A., et al. 2013, Astronomy Astrophysics, 554, A41, doi: 10.1051/0004-6361/201220820

Mateo, M., III, J. I. B., Crane, J., et al. 2012, in Ground-based and Airborne Instrumentation for Astronomy IV, ed. I. S. McLean, S. K. Ramsay, & H. Takami, Vol. 8446, International Society for Optics and Photonics (SPIE), 1686 – 1704, doi: 10.1117/12.926448

Mathieu, R. D., Meibom, S., & Dolan, C. J. 2004, The Astrophysical Journal, 602, L121–L123, doi: 10.1086/382686

Matthews, C. T., Crepp, J. R., Vasisht, G., & Cady, E. 2017, Journal of Astronomical Telescopes, 3, 045001

Mawet, D., Shelton, C., Wallace, J., et al. 2014a, SPIE, 9143, 9143

Mawet, D., Milli, J., Wahhaj, Z., et al. 2014b, ApJ, 792, 97

Mawet, D., Wizinowich, P., Dekany, R., et al. 2016, SPIE, 9909, 9909

Mazeh, T. 2008, in EAS Publications Series, Vol. 29, EAS Publications Series, ed. M. J. Goupil & J. P. Zahn, 1–65, doi: 10.1051/eas:0829001

Mazin, B., Day, P., Zmuidzinas, J., & LeDuc, H. 2002in , American Institute of Physics, 309–312

Mazin, B. A., Bumble, B., Meeker, S. R., et al. 2012, Opt. Express, 20, 1503

Mazin, B. A., Meeker, S. R., Strader, M. J., et al. 2013a, PASP, 125, 1348

—. 2013b, Publications of the Astronomical Society of the Pacific, 125, 1348

McHugh, S., Mazin, B. A., Serfass, B., et al. 2012, Review of Scientific Instruments, 83, 044702, doi: 10.1063/1.3700812

Meeker, S. R., Mazin, B. A., Walter, A. B., et al. 2018, , 130, 065001, doi: 10.1088/1538-3873/aab5e7

Meibom, S., & Mathieu, R. D. 2005, , 620, 970, doi: 10.1086/427082

Meynet, G., Mermilliod, J. C., & Maeder, A. 1993, , 98, 477

Nine, A. C., Milliman, K. E., Mathieu, R. D., et al. 2020, , 160, 169, doi: 10.3847/1538-3881/abad3b

Pinsonneault, M. H., & Stanek, K. Z. 2006, The Astrophysical Journal, 639, L67, doi: 10.1086/502799

Poovelil, V. J., Zasowski, G., Hasselquist, S., et al. 2020, arXiv e-prints, arXiv:2009.06777. https://arxiv.org/abs/2009.06777

Portegies Zwart, S. F., McMillan, S. L. W., & Gieles, M. 2010, , 48, 431, doi: 10.1146/annurev-astro-081309-130834

Prisinzano, L., Micela, G., Sciortino, S., & Favata, F. 2003, , 404, 927, doi: 10.1051/0004-6361:20030524

Racine, R., Walker, G. A. H., Nadeau, D., Doyon, R., & Marois, C. 1999, PASP, 111, 587

Raghavan, D., McAlister, H. A., Henry, T. J., et al. 2010, , 190, 1, doi: 10.1088/0067-0049/190/1/1

Ricker, G. R., Winn, J. N., Vanderspek, R., et al. 2015, Journal of Astronomical Telescopes, Instruments, and Systems, 1, 014003, doi: 10.1117/1.JATIS.1.1.014003

Ruane, G., Ngo, H., Mawet, D., et al. 2019, The Astronomical Journal, 157, 118, doi: 10.3847/1538-3881/aafee2

Sales Silva, J. V., Peña Suárez, V. J., Katime Santrich, O. J., et al. 2014, , 148, 83, doi: 10.1088/0004-6256/148/5/83

Simon, M., & Obbie, R. C. 2009, The Astronomical Journal, 137, 3442–3448, doi: 10.1088/0004-6256/137/2/3442

Smith, J. P., Mazin, B. A., Walter, A. B., et al. 2020, IEEE Transactions on Applied Superconductivity, 31, 1

Soummer, R., Ferrari, A., Aime, C., & Jolissaint, L. 2007, ApJ, 669, 642

Soummer, R., Hagan, J. B., Pueyo, L., et al. 2011, , 741, 55, doi: 10.1088/0004-637X/741/1/55

Soummer, R., Pueyo, L., & Larkin, J. 2012, ApJ, 755, L28

Sparks, W. B., & Ford, H. C. 2002, ApJ, 578, 543

Strader, M. J., Archibald, A. M., Meeker, S. R., et al. 2016, Mon. Not. R. Astron. Soc., 459, 427

Sung, H., Bessell, M. S., Lee, B.-W., & Lee, S.-G. 2002, The Astronomical Journal, 123, 290, doi: 10.1086/324729

Szypryt, P., Duggan, G. E., Mazin, B. A., et al. 2014, Mon. Not. R. Astron. Soc., 439, 2765

Szypryt, P., Meeker, S. R., Coiffard, G., et al. 2017, Opt. Express, 25, 25894

Torres, G., Andersen, J., & Giménez, A. 2010, , 18, 67, doi: 10.1007/s00159-009-0025-1

van der Walt, S., Schönberger, J. L., Nunez-Iglesias, J., et al. 2014, PeerJ, 2, e453, doi: 10.7717/peerj.453

van Dokkum, P. 2001, Publications of the Astronomical Society of the Pacific, 113, 1420–1427, doi: 10.1086/323894

van Eyken, J. C., Strader, M. J., Walter, A. B., et al. 2015, ApJS, 219, 14

Vesperini, E., McMillan, S. L. W., D'Antona, F., & D'Ercole, A. 2013, , 429, 1913, doi: 10.1093/mnras/sts434

Vesperini, E., McMillan, S. L. W., D'Antona, F., & D'Ercole, A. 2011, Monthly Notices of the Royal Astronomical Society, no–no, doi: 10.1111/j.1365-2966.2011.19046.x

Vousden, W. D., Farr, W. M., & Mandel, I. 2016, , 455, 1919, doi: 10.1093/mnras/stv2422

Walter, A. B., Bockstiegel, C., Brandt, T. D., & Mazin, B. A. 2019, Publications of the Astronomy Society of the Pacific, 131, 114506

Walter, A. B., Mazin, B. A., Bockstiegel, C., et al. 2018, in SPIE, Vol. 10702, Ground-based and Airborne Instrumentation for Astronomy VII, 107020V

Walter, A. B., Fruitwala, N., Steiger, S., et al. 2020, Publications of the Astronomical Society of the Pacific, 132, 125005, doi: 10.1088/1538-3873/abc60f

Wright, J. T., & Howard, A. W. 2009, , 182, 205, doi: 10.1088/0067-0049/182/1/205

Zobrist, N., Eom, B. H., Day, P., et al. 2019, Applied Physics Letters, 115, 042601